NUREG/CR-6934
PNNL-16192

# Fatigue Crack Flaw Tolerance in Nuclear Power Plant Piping

# A Basis for Improvements to ASME Code Section XI Appendix L

**Pacific Northwest National Laboratory**

**U.S. Nuclear Regulatory Commission**
**Office of Nuclear Regulatory Research**
**Washington, DC 20555-0001**

NUREG/CR-6934
PNNL-16192

# Fatigue Crack Flaw Tolerance in Nuclear Power Plant Piping

# A Basis for Improvements to ASME Code Section XI Appendix L

Manuscript Completed: November 2006
Date Published: May 2007

Prepared by
S.R. Gosselin, F.A. Simonen, P.G. Heasler,
S.R. Doctor

Pacific Northwest National Laboratory
Richland, WA 99352

D.A. Jackson and W.E. Norris, NRC Project Managers

**Prepared for**
**Division of Fuel, Engineering and Radiological Research**
**Office of Nuclear Regulatory Research**
**U.S. Nuclear Regulatory Commission**
**Washington, DC 20555-0001**
**NRC Job Code Y6604**

# Abstract

Appendix L of the ASME Section XI Boiler and Pressure Vessel Code as adopted in 1996 provides non-mandatory guidelines for the nuclear power industry to evaluate the serviceability of components that are adversely subjected to fatigue stresses. Appendix L uses a damage tolerance approach to establish an examination strategy to ensure that components operate reliably between successive inspections. Experience has identified the need for two main improvements: 1) updating requirements for postulated flaw depths by incorporating insights gained from industry and U.S. Nuclear Regulatory Commission (NRC) performance demonstration data and 2) accounting for the initiation and coalescence of multiple fatigue cracks observed in the field. The work described in this report provides a technical basis for improvements to the requirements of Appendix L.

Using industry Performance Demonstration Initiative (PDI) fatigue crack detection data, Pacific Northwest National Laboratory (PNNL) developed a matrix of statistically based probability of detection (POD) curves that considered various nondestructive evaluation performance factors. The improved POD curves, developed for ferritic and for wrought stainless steel materials, are presented in this report. These results showed that very good nondestructive evaluation (NDE) performance could be expected when Appendix L postulated flaw depths are based on the existing Section XI flaw acceptance standards. Probabilistic fracture mechanics calculations comparing best-estimate leak probabilities obtained from both the new performance-based POD curves and previous probabilistic fracture mechanics models are presented.

A review of service experience showed that a crack growth model was needed to address failures for which several fatigue cracks can initiate at multiple sites and then link together to form a single fatigue crack that is much longer than the standard 6:1 aspect ratio flaws used by ASME Section XI for damage tolerance calculations. Fracture mechanics calculations established aspect ratios for equivalent single cracks (ESC) between the extremes of a 6:1 ratio and a full circumferential crack that can be used in ASME Section XI Appendix L flaw tolerance assessments. The computations presented in this report consider two materials (stainless steel and low-alloy steel), five nominal pipe (sizes 50.8 mm(2 in.) Schedule 80 and 160, 154.6 mm (6 in.) Schedule 160, 254 mm (10 in.) Schedule 160, and 558.8 mm (22 in.) Schedule 160), five cyclic membrane-to-gradient stress ratios (0.0, 0.10, 0.25, 1.0, and 3.0), and a wide range of primary loads. Calculations identify the ESC aspect ratio associated with the hypothetical reference flaw depth assumptions in Appendix L. Examples of computations that apply the proposed ESC model of the revised Appendix L also are presented.

# Foreword

American Society of Mechanical Engineers (ASME) first incorporated Appendix L, "Operating Plant Fatigue Assessment," in the 1996 Addenda of Section XI, Boiler and Pressure Vessel Code. ASME developed Appendix L to provide guidance for evaluating plant operating events and determining the acceptability of components for which fatigue usage limits may have been exceeded or for which fatigue stresses may be a concern. Experience in applying Appendix L revealed three issues needing resolution: (1) the crack growth model needed to account for the initiation and coalescence of multiple fatigue cracks observed in the field, (2) flaw detection and sizing performance needed to reflect newly available performance demonstration data, and (3) application of Appendix L was found to be impractical for plant license renewal. The first two items were issues identified by U.S. Nuclear Regulatory Commission (NRC) staff. These items were discussed in a *Federal Register* Notice dated September 22, 1999 (64 FR 51386). ASME established the Section XI Task Group of Operating Plant Fatigue Assessments (TGOPFA) to consider the issues.

The U.S. Nuclear Regulatory Commission participated on TGOPFA, and the Office of Nuclear Regulatory Research conducted research to support resolution of the issues and provide an independent technical assessment. ASME has revised Appendix L, based substantially on the findings provided in this report, and ASME has approved the revised appendix for use.

The first issue was that an improved crack growth model was needed as the allowable operating periods calculated for the postulated flaws could be nonconservative. Reviewers of nuclear power plant service history and performance demonstration data had observed that flaw aspect ratios (flaw length-to-depth ratios) were significantly larger than the 6:1 default aspect ratio assumed in Appendix L. Thermal fatigue mechanisms can cause several small fatigue cracks to initiate, coalesce, and then grow like an equivalent long, single crack. Calculating allowable operating periods using the default aspect ratio can be nonconservative. An improved crack growth model was needed to more accurately calculate allowable operating periods. This report provides a detailed discussion of flaw aspect ratios and examines the equivalent single crack aspect ratio necessary in an Appendix L flaw tolerance evaluation to account for the effect of relatively long flaws with large aspect ratios.

The second issue was a need for improved probability of detection (POD) curves. The original postulated flaw depths were based primarily on judgment and limited quantitative information of ultrasonic inspection capabilities. New data on flaw detection capabilities became available from the Performance Demonstration Initiative (PDI) that showed for ferritic and wrought stainless steels, an inspector's ability to detect smaller fatigue cracks (depths of 10% to 25% of the wall thickness) was much better than originally assumed in Appendix L. This was due to improvements in nondestructive examination (NDE) technology. The result of the improvements is that very good NDE performance can be expected at flaw depths consistent with the allowable flaw depths specified in Section XI of the ASME Boiler and Pressure Vessel Code. The better than assumed POD means that significant reductions in leak probabilities can be expected with improved inspection, and the postulated reference flaw depths can be reduced. A matrix of statistically based POD curves has been developed that considered

various NDE performance factors. This report presents the improved POD curves, developed for ferritic and for wrought stainless steel materials.

The third issue was a need to improve the practicality of applying Appendix L for plant license renewal. The industry application of Appendix L for plant license renewal revealed that the methodology was impractical. For many fatigue sensitive locations, Appendix L was unnecessarily conservative regarding flaw size assumptions. In addition, the Appendix L flaw tolerance procedures did not in many cases provide an inspection interval of sufficient length to allow long-term plant operation. As such, the only viable options were to recalculate the ASME Code cumulative usage factor (CUF) using more refined inputs or repair/replace the affected components. The PDI information allows for significantly smaller sizes for postulated flaws. With this information, it has been possible to (1) develop improved performance models to quantify the capabilities of ultrasonic examinations (i.e., POD curves), (2) upgrade the POD modeling capabilities in probabilistic fracture mechanics (PFM) computer codes, and (3) gain a better understanding of how NDE performance factors affect piping reliability and associated augmented inspection strategies. This report applies this information to evaluate the Appendix L flaw tolerance procedure and its ability to define augmented inspection strategies that can offset increases in the failure frequencies expected to occur as components continue to operate after the CUF limit is exceeded.

Brian W. Sheron, Director
Office of Nuclear Regulatory Research
U.S. Nuclear Regulatory Commission

# Contents

# Appendix

# Figures

# Tables

# Executive Summary

Since the 1996 introduction of Appendix L into the ASME Code Section XI, the nuclear industry and the U.S. Nuclear Regulatory Commission (NRC) have raised concerns regarding the flaw tolerance procedure in this appendix. As a result, the ASME Working Group on Operating Plant Criteria re-established the Task Group on Operating Plant Fatigue Assessments to address the various concerns. In these investigations, the task group established an improved technical basis for both the flaw models and the corresponding successive inspection frequencies in Appendix L.

This report describes work performed to establish a technical basis for improvements to the requirements of Appendix L. Section 2 reviews the background and basis for the current procedure and identifies the need for improvements to Appendix L. Recent industry applications for plant license renewal showed that, for many fatigue sensitive locations, the conservative nature of the flaw size assumptions and successive inspection frequency requirements essentially rendered the flaw tolerance approach ineffectual and impractical. This was especially true for components with section thicknesses less than 25.4 mm (1 in.). In addition, the NRC raised specific concerns with the technical basis for the default 6:1 aspect ratio for the initial postulated flaw assumed in the procedures. The aspect ratio concerns were raised in light of crack area profiles observed in several service-induced thermal fatigue failures.

The service experience study documented in Section 3 shows that service-induced fatigue problems at operating plants are caused primarily by thermal stratification or hot/cold water mixing. These loadings are known to consist of many cycles with the cyclic boundary conditions changing rapidly, causing cracks to initiate and grow at multiple locations on the inside surface of the pipe. Because of the large nonlinear gradient stress profiles associated with these service conditions, cracks will tend to grow in the length direction where the highest surface stresses occur. This can cause many of the cracks to coalesce and subsequently grow as larger defects.

The data presented in Section 3 show that the observed aspect ratios (flaw lengths-to-depth ratios) were significantly larger than the 6:1 default aspect ratio assumed in Appendix L. For the range of crack depths specified in the current Appendix L (i.e., normalized crack depths [a/t] between 10% and 30%), the measured aspect ratios were as low as 10:1 and as high as 330:1. This suggests that the 6:1 default initial aspect ratio may not be appropriate and adjustments are needed for the postulated reference flaw model or for the successive inspection frequencies.

Section 4 describes improved probability of detection (POD) curves developed for ferritic and wrought stainless steels. For both materials, the ability to detect smaller fatigue cracks (depths of 10% to 25% of the wall thickness) was much better than originally assumed in Appendix L, such that very good nondestructive evaluation (NDE) performance could be expected at flaw depths consistent with allowable flaw depths specified in ASME Section XI Tables IWB-3514-1 and 3514-2. Excellent NDE performance for fatigue cracks always can be expected for ferritic materials. Because very little difference was observed between POD curves for all the ferritic cases considered in this study, the NDE performance was represented by a single POD curve. Very good performance can be expected also for circumferential cracks in stainless steel but only when the crack is located on the same side of the weld from which the NDE examination is made. For stainless steels, the POD depended on component thickness. In all cases, inspector qualification had only a small effect on the resulting POD curves.

For stainless steels, when the access is limited to the far side, the data available from the industry sponsored Performance Demonstration Initiative (PDI) produced an optimistic view of inspector performance. Because of the difficulties in inspecting stainless steel welds, the PDI test specimens were screened to ensure that the far-side flaw specimens were detectable using the best currently available technology such that the corresponding PDI performance represents a best effort for far-side flaws. Additional research will be needed to better quantify performance estimates for far-side flaws. However, these conditional performance results, coupled with expert judgment, provide valuable insights that can be used to establish qualitative guidance for flaw tolerance evaluations.

Section 5 describes calculations performed by Pacific Northwest National Laboratory to examine how component reliability (i.e., leakage frequency) is affected when the improved POD curves in Section 4 are assumed for different inspection strategies. When a "PDI performance" POD curve is assumed, all inspection strategies show a significant reduction in component failure frequency for the operating period after the first inspection. This is due primarily to the ability to detect and repair small cracks early in plant life. The calculated component leak frequencies continued to decrease with each subsequent inspection and remained below the threshold leak frequency associated with a calculated usage factor of 1.0.

Based on the PDI data, the very good NDE performance can be expected for flaw depths consistent with allowable flaw depths specified in ASME Section XI Tables IWB-3514-1 and 3514-2. Because significant reductions in leak probabilities can be expected from the initial and subsequent inspections, the postulated reference flaw depths of the current Appendix L can be reduced. These results also suggest that the current factor of two reductions in the allowable operating period can be eliminated.

A deterministic crack growth analysis as described in Section 6 was conducted to aid in understanding the effects of various loading types on the growth of fatigue cracks, considering flaw growth in both the depth and surface length directions. The results showed that crack growth is strongly dependent on the aspect ratio of the surface crack and on the relative magnitudes of cyclic membrane stresses and cyclic gradient stresses (i.e., linear and/or nonlinear). As expected, under thermal transient conditions typically associated with component failures observed in the field, the high-cycle loadings attributed to thermal striping, turbulence penetration, and thermal mixing can lead to mainly surface cracking with shallow flaw depths.

Because the initial aspect ratio was known to be a critical input to the fatigue crack growth calculations, the work described in Section 7 gives detailed consideration to flaw aspect ratios. In addition, the crack profiles observed in the field failures as described in Section 3 show that fatigue cracking often results in relatively long flaws with large aspect ratios. Because the nature of the thermal fatigue mechanisms associated with these failures causes several small fatigue cracks to initiate, coalesce, and then grow like an equivalent long single crack, the calculations in Section 7 examined the equivalent single crack aspect ratio necessary to account for this effect in an Appendix L flaw tolerance evaluation.

The aspect ratio investigations described in Section 7 suggest that a single 6:1 aspect ratio will adequately account for the effects of multiple crack initiation and crack growth for uniform membrane cyclic stresses. In such cases, the alternating membrane stress is large compared to the alternating gradient stress ($\Delta\sigma_M/\Delta\sigma_G$ is very large). On the other hand, the appropriate aspect ratio of the equivalent single crack becomes very large as $\Delta\sigma_M/\Delta\sigma_G$ becomes very small. Under these loading conditions, the allowable

operating periods calculated for a 6:1 postulated flaw are nonconservative compared to the shorter times required to reach critical crack depths for realistic conditions of multiple crack initiation and linking. Therefore, it can be inappropriate to base Appendix L successive examination frequencies on crack growth results for a single 6:1 aspect ratio flaw.

As an alternative to the current Appendix L procedures, the analyst may elect to conservatively assume an aspect ratio for a crack length equal to the full inside circumference of the component. However, the evaluations described in Section 7 show this assumption can be unnecessarily conservative for typical membrane-to-gradient stress ratios expected to be present in operating plant fatigue sensitive locations. A better alternative is to determine allowable inspection intervals based on the equivalent single crack (ESC) models in Section 7 and the maximum end-of-inspection-period-allowable flaw depths calculated from the analytical procedures of Section XI Appendix C.

# Acknowledgments

The development of the methodology for fatigue crack growth calculations and failure probability calculations used in this project was sponsored by the U.S. Nuclear Regulatory Commission. D. A. Jackson and W. E. Norris are the NRC project managers. F. L. Becker, Electric Power Research Institute, assisted Pacific Northwest National Laboratory in the performance of statistical evaluations of flaw detection data from the Performance Demonstration Initiative. A. F. Deardorff, Structural Integrity Associates, Inc. contributed the review of the nuclear industry fatigue cracking experience and the effects of aspect ratio on crack growth. Valuable guidance and technical contributions were provided by R. G. Carter, Electric Power Research Institute. Pacific Northwest National Laboratory is operated by Battelle for the U.S. Department of Energy under Contract DE-AC05-76RL01830.

# Abbreviations and Acronyms

| | |
|---|---|
| ANL | Argonne National Laboratory |
| ASME | American Society of Mechanical Engineers |
| BGE | Baltimore Gas & Electric Company |
| BWR | boiling water reactor |
| CUF | cumulative usage factor |
| CVCS | chemical and volume control system |
| EPRI | Electric Power Research Institute |
| erfc | error function |
| ESC | equivalent single crack |
| ISI | inservice inspection |
| LEFM | linear elastic fracture mechanics |
| LWR | light water reactor |
| MSC | microstructurally small crack |
| NDE | nondestructive evaluation |
| NRC | U.S. Nuclear Regulatory Commission |
| PDA | Performance Demonstration Administrator |
| PDI | Performance Demonstration Initiative |
| PFM | probabilistic fracture mechanics |
| PNNL | Pacific Northwest National Laboratory |
| POD | probability of detection |
| PWR | pressurized water reactor |
| PZR | pressurizer |
| QA | quality assurance |
| RCS | reactor coolant system |
| UKAEA | United Kingdom Atomic Energy Authority |
| UT | ultrasonic inspection |

# 1 Introduction

Section XI of the American Society of Mechanical Engineers (ASME) Boiler and Pressure Vessel Code has worked since the early 1990s to develop guidelines for the nuclear power industry to evaluate the serviceability of components that are subject to cyclic fatigue stresses. Results of this work formed the basis for a non-mandatory Appendix L that became part of the 1996 Addenda to the 1995 Edition of Section XI (ASME 2004a). A key part of this appendix was a damage tolerance analysis, which postulated a flaw at the fatigue location of interest and then performed a fatigue crack growth analysis to determine inspection intervals that can detect fatigue cracks before they exceed Code-allowable sizes.

Experience with the initial version of Appendix L identified two main areas that needed improvements. New data on the flaw detection capabilities had become available, and these data showed that ultrasonic inspections can detect flaws much smaller than assumed during the original development of Appendix L. This information allows for significantly smaller sizes for postulated flaws. A second area of needed improvement was related to the growth of fatigue cracks. A crack growth model was needed to address component fatigue failures for which several fatigue cracks can initiate at multiple sites and then link together to form a single fatigue crack that is much longer than the standard 6:1 aspect ratio of the flaws typically used by ASME Section XI for damage tolerance calculations.

The work described in this report provides a technical basis for improvements to the requirements of Appendix L. Pacific Northwest National Laboratory (PNNL) was jointly sponsored by the Office of Nuclear Regulatory Research of the U.S. Nuclear Regulatory Commission (NRC), the Electric Power Research Institute (EPRI), and the Office of Nuclear Energy Science and Technology of the U.S. Department of Energy in support of the Nuclear Energy Plant Optimization program. The overall objectives for the coordinated research were to

1. develop improved performance models to quantify the capabilities of ultrasonic examinations (i.e., probability of detection [POD] curves)

2. upgrade the POD modeling capabilities in probabilistic fracture mechanics (PFM) computer codes

3. understand how nondestructive evaluation (NDE) performance factors affect piping reliability and associated augmented inspection strategies

4. evaluate the current Appendix L flaw tolerance procedure and its ability to define augmented inspection strategies that can offset increases in the failure frequencies expected to occur as components continue to operate after calculated usage factors exceed 1

5. develop flaw tolerance evaluation equivalent single crack reference flaw models and operating period correction factors that can be used to define successive inspection schedules that will account for the initiation and growth of fatigue cracks at multiple locations on the component surface.

This report presents an evaluation of industry NDE fatigue crack detection data compiled through the Performance Demonstration Initiative and documents the development of families of performance-based POD curves based on current industry data for the detection of fatigue cracks. A set of statistically based

POD curves was developed considering various combinations of NDE performance factors such as material type (stainless steel or carbon steel), access (double-sided or single-sided), section thickness, procedure (automatic or manual), and inspector qualification. PNNL worked directly with EPRI personnel at the NDE Center in Charlotte, North Carolina. During this project PNNL provided the statistical tools and training so that future analyses of the PDI data could be performed by the NDE Center staff. This report also presents results of probabilistic and deterministic calculations of fatigue crack growth. These calculations evaluated the effects of multiple fatigue cracks and provide a technical basis for the lengths (aspect ratios) of postulated fatigue cracks used for the damage tolerance analyses of Appendix L. Specific sections of this report cover the following topics:

- background on Appendix L of ASME Section XI, industry experience with Appendix L, and a discussion of suggested improvements (Section 2)

- a review of experience with fatigue cracking in the nuclear power industry (Section 3)

- a discussion of recent improvements in crack detection capabilities and the development of statistically based probability of detection curves (Section 4)

- probabilistic fracture mechanics calculations that quantify the potential reductions in component failure rates that can be expected if periodic inspections are performed at suitable frequencies with the enhanced flaw detection capabilities (Section 5)

- an evaluation of the effects of crack growth on the aspect ratios of fatigue cracks (Section 6)

- the development of a methodology to address multiple fatigue cracks and the effects of such cracks on the calculation of allowable operating periods between inservice inspections (Section 7).

A recent EPRI study (EPRI 2002; Deardorff et al. 2002) has proposed revisions to the fatigue crack initiation model originally used in NUREG/CR-6674 (Khaleel et al. 2000). The revisions made minor changes to the constants of the strain life relations based on Argonne National Laboratory (ANL) work described in NUREG/CR-6717, and assumed a reduced standard deviation in fatigue strength at the endurance limit ($>1 \times 10^6$ cycles). Because the ANL database has very little experimental data at the endurance limit, a standard deviation at the endurance limit equal to 10% of the mean endurance limit strain was assumed following a default coefficient of variation recommendation by Wirsching (1995). The limited amount of data in the ANL database at strains near the endurance limit made it difficult to validate this assumption for the coefficient of variation. The changes to the standard deviation at the endurance strain did not significantly affect the high-strain region of the fatigue curves currently used in pc-PRAISE. Sensitivity studies (EPRI 2002; Deardorff et al. 2002) showed that the reductions in predicted leak frequencies associated with the proposed changes to the fatigue curves were relatively small when fatigue usage was dominated by high-strain cyclic conditions.

Because the above recommendations of the EPRI study (EPRI 2002; Deardorff et al. 2002) were not used in the current study, the impacts of the proposed changes on the results and conclusions in Sections 5 and 7 of this report were assessed. The fatigue usage for the components evaluated in Section 5 is

dominated by high-strain (low-cycle) loads, so proposed changes to the fatigue curves are not expected to significantly change either the calculations of component reliabilities or the effects of the PDI performance-based POD curves in Sections 5. Section 7 also focuses on high-strain load. Again, the effects on predicted fatigue lives are expected to be small, particularly for the results that are based on relative values of failure probabilities.

# 2 Appendix L Background

Section XI of the ASME Boiler and Pressure Vessel Code contains the requirements for inservice inspection of operating nuclear power plants. Rules for the evaluation of flaw indications detected during inspection are included. In the case of planar flaws, Section XI contains rules for flaw characterization and evaluation. IWB-3500 contains a set of acceptance standards for smaller flaw indications not requiring further evaluation. IWB-3600 contains rules for analytical evaluation of larger flaws. Section XI requires that the evaluation consider both crack growth and allowable flaw size for Normal/Upset and Emergency/Faulted Conditions. Non-mandatory Appendices A, C, and H contain a methodology for evaluating flaws in ferritic vessels, stainless steel piping, and ferritic piping, respectively.[(a)]

In November 1991, the ASME Section XI Task Group on Operating Plant Fatigue Assessment was formed to study fatigue evaluation methods, develop procedural guidelines, and establish acceptance criteria that operating plants can use to assess component serviceability. This initial work proposed methodologies for evaluating thermal fatigue concerns that result from plant cyclic operation, for example, when a component's cumulative usage factor (CUF) was predicted to be greater than 1.0. The results of this initial work were published as a non-mandatory Appendix L in the 1996 Addenda to the 1995 Edition of Section XI (ASME 2004a). Code-enabling words were included in IWB-3700. Two procedures were included:

- Fatigue Analysis

  This approach allowed re-analysis of the component Code design cumulative usage factor (CUF) originally documented in the plant design stress reports. Consideration could be given to use of later codes, updated or more sophisticated stress analysis, revised load definition, actual cyclic loadings.

- Flaw Tolerance Analysis

  This approach assumed a hypothetical flaw for the location of interest. The methods of Section XI for actual flaws were to be applied to predict crack growth, determine an allowable flaw size, and to determine an inspection interval.

The operating plant fatigue assessment process in Figure 2.1 shows how these two fatigue analyses might be used to evaluate a fatigue concern identified at a piping component in an ASME Class 1 system. In this example the analyst may first re-analyze this component using the Code fatigue analysis procedure for ASME Class 1 piping (ASME 2004b). Should this analysis fail to show that the predicted cumulative

(a) In the July 1, 2002, Addenda to ASME Section XI, Appendices C and H were revised and consolidated into a new Appendix C that treats both austenitic and ferritic piping. A new Appendix H considers flaw evaluations of austenitic and ferritic piping using the failure assessment diagram approach.

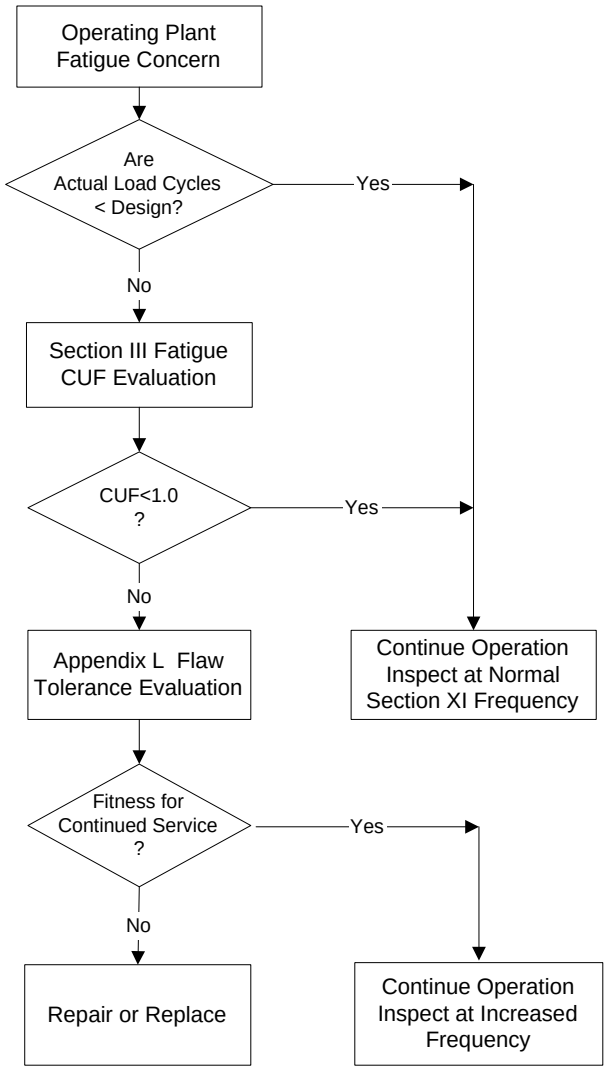


**Figure 2.1 Example Operating Plant Fatigue Assessment of a Component Fatigue Concern Identified in an ASME Class 1 Piping System**

usage factor is less then 1.0, the component's fitness for service may then be based on a flaw tolerance evaluation and the implementation of an inspection strategy designed to detect a defect before it grows to an unacceptable size.

## 2.1 Flaw Tolerance Analysis

The Appendix L damage tolerance procedure is used to identify an inspection strategy designed to ensure that successive ultrasonic examinations of the component occur at a frequency that will identify a fatigue crack before it grows to an unacceptable size. In this procedure, the component is first inspected to verify the absence of any relevant and detectable indications or flaws. Subsequent inspections are then based on deterministic fracture mechanics calculations and on the time required for the assumed flaws to

grow to unacceptable size. The flaw tolerance approach is well suited for operating plants because fatigue concerns are typically limited to only a few plant component locations. In addition, with this approach, future performance capabilities can be established independent of past loading histories. The procedure for performing fatigue flaw tolerance evaluations is contained in Article L-3000 of Appendix L.

The procedural steps of Appendix L include the following:

1. Verify the absence of any relevant indication exceeding the applicable flaw acceptance standards in Table IWB-3410.

2. Postulate the existence of a hypothetical flaw according to the flaw model in L-3200.

3. Determine the stresses at the location of the postulated flaw.

4. Determine the postulated end-of-evaluation period flaw size and critical flaw sizes by using existing ASME Section XI analytical procedures contained in Appendix A, Appendix C, or Appendix H, as applicable.

5. Apply the appropriate flaw acceptance criteria contained in IWB-3600.

6. Continue operation and inspect the component at a frequency specified in L-3420.

### 2.1.1 Appendix L Postulated Flaws

The bases for the Appendix L postulated flaws are discussed in EPRI TR-104691, *Operating Nuclear Power Plant Fatigue Assessments* (EPRI 1995). Because the absence of flaws is based on inspection results, the flaw model (size and shape) must be consistent with the inspection capabilities. In other words, the hypothetical reference flaw assumed in the flaw tolerance assessment should represent the largest flaw expected to be missed during the initial inspection. The postulated flaw sizes used in Appendix L are described in Table 2.1 (ASME 2004a).

The postulated flaw sizes were based primarily on judgment and limited quantitative information of ultrasonic inspection (UT) capabilities. At that time, the limited performance demonstration data were available only for thick-walled reactor pressure vessels, and these data were considered most applicable when the component section thickness was greater than 101.6 mm (4 in.). Because the industry's Performance Demonstration Initiative (PDI) for piping was just starting, Appendix VIII NDE performance demonstration data were not available. Consequently, conservative estimates were made based on the discouraging flaw detection and sizing performance had been observed in earlier round-robin studies (Spanner et al. 1990). The Appendix L postulated flaws were subsequently reviewed by the ASME Section XI Working Group on Procedure Qualification and Volumetric Examination. In that group's opinion, the inner surface fatigue cracks described in Table 2.1 could be detected in service for most of the materials that comprise the reactor coolant system. However, the working group understood

**Table 2.1 Appendix L Table L-3210-1 Postulated Surface Flaw Depth**

| Section Thickness, t mm (in.) | Postulated Surface Flaw Depth, a/t (%) |
|---|---|
| 12.7 (0.5) | 30.0 |
| 25.4 (1.0) | 20.0 |
| 50.8 (2.0) | 15.0 |
| 76.2 (3.0) | 11.7 |
| 101.6 (4.0)-304.8 (12.0) | 10.0 |
| Notes:<br>(1) 6:1 minimum aspect ratio.<br>(2) For t <12.7 mm (<0.5 in.), the postulated flaw depth a = 3.8 mm (0.15 in.)<br>(3) For t >304.8 mm (>12 in.), the postulated flaw depth a = 30.5 mm (1.2 in.) | |

that the capability of detecting cracks in components containing dissimilar (bimetallic or trimetallic welds) and for cast austenitic piping, due to their challenging metallurgical characteristics (EPRI 1995; Gosselin 1995), was uncertain.

### 2.1.2 Appendix L Successive Inspections

Flaw tolerance in Appendix L is measured in terms of an allowable operating period, P. As defined in Appendix L, the parameter P represents the time required for the a hypothetical (postulated) flaw from Table 2.1 to grow to a depth equal to the maximum allowable flaw size specified in ASME Section XI IWB-3600.

Successive inspections are then implemented at the location of concern according to the schedule shown in Table 2.2 (ASME 2004a). The time intervals between inservice inspections (ISIs) are selected to ensure that the component will be re-examined before a growing hypothetical flaw exceeds half the size allowed by ASME Section XI.

**Table 2.2 Appendix L Successive Inspection Schedule**

| Allowable Operating Period, P | Successive Inspection Frequency |
|---|---|
| ≥20 years | End of each 10 year Inspection Interval |
| <20 years | End of P/2 operating years or each operating cycle, whichever is greater |

## 2.2 Industry Experience with Appendix L

Faced with an operating fatigue concern, nuclear plants primarily rely on ASME Section III Class 1 design rules in order to establish a basis for component operability. These rules constitute the requirements for nuclear power plant vessel and component construction. When combined with the Owner's Design Specification, they are intended to provide reasonable assurance that the plant piping and components will operate reliably throughout their design life. In fact, industry service experience has shown that, when all significant fatigue loads are recognized and accounted for in the analysis, the piping components provide excellent reliability (EPRI 1995).

In the majority of cases, operating plant fatigue concerns (including incidents of fatigue cracking) are associated with the discovery of loading conditions not accounted for in the plant's design stress reports. Faced with this problem, utilities usually will attempt to establish component operability by "requalifying" the component design. For those plants designed to ASME Section III, the analyst simply adds the new loading condition(s) to the other design transients assumed in the Design Report and demonstrates that the revised design basis cumulative usage factor (CUF) remains below 1.0. (Note: For the many operating plants designed to earlier piping design codes [e.g., ANSI B31.7, ANSI B31.1] without original Class 1 fatigue analyses, this approach to component fatigue qualification becomes significantly more difficult and expensive.) Depending on the significance of the loading condition in question, requalifying the as-built component to the original design and licensing requirements may be extremely difficult and in some cases may not be possible. Examples of this can be seen in the industry's efforts to address operating plant fatigue concerns in boiling water reactor (BWR) and pressurized water reactor (PWR) feedwater nozzles, PWR surge lines, PWR spray lines, and other components. In these cases, it may be necessary to deviate from the traditional "design qualification" analysis to confirm component serviceability.

Most recent applications of Appendix L have been associated with license renewal applications. The license renewal rule requires that the licensee perpetuate the current design basis to the end of the renewal period (i.e., 60 years). With regard to fatigue, this means that the calculated CUF using ASME methods must be maintained less than 1.0.

Emphasis is placed on the more fatigue-sensitive areas in the plant that are selected based on anticipated loading conditions as well as industry service experience (Gosselin et al. 1994). These fatigue-sensitive locations are not limited to Class 1 components but may also include Class 2 piping components whose original design qualification was not based on a CUF analysis.

In a 1999 report to the ASME Section XI Task Group on Operating Plant Fatigue Assessments, Baltimore Gas & Electric Company (BGE) indicated that, in license renewal space, the potential for large-scale replacements is real (J. T. Connor, BGE, unpublished). Lines such as the surge line, main and auxiliary spray lines, and chemical volume and control piping connected to the reactor coolant system have the potential to exceed a CUF of 1.0 at a multitude of locations prior to the end of the extended design life. In many cases, the Appendix L flaw tolerance procedures do not provide a sufficiently long inspection interval to allow long-term plant operation. As such, the only viable options are to recalculate the CUF using more refined inputs or, at worst, repair/replace the affected components.

In 1999, the NRC documented its comments on Appendix L in the *Federal Register* (64 FR 51370-400)]. Although the NRC review of Appendix L determined that its use was generally acceptable, the staff identified two issues that need to be considered for future revisions of Appendix L. The first is that the assumption of a postulated flaw with a fixed aspect ratio of 6:1 may not be conservative, depending on the extent that the cumulative usage factor (CUF) criterion has been exceeded along the surface of the component. In the second issue, the staff pointed out that many of the fatigue failures observed in the field result from the growth of multiple fatigue crack initiation locations on the inside circumference of the pipe. Over time, these cracks coalesce and effectively act as a larger defect. This condition can have an impact on crack growth rates, allowable end-of-evaluation flaw depths, and projected remaining fatigue life in a component.

## 2.3 Needed Improvements to Flaw Tolerance Procedures

Recent industry applications of Appendix L have raised concerns regarding the effectiveness of the current flaw tolerance procedures. In general, the consensus opinion is that an improved technical basis is needed for both the postulated flaw sizes and the rules used to establish inspection frequencies. Most noteworthy are the issues of effectiveness, flaw model, and technical basis.

Insights into flaw detection capabilities gained from the industry PDI suggest that in some cases, the NDE capabilities of field teams performing piping inspections are better than assumed in Appendix L. In these cases, the flaw size assumptions in Appendix L may be overly conservative, which render the flaw tolerance alternative ineffectual. In some cases, these conservative flaw size assumptions render the flaw tolerance procedure impractical (e.g., the resulting allowable operating periods are less than one operating cycle). This is especially true for components whose section thickness is less than 1 in.

The flaw size assumptions in the Appendix L flaw tolerance procedure are common to both carbon steel and wrought austenitic stainless steel materials. The assumed flaw depths are presented as a function of section thickness only, and no distinction is made with regard to differences in flaw detection and sizing capability for carbon and stainless steel materials or other NDE performance factors such as inspection access, inspection procedure, or inspector qualification. Finally, questions have been raised regarding the basis for the default 6:1 aspect ratio assumed in the flaw tolerance procedures. These concerns were raised in light of the through-thickness crack profiles observed in several service-induced thermal fatigue failures reported to the NRC.

An improved technical basis is needed for both the flaw models and the rules used to establish inspection frequencies. The flaw model (i.e., size and shape) used in Appendix L should be tied closely to performance demonstration results, and the inspection frequencies should ensure that the likelihood of failure will not increase beyond that provided in the original design code of record.

There is a need for probabilistic fracture mechanics evaluation methods and criteria for acceptable failure probabilities that can be used to evaluate component serviceability, define frequencies for augmented inspections, and establish a reliability basis for the deterministic flaw tolerance procedures in Appendix L. The present report applies probabilistic models to generate numerical results and recommendations that support improved deterministic requirements for Appendix L.`

# 3 Review of Nuclear Industry Thermal Fatigue Cracking Experience

Commercial nuclear power plant thermal fatigue cracking experience was reviewed to determine what insights might be gained with respect to reference flaw model assumptions used in a flaw tolerance analysis. The objective was to document field experience with long fatigue cracks that showed large aspect ratios significantly greater than the 6:1 aspect ratio assumed in the current Appendix L flaw model. These examples clearly showed a need for Appendix L to address postulated cracks with aspect ratios greater than 6:1. The review focused on thermal fatigue cracking and did not address examples of mechanical fatigue such as related to vibrational fatigue.

EPRI recently conducted a review of thermal fatigue experience with reactor coolant system piping (ASME 2004a; EPRI 2002). This study was oriented toward understanding the area of thermal fatigue in normally stagnant non-isolable lines in PWR plants. There has been one similar event in a BWR plant (ASME 2004a; EPRI 2002; Deardorff et al. 2002). In all these events of cracking and/or leakage, the thermal fatigue was related to thermal stratification, valve leakage, and local thermal mixing issues not analyzed in the original plant designs. These failures result from high-cycle effects due to local effects of hot/cold water mixing or thermal fatigue.

The other large body of thermal fatigue cracking events relates to PWR steam generators (PWR Pipe Cracking Study Group 1990) and BWR feedwater nozzles (NRC 1980). In both situations, relatively colder water flows into a nozzle in a hot vessel. For the PWRs, the cracking initiated at the weld between the nozzle/safe-end and the attached piping. In the BWRs, the cracking occurred very locally in the vessel nozzle, and was due to localized mixing of the hot and cold water on the nozzle bore and blend-radius regions. Again, these loadings were unknown at the time of the original plant designs.

Table 3.1 summarizes the relevant thermal fatigue cracking experience. Figure 3.1 shows the crack aspect ratio, expressed as crack depth/total length ($a/l$). In this case, the 6:1 aspect ratio postulated reference flaw specified in ASME Section XI Appendix L would be $a/l = 0.167$. These data show that in a significant number of cases, relatively deep cracking has been discovered with aspect ratios ($a/l$) less than 0.167.

Figure 3.2 provides another view of the data by showing the crack length normalized to the wall thickness ($a/t$). This shows that the crack surface length is normally at least several times the wall thickness. For the range of crack depths specified in the current Appendix L flaw model (i.e., normalized crack depths [$a/t$] between 10% and 30%), the measured aspect ratios were as low as 10:1 and as high as 330:1. In many cases, the inside surface length is very long compared to the wall thickness.

The use of the 6:1 aspect ratio single crack specified in Appendix L may not adequately model predicted crack growth for all operating conditions. The experience suggests that service-induced fatigue problems in operating plants are caused primarily from thermal stratification or hot/cold water mixing conditions. This type of loading is known to contain many cycles with the cyclic boundary conditions changing rapidly, causing cracks to initiate and grow at multiple locations on the inside surface of the pipe.

## Table 3.1 Summary of Thermal Fatigue Cracking Experience

| Plant | Location | Cause | Length, in.[(a)] | Depth, in.[(a)] | a/l | t | a/t |
|---|---|---|---|---|---|---|---|
| Finland | RWCS | Thermal Fatigue - Mixing tee | 7 | NR | NR | NR | NR |
| Sweden | SDC/FW | Thermal Fatigue - Mixing tee | 4 | 0.4 | 0.1 | 1.1 | 0.36 |
| Tihange | SIS | Thermal Stratification | 6 | 0.719 (thru-wall) | 0.12 | 0.719 | 1 |
| Tihange | SIS | Thermal Stratification | 3.9 | 0.24 | 0.06 | 0.719 | 0.33 |
| Tihange | SIS | Thermal Stratification | 3.9 | 0.24 | 0.06 | 0.719 | 0.33 |
| Farley | Feedwater Reducer | Thermal Fatigue | 1-8" | 0.04-0.23 | 0.03 | 0.63 | 0.07-0.37 |
| Turkey Point | Feedwater Reducer | Thermal Fatigue | 32 | 0.1 | 0.003 | 0.63 | 0.16 |
| Sequoyah | SG FW Nozzle | Thermal Stratification | 8.625 | 0.1 | 0.012 | 0.62 | 0.16 |
| Conn Yankee | SG FW Nozzle | Thermal Stratification | 18 | 0.25 | 0.014 | 0.645 | 0.388 |
| Diablo Canyon | SG FW Nozzle | Thermal Stratification | 8 | 0.34 | 0.043 | 0.844 | 0.4 |
| Diablo Canyon | SG FW Nozzle | Thermal Stratification | 2.3 | 0.24 | 0.1 | 0.844 | 0.28 |
| Diablo Canyon | SG FW Nozzle | Thermal Stratification | 2.2 | 0.25 | 0.1 | 0.844 | 0.296 |
| 12 PWRs | SG FW Nozzle | Thermal Stratification | NR | 0.08-0.75 | NR | 0.844 | NR |
| Mihama | Excess Letdown | Thermal Strat/TP Cycling | 1 | 0.344 (thru-wall) | 0.344 | 0.344 | 1 |
| Oconee 1 | RCS Drain | Thermal Strat/TP Cycling | 0.5 | 0.217 (thru-wall) | 0.43 | 0.217 | 1 |
| TMI | RCS Drain | Thermal Strat/TP Cycling | 2 | 0.344 (thru-wall) | 0.172 | 0.344 | 1 |
| Callaway | Excess Letdown | Thermal Fatigue | 4 | 0.344 (thru-wall) | 0.086 | 0.344 | 1 |
| Farley | SIS | Thermal Strat/TP Cycling | 6 | 0.719 (thru-wall) | 0.12 | 0.719 | 1 |
| Genkai | RHR Suction | Thermal Strat/Leakage Cycling | 3.81 | 0.827 (thru-wall) | 0.216 | 0.827 | 1 |
| Loviisa | PZR Aux Spray | Thermal Cycling | 3.2 | valve body | NR | NR | 1 |
| Loviisa | RCS Cross-tie | Thermal Strat/Leakage Cycling | 0.98 | 0.217 (thru-wall) | 0.22 | 0.217 | 1 |
| Loviisa | RCS Cross-tie | Thermal Strat/Leakage Cycling | 1.1 | 0.146 | 0.13 | 0.217 | 0.67 |
| French Test Data | SG FW Nozzle | Thermal Stratification | 1.6 | 0.08 | 0.05 | 0.843 | 0.095 |
| Dampierre 2 | SIS | Thermal Strat/TP Cycling | 4.3 | 0.717 (thru-wall) | 0.167 | 0.717 | 1 |
| Dampierre 1 | SIS | Thermal Strat/TP Cycling | 3.2 | 0.717 (thru-wall) | 0.22 | 0.717 | 1 |
| Dampierre 1 | SIS | Thermal Strat/TP Cycling | 1.57 | 0.354 | 0.225 | 0.717 | 0.493 |
| Obrigheim | CVCS | Thermal Strat/Leakage Cycling | 2.76 | 0.22 (thru-wall) | 0.08 | 0.22 | 1 |
| Biblis | CVCS | Thermal Strat/Leakage Cycling | 2 | 0.248 (thru-wall) | 0.126 | 0.248 | 1 |
| Oconee 2 | MU/HPI | Thermal Strat/TP Cycling | 7.81 | 0.375 (thru-wall) | 0.048 | 0.375 | 1 |
| Crystal River | MU/HPI | Thermal Strat/TP Cycling | 3 | 0.375 (thru-wall) | 0.123 | 0.375 | 1 |
| Civaux | RHR | Thermal Fatigue/Hot-Cold Mixing | 7.087 | 0.366 (thru-wall) | 0.052 | 0.366 | 1 |
| Tsuruga | CVCS Regen HX | Thermal fatigue/Hot-Cold Mixing | 6 | 0.488 (thru-wall) | 0.082 | 0.488 | 1 |
| Nine Mile Point | Iso-Condenser Return | Thermal Strat/Leakage Cycling | 3.5 | 1.25 (thru-wall) | 0.357 | 1.25 | 1 |

Note: Strat = Stratification, TP = Turbulence Penetration, NR = Not Reported.
(a) 25.4 mm = 1 in.

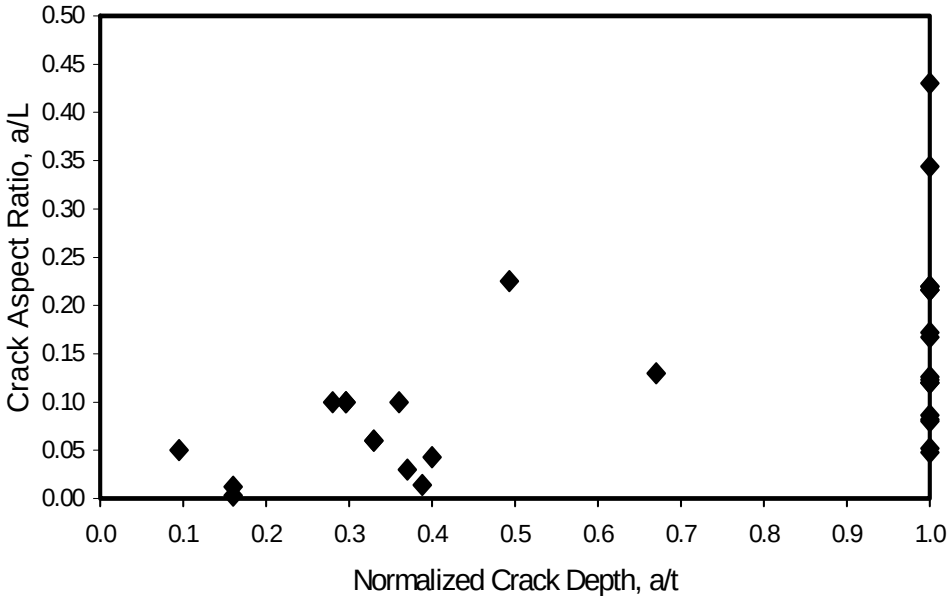


**Figure 3.1 Aspect Ratio from Cracking Experience**

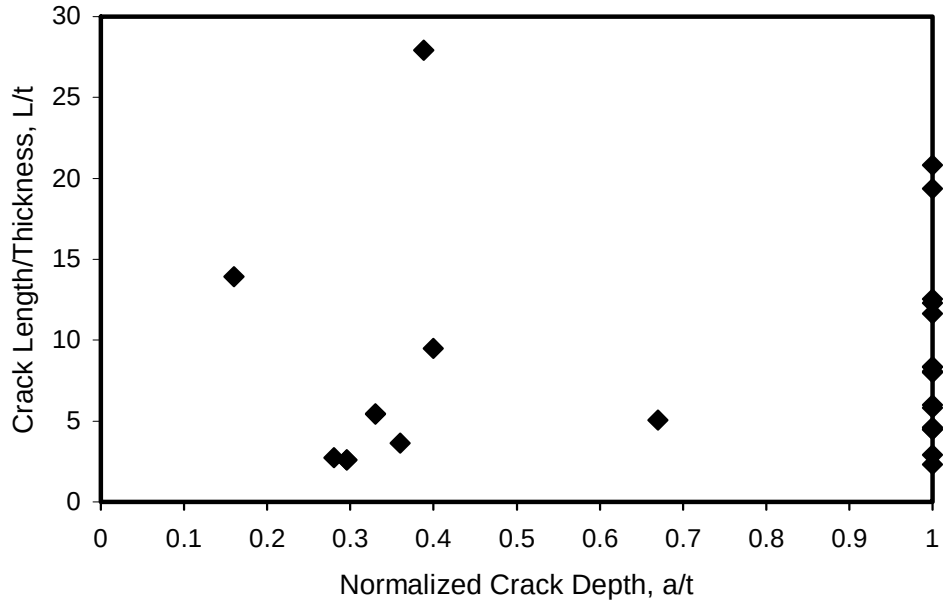


**Figure 3.2 Normalized Crack Length from Cracking Experience**

Because of the large nonlinear gradient stress profiles associated with these service conditions, cracks will tend to grow in the length direction where the highest surface cyclic stresses occur. This will cause many of these cracks to coalesce and grow as effectively larger defects. This will be discussed further in Section 6.

# 4 Improvements in Fatigue Crack Detection Capability

This section describes how experts from EPRI and PNNL used industry fatigue crack detection data to develop NDE performance-based POD curves. The fatigue crack detection data used in this study were assembled from the industry Performance Demonstration Initiative (PDI) testing results at the EPRI NDE Center in Charlotte, North Carolina. These results were used to establish a database of 16,181 NDE performance observations with 18 separate fields associated with each observation. From this database, a matrix of 42 stainless steel and 14 carbon and low-alloy steel statistically based POD curves was developed. In the matrix, each POD curve represented a combination of performance factors such as material type (stainless steel or carbon steel), access (double-sided or single-sided), section thickness, procedure (automated or manual), and inspector qualification.

Subsequent comparisons of the statistical fits for each of the POD cases showed that excellent NDE performance for fatigue cracks can be expected for ferritic materials. Very little difference was observed between the POD curves for the 14 carbon steel performance cases considered in this study, and NDE performance could therefore be represented by a single POD curve. For stainless steel, very good performance also can be expected for circumferential cracks located on the same side of the weld in which the NDE examination is made. In all these cases, inspector qualification had a small effect on the resulting POD curves. POD depended primarily on component thickness. Three POD curves for stainless steel were prepared.

During these investigations, the PDI data and PDI documentation were managed very carefully to ensure that the identity and performance of individual teams were not disclosed and the type, number, location, and sizes (depth and length) of flaws in the sample sets used for PDI were not compromised. At all times during this project, the PDI performance data remained under the control of EPRI personnel at the EPRI NDE Center. All processes were controlled according to the instructions specified in the EPRI PDI quality control procedures. The results presented in this report represent the collective statistical trends of the data and do not contain any raw PDI data, data points, or ranges of data.

## 4.1 ASME Section XI Appendix VIII

Section XI specifies the rules for conducting nondestructive inservice examinations in U.S. nuclear power plants (ASME 2004a). Between 1986 and 1989, Section XI dramatically changed its philosophy toward the ultrasonic examination requirements. Prior to the 1989 Section XI, requirements for ultrasonic examination were very prescriptive. Section XI attempted to identify and define all essential variables necessary to ensure that reliable UT practices would be used at nuclear power plants. In 1989, Section XI discontinued defining the essential variables and adopted a performance-based philosophy that relied on the qualification of UT procedures, equipment, and personnel used to detect and size flaws in piping, vessels, and bolting components. These new requirements were incorporated into Section XI in mandatory Appendix VIII, titled “Performance Demonstration for Ultrasonic Examination Systems.” These requirements apply to all personnel who detect, record, or interpret indications or size flaws in welds or components. Each organization (i.e., owner or vendor) must have a written program in place that ensures compliance with these code requirements.

The Appendix VIII requirements are organized into the following five articles:

- Article 1000 – Scope of Applicability of Appendix VIII
- Article 2000 – General Procedure and Personnel Examination System Requirements
- Article 3000 – Qualification Requirements for Detection and Sizing Tests, Essential Variables, and Requalification
- Article 4000 – Essential Variable Tolerance Requirements
- Article 5000 – Qualification and Requalification Record Requirements.

Additional mandatory requirements are provided in any one of 13 supplements to Appendix VIII. These supplements address additional requirements associated with specific material, component welds, examination processes, and other issues. For piping welds, qualification supplements are included for wrought stainless, ferritic, dissimilar metal, and weld overlay component types.

In general, NDE examination procedures, equipment, and personnel must qualify for both the detection and sizing acceptance criteria in Appendix VIII. Typically, length-sizing tests are conducted in conjunction with the detection test; however, a separate depth-sizing test is required. For piping welds, qualification is generally based on the following criteria:

- Demonstrate at least 80% detection with minimal false calls.
- The root mean squared (RMS) error between measured and true flaw length must be less than or equal to 19.1 mm (0.75 in.).
- The RMS error between measured and true flaw depth must be less than or equal to 3.2 mm (0.125 in.).

The adoption of performance-based requirements for ultrasonic inspections dramatically changed ASME Code requirements and the role of the code in procedure development. In doing so, the ASME Code shifted the responsibility of reliable procedure development to NDE engineers. The primary charter of ASME Code committees also changed. Rather than specifying procedure requirements, the code committees must focus now on developing guidance for performance demonstration testing requirements that are realistic and cost effective and will ensure reliable ultrasonic examination procedures are implemented in the field. Finally, these performance demonstration criteria now permit quantitative descriptions of the reliability of the inspector population.

## 4.2 Nuclear Industry Performance Demonstration Initiative

The nuclear industry Performance Demonstration Initiative (PDI) was formed by U.S. utilities in 1991. The program is designed to implement a unified industry approach to the performance demonstration requirements of ASME Section XI Appendix VIII. Using common protocols and sample sets, the need for site-specific performance demonstrations is minimized. Piping, bolting, and reactor pressure vessel

(RPV) shell weld performance demonstration testing began in 1994. The demonstration phase for piping and RPV shell welds has provided significant information relative to the reliability of ultrasonic examinations. Before the end of 2001, more than 500 candidates and 20 organizations had participated in the program. The numbers of measurements have exceeded 5,000 for sizing and 14,000 for piping detection and length sizing. Detection and sizing measurements for the RPV are on the order of 10% of the piping totals. Both piping and bolting statistics provide a significant database of inspection reliability information, which can provide a strong technical justification for future applications.

With the publication of the revised 10 CFR 50.55a rule on September 22, 1999, the NRC required expedited implementation of all Appendix VIII requirements. As a result, PDI has initiated activities for Phase II of the program. Phase II of the PDI program is addressing important problems that could have significant impacts on the cost and effectiveness of the U.S. performance demonstration approach. These include the nozzle inner-radius examination from the outside surface, nozzle-to-shell weld examinations, and dissimilar metal welds.

### 4.2.1 PDI Steering Committee and Working Groups

The PDI program implementation is overseen by a steering committee composed of 15 members representing 15 different U.S. utilities. All utilities owning nuclear plants in the United States are participating in the PDI. The PDI Steering Committee meets periodically with the NRC staff to discuss implementation of Appendix VIII. To address the many implementation issues, four PDI working groups were formed, made up of steering committee members and other key individuals from other utilities, ISI vendors, and the EPRI NDE Center. The Technical Working Group is responsible for the demonstration protocol, the sample matrix, and computer modeling and integrity issues. Liaison with the ASME Code is also the responsibility of the Technical Working Group. The Finance Working Group is responsible for funding acquisition, budgets, and program expenditures. The Special Projects Working Group addresses issues such as the timing for implementation, organizing industry information meetings, scheduling, and long-term administration of the demonstration program. A Quality Assurance Working Group develops guidance for the PDI QA program and monitors the quality assurance aspects of the program. EPRI and the EPRI NDE Center are providing support as requested by the committee and administering the demonstration program for PDI.

### 4.2.2 PDI Samples

The PDI program addresses the sample fabrication and operational requirements for a unified performance demonstration program operated by EPRI for the PDI Steering Committee. The PDI program has established requirements for the demonstration test blocks as well as the rules and protocol for the program operation.

The samples are a critical ingredient of the program and represent a substantial portion of the total cost. The samples are designed to cover the widest practicable range of components in U.S. plants. Detailed dimensional information was obtained and reviewed to design a sample set that spans the maximum range according to the rules in Appendix VIII that govern the range of qualifications. If a specific component configuration is not covered by the PDI samples, the affected utility may have to develop a special mock-up or investigate the use of computer modeling to cover qualification for that case.

The PDI program has developed detailed design specifications that contain requirements for sample design and fabrication, including requirements for introduction and characterization of intentional flaws. For piping, the sample sets are wrought austenitic pipe supplemented with ferritic piping samples as required. The sample sets also address PWR clad ferritic and wrought stainless steel main coolant loop piping. Austenitic specimens cover the range from 6.0 mm (0.237 in.) to 76.2 mm (3.0 in.) in thickness and diameters from 50.8 mm (2.0 in.) to 863.6 mm (34.0 in.). The ferritic specimens cover the pipe thicknesses from 8.56 mm (0.337 in.) to 95.3 mm (3.75 in.) and diameters from 101.6 mm (4.0 in.) to 1321 mm (52 in.). The piping samples used for depth sizing demonstrations are fabricated using flaw implantation techniques that provide a precise knowledge of the true flaw depth.

### 4.2.3 PDI Procedures and Documentation

The PDI Steering Committee administers the program through its direct oversight and a series of agreements, guidelines, and requirements documents. These documents include guidelines for performance demonstration, performance demonstration protocol, specimen fabrication quality assurance requirements (SFQAR), and performance demonstration process quality assurance requirements (PDPQAR). The Performance Demonstration Guidelines is the basic operating document of the Committee and includes the rules for organizing and operating the performance demonstration program. These guidelines describe the scope and purpose of the PDI program and the roles and responsibilities of the PDI, utilities, and program administrator. They contain the basic elements of the PDI performance demonstration program. The protocol document provides detailed guidance in the conduct of the actual demonstrations. The Performance Demonstration Administrator (PDA) is responsible for the development of detailed procedures to fulfill these requirements. The Steering Committee through the QA Working Group has provided detailed quality assurance (QA) requirements through the SFQAR and PDPQAR. The EPRI NDE Center, as the PDA, has written detailed programs to fulfill these requirements.

Administration of the program includes sample design and procurement, sample documentation, administering demonstrations, QA activities and audit support, and maintaining qualification records. It is expected that utility personnel will maintain oversight and periodically audit the program. Documentation that must be maintained to show compliance with the requirements of Appendix VIII includes the list of qualified essential variables for each procedure-vendor combination, sample set descriptions, and the results of the qualification demonstrations.

## 4.3 Performance Demonstration Data

Because NDE performance can be affected by several factors, the initial effort focused on identifying factors anticipated to have a significant impact on NDE performance. Based on these factors, a matrix of potential POD curve cases was assembled. Performance curves were then prepared using the S-PLUS® statistical software[(a)] for all POD cases in which the available performance data were statistically sufficient (Gosselin et al. 2005).

(a) S-PLUS® is a commercial statistical analysis software package available from Insightful Corporation, Seattle, Washington.

### 4.3.1 NDE Performance Factors

PNNL and EPRI experts in NDE, fracture mechanics, PDI data, and ASME Section XI were consulted to compile an initial listing of NDE performance factors believed to have a significant impact on POD. The following individuals provided input:

- Steve Gosselin, PNNL
- Steve Doctor, PNNL
- Fred Simonen, PNNL
- Tom Taylor, PNNL
- Larry Becker, EPRI.

The results are provided in Table 4.1. Seven primary performance factors were identified—material, crack geometry/type, NDE examination access, NDE procedure, examiner qualification, pipe diameter, and pipe wall thickness. Specific grouping conditions were identified for each of the seven primary performance factors. An initial set of PDI data assumptions and grouping recommendations was developed and then used to assemble an initial listing of POD cases.

### 4.3.2 POD Performance Curve Cases

The recommendations and assumptions in Table 4.1 resulted in 56 POD performance factor combinations—14 carbon and alloy steel cases and 42 stainless steel cases. It was determined that one-half of the POD curves (28 cases) would be based on PDI data from those examiners who passed Appendix VIII. The remaining 28 curves would be based on PDI data from all examiners (Pass + Fail). Tables 4.2 and 4.3 show how the performance factors were applied in this initial assessment for carbon and alloy steel and stainless steel, respectively. An initial listing of POD performance curve cases is provided in Tables 4.4 and 4.5.

### 4.3.3 Fatigue Crack NDE Performance Database

This section describes the NDE performance database used in the development of statistically based POD curves from the EPRI PDI data.

Each row in the database table describes what a single inspection found when a single grading unit was inspected. In other words, the basic observational unit in this table is an “inspection x grading-unit” datum. The fields included in the database were separated into three categories:

- **Inspection Fields** – These are fields that identify the inspection performed, relevant procedures used, and qualification of the inspector.

- **Grading Unit Fields** – These are fields that describe the state of the material being inspected (i.e., the grading unit). This field should include a grading unit identifier that uniquely identifies each grading unit. Examples of grading unit fields include flaw type, material type, and flaw size.

**Table 4.1 NDE Performance Factors**

| Category | Performance Factor | Comments and Assumptions |
|---|---|---|
| Material | **CS** - Carbon and Low Alloy<br>**SS** - Stainless Steel | PDI data from both carbon steel and low alloy steels may be combined. PDI stainless steel is assumed to all be wrought material. |
| Crack Geometry | **CIRC** - Circumferential crack<br>**AXIAL** - Longitudinal crack<br>**ALL** - (CIRC+AXIAL) | PDI crack geometry is expected to be a factor in SS material.<br>See comment above.<br>It is expected that CIRC and AXIAL performance factors will not be significant for carbon and low alloy steels. |
| NDE Examination Access | **SSFS** - Single-Sided access with flaw on Far Side (also referred to as "far side access")<br>**SSNS** - Single-Sided access with flaw on Near Side (also referred to as "same side access")<br>**DS** - Double-Side access | NDE examination access performance factors (SSFS, SSNS, and DS) are expected to be primarily a concern for flaws in SS piping. NDE examination access is not expected to be a significant factor of carbon and low ally steels<br>Similar performance is expected for SSNS and DS access conditions. |
| NDE Procedure | **MAN** - Manual<br>**AUTO** - Automatic | It is expected that for small bore piping <4in. (10.2 mm) NPS, automatic procedures were not used. |
| Qualification | **PASS** - Examiner passed ASME Section XI Appendix VIII qualification standards<br>**ALL** - (PASS + FAIL) | |
| Diameter<br><br>Pipe Wall Thickness | **OD1** - <102 mm (4 in.) NPS<br>**OD2** - >102 mm (4 in.) NPS<br>**T1** ≤ 10.2 mm (0.4 in.)<br>10.2 mm (0.4 in.) < **T2** ≤ 38.1 mm (1.5 in.)<br>**T3** >1.5 in. (38.1 mm) | For wall thicknesses 0.4 in. (10.2 mm) and less, the resolution issues (e.g., differentiation of cracks, crack boundary, and weld roots) become more significant. For wall thicknesses greater than 1.5 in. (38.1 mm), sound intensity attenuation becomes a more significant concern. |

## Table 4.2 Carbon and Alloy Steel POD Case Conditions

| Performance Factor Category | Condition[a] | Pipe Size ≤ 102 mm (4 in.) NPS[b] | | Pipe Size > 102 mm (4 in.) NPS[b] | |
|---|---|---|---|---|---|
| Pipe Wall Thickness | T1 | X | 1 | X | 3 |
| | T2 | | | X | |
| | T3 | | | X | |
| Crack Geometry | CIRC | | 1 | | 1 |
| | AXIAL | | | | |
| | ALL | X | | X | |
| Examination Access | SSFS | | 1 | | 1 |
| | SSNS+DS | | | | |
| | ALL | X | | X | |
| PNDE Procedure | MAN | X | 1 | X | 2 |
| | AUTO | | | X | |
| Qualification | PASS | X | 2 | X | 2 |
| | FAIL | | | | |
| | ALL | X | | X | |
| Total POD Cases[c] | | | 2 | | 12 |

(a) Conditions are defined in Table 4.1.
(b) Number of condition cases in each performance factor category from available PDI data.
(c) Equals the product of the individual condition cases in (b) columns.

## Table 4.3 Stainless Steel POD Case Conditions

| Performance Factor Category | Condition[a] | Pipe Size ≤102 mm (4 in.) NPS[b] CIRC Flaw | | Pipe Size ≤102 mm (4 in.) NPS[b] AXIAL Flaw | | Pipe Size >102 mm (4 in.) NPS[b] CIRC Flaw | | Pipe Size >102 mm (4 in.) NPS[b] AXIAL Flaw | |
|---|---|---|---|---|---|---|---|---|---|
| Pipe Wall Thickness | T1 | X | 1 | X | 1 | X | 3 | X | 3 |
| | T2 | | | | | X | | X | |
| | T3 | | | | | X | | X | |
| Crack Geometry | CIRC | X | 1 | | 1 | X | 1 | | 1 |
| | AXIAL | | | X | | | | X | |
| | ALL | | | | | | | | |
| Examination Access | SSFS | X | 2 | | 1 | X | 2 | | 1 |
| | SSNS+DS | X | | | | X | | | |
| | ALL | | | X | | | | X | |
| PNDE Procedure | MAN | X | 1 | X | 1 | X | 2 | X | 2 |
| | AUTO | | | | | X | | X | |
| Qualification | PASS | X | 2 | X | 2 | X | 2 | X | 2 |
| | FAIL | | | | | | | | |
| | ALL | X | | X | | X | | X | |
| Total POD Cases[c] | | | 4 | | 2 | | 24 | | 12 |

(a) Conditions are defined in Table 4.1.
(b) Number of condition cases in each performance factor category from available PDI data.
(c) Equals the product of the individual condition cases in (b) columns.

## Table 4.4 Stainless Steel POD Performance Curve Case Listing

| POD Case | Material | NPS Pipe Size mm (in.) | Crack Geometry | NDE Access | NDE Procedure | Qualification | Pipe Wall Thickness |
|---|---|---|---|---|---|---|---|
| SS1 | SS | <102 (4) | CIRC | SSFS | MAN | PASS | T1 |
| SS2 | SS | <102 (4) | CIRC | SSNS+DS | MAN | PASS | T1 |
| SS3 | SS | <102 (4) | CIRC | SSFS | MAN | ALL | T1 |
| SS4 | SS | <102 (4) | CIRC | SSNS+DS | MAN | ALL | T1 |
| SS5 | SS | <102 (4) | AXIAL | ALL | MAN | PASS | T1 |
| SS6 | SS | <102 (4) | AXIAL | ALL | MAN | ALL | T1 |
| SS7 | SS | >102 (4) | CIRC | SSFS | MAN | PASS | T1 |
| SS8 | SS | >102 (4) | CIRC | SSFS | MAN | ALL | T1 |
| SS9 | SS | >102 (4) | CIRC | SSFS | AUTO | PASS | T1 |
| SS10 | SS | >102 (4) | CIRC | SSFS | AUTO | ALL | T1 |
| SS11 | SS | >102 (4) | CIRC | SSNS+DS | MAN | PASS | T1 |
| SS12 | SS | >102 (4) | CIRC | SSNS+DS | MAN | ALL | T1 |
| SS13 | SS | >102 (4) | CIRC | SSNS+DS | AUTO | PASS | T1 |
| SS14 | SS | >102 (4) | CIRC | SSNS+DS | AUTO | ALL | T1 |
| SS15 | SS | >102 (4) | CIRC | SSFS | MAN | PASS | T2 |
| SS16 | SS | >102 (4) | CIRC | SSFS | MAN | ALL | T2 |
| SS17 | SS | >102 (4) | CIRC | SSFS | AUTO | PASS | T2 |
| SS18 | SS | >102 (4) | CIRC | SSFS | AUTO | ALL | T2 |
| SS19 | SS | >102 (4) | CIRC | SSNS+DS | MAN | PASS | T2 |
| SS20 | SS | >102 (4) | CIRC | SSNS+DS | MAN | ALL | T2 |
| SS21 | SS | >102 (4) | CIRC | SSNS+DS | AUTO | PASS | T2 |
| SS22 | SS | >102 (4) | CIRC | SSNS+DS | AUTO | ALL | T2 |
| SS23 | SS | >102 (4) | CIRC | SSFS | MAN | PASS | T3 |
| SS24 | SS | >102 (4) | CIRC | SSFS | MAN | ALL | T3 |
| SS25 | SS | >102 (4) | CIRC | SSFS | AUTO | PASS | T3 |
| SS26 | SS | >102 (4) | CIRC | SSFS | AUTO | ALL | T3 |
| SS27 | SS | >102 (4) | CIRC | SSNS+DS | MAN | PASS | T3 |
| SS28 | SS | >102 (4) | CIRC | SSNS+DS | MAN | ALL | T3 |
| SS29 | SS | >102 (4) | CIRC | SSNS+DS | AUTO | PASS | T3 |
| SS30 | SS | >102 (4) | CIRC | SSNS+DS | AUTO | ALL | T3 |
| SS31 | SS | >102 (4) | AXIAL | ALL | MAN | PASS | T1 |
| SS32 | SS | >102 (4) | AXIAL | ALL | MAN | ALL | T1 |
| SS33 | SS | >102 (4) | AXIAL | ALL | AUTO | PASS | T1 |
| SS34 | SS | >102 (4) | AXIAL | ALL | AUTO | ALL | T1 |
| SS35 | SS | >102 (4) | AXIAL | ALL | MAN | PASS | T2 |
| SS36 | SS | >102 (4) | AXIAL | ALL | MAN | ALL | T2 |

**Table 4.4 (contd)**

| POD Case | Material | NPS Pipe Size mm (in.) | Crack Geometry | NDE Access | NDE Procedure | Qualification | Pipe Wall Thickness |
|---|---|---|---|---|---|---|---|
| SS37 | SS | >102 (4) | AXIAL | ALL | AUTO | PASS | T2 |
| SS38 | SS | >102 (4) | AXIAL | ALL | AUTO | ALL | T2 |
| SS39 | SS | >102 (4) | AXIAL | ALL | MAN | PASS | T3 |
| SS40 | SS | >102 (4) | AXIAL | ALL | MAN | ALL | T3 |
| SS41 | SS | >102 (4) | AXIAL | ALL | AUTO | PASS | T3 |
| SS42 | SS | >102 (4) | AXIAL | ALL | AUTO | ALL | T3 |

**Table 4.5 Carbon and Alloy Steel POD Performance Case Listing**

| POD Case | Material | NPS Pipe Size mm (in.) | Crack Geometry | NDE Access | NDE Procedure | Qualification | Pipe Wall Thickness |
|---|---|---|---|---|---|---|---|
| CS1 | CS | <102 (4) | ALL | ALL | MAN | PASS | T1 |
| CS2 | CS | <102 (4) | ALL | ALL | MAN | ALL | T1 |
| CS3 | CS | >102 (4) | ALL | ALL | MAN | PASS | T1 |
| CS4 | CS | >102 (4) | ALL | ALL | MAN | PASS | T2 |
| CS5 | CS | >102 (4) | ALL | ALL | MAN | PASS | T3 |
| CS6 | CS | >102 (4) | ALL | ALL | MAN | ALL | T1 |
| CS7 | CS | >102 (4) | ALL | ALL | MAN | ALL | T2 |
| CS8 | CS | >102 (4) | ALL | ALL | MAN | ALL | T3 |
| CS9 | CS | >102 (4) | ALL | ALL | AUTO | PASS | T1 |
| CS10 | CS | >102 (4) | ALL | ALL | AUTO | PASS | T2 |
| CS11 | CS | >102 (4) | ALL | ALL | AUTO | PASS | T3 |
| CS12 | CS | >102 (4) | ALL | ALL | AUTO | ALL | T1 |
| CS13 | CS | >102 (4) | ALL | ALL | AUTO | ALL | T2 |
| CS14 | CS | >102 (4) | ALL | ALL | AUTO | ALL | T3 |

- **Result Fields** – These fields describe what the inspection found. For this study, we were interested in one principal result – "Was the flaw detected in the grading-unit?" Other results also may be useful, such as indicated flaw depth and length sizing.

The database, stored in S-PLUS®, contained 16,181 observations in 18 fields. No false call information was included. The false call performance results can be used to identify the minimum statistical POD (i.e., POD at zero crack depth). However, because the primary interest is in NDE performance when engineering-size thermal fatigue cracks are present, the lack of false call information should not influence the results. A detailed description of the database fields is summarized below.

#### 4.3.3.1 Inspection Fields

- Inspection ID – Unique identifier assigned to each inspection. There are 781 unique inspections in the database.

- PDI Procedure – This field contains EPRI's inspection procedure descriptor. There are 35 descriptors.

- Procedure – This field describes the procedure used during inspection. It distinguishes between manual (MAN) and automated (AUTO) procedures. Of the 16,181 observations contained in the database, manual procedures were used on 13,923 observations, automated procedures accounted for 2,257 observations, and finally in 1 observation the procedure field was blank.

- Qualification – This field describes whether or not the inspector passed the ASME Section XI Appendix VIII qualification. The field is assigned values of PASS or FAIL. In 51% of the observations (8,206), the inspector passed; in 49% (7,975 observations), the inspector failed to satisfy the Appendix VIII detection test acceptance criteria.

#### 4.3.3.2 Grading Unit Fields

- Grading Unit ID – This field contains a unique identifier assigned by EPRI to each specimen grading unit. It is used to incorporate pipe thickness, diameter, and schedule with all the observations.

- Material – This field describes the material type. The material types include F (ferritic material [i.e., carbon and alloy steels]) and A (austenitic stainless steel). Austenitic stainless steel was associated with 13,182 observations, and ferritic material was used in 2,999 observations in the database.

- Flaw Orientation – This field describes the flaw orientation as circumferential, C, and axial, A. The flaw orientation was circumferential in 14,561 observations and axial in 1,620 observations of the database.

- Access – This field describes inspection access of the detector relative to the location of the flaw in the grading unit. The field values are F (single-sided access from the far side of the flaw) and S (same side access or flaw near-side access). Same-side access was available in 11,193 of the grading units, and only far-side access was available in 4,988 observations. (NOTE: The case of far-sided access in stainless steel is not supported by the PDI. It has not been possible thus far to qualify procedures and personnel for flaws located on the far side of austenitic welds. As an alternative, PDI provides an opportunity for personnel and procedures to demonstrate that they can apply the best available technology now. The demonstration is a best effort approach.)

- Pipe Diameter – This field contains the test specimen pipe diameter in inches. Pipe specimen diameters range from 50.8 mm (2 in.) to 1270 mm (50 in.) NPS. The pipe diameter and the corresponding database observation counts are displayed in Table 4.6.

**Table 4.6 Fatigue Crack NDE Performance Data: Pipe Diameter Count Table**

| **Diameter mm (in.)** | 50.8 (2) | 101.6 (4) | 152.4 (6) | 304.8 (12) | 508 (20) | 609.6 (24) | 711.2 (28) | 889 (35) | 914 (36) | 940 (37) | 1270 (50) |
|---|---|---|---|---|---|---|---|---|---|---|---|
| **Count:** | 699 | 2,740 | 1,199 | 2,517 | 3,528 | 2,023 | 608 | 697 | 1,567 | 224 | 379 |

- Nominal Wall Thickness – This field identifies the nominal pipe wall thickness for the grading unit test specimen. The database pipe wall thickness and the corresponding database observation counts are shown in Table 4.7.

**Table 4.7 Fatigue Crack NDE Performance Data: Nominal Wall Thickness Count Table**

| **Thick mm (in.)** | 6.0 (.237) | 8.6 (.337) | 8.7 (.344) | 11.0 (.432) | 17.5 (.688) | 21.6 (.850) | 35.6 (1.4) | 38.1 (1.5) | 50.8 (2) | 66.7 (2.63) | 73.7 (2.9) | 79.4 (3.13) | 97.8 (3.85) |
|---|---|---|---|---|---|---|---|---|---|---|---|---|---|
| **Count** | 1,012 | 1,728 | 699 | 1,199 | 2,517 | 3,528 | 608 | 2,023 | 219 | 1,567 | 478 | 224 | 379 |

- Flaw Type – This field describes the type of flaw in the grading unit. The types of flaws contained in the database include intergranular stress corrosion cracks (IGSCC), thermal fatigue (TF), and mechanical fatigue (MF). The flaw type and the corresponding database observation counts are listed in Table 4.8.

**Table 4.8 Fatigue Crack NDE Performance Data: Flaw Type Count Table**

| **Flaw Type** | IGSCC | TF | MF |
|---|---|---|---|
| **Count** | 4,136 | 8,223 | 3,822 |

- Flaw Length – This field identifies the true maximum flaw length for the specimen.

- Flaw Depth – This field identifies the true flaw depth.

#### 4.3.3.3 Result Fields

- Detection Field – This field identified whether the flaw was detected (TRUE) or not detected (FALSE) in the grading unit. In the database, the flaw was detected in 13,467 observations and not detected in 2,714 observations.

- Length Sizing **–** This field identifies the flaw length measured during the length-sizing portion of the detection test. This field is not necessary for POD analysis and is included only for completeness.

## 4.4 Statistically Based POD Curves

POD curves were first estimated (where possible) for each case listed in Tables 4.4 and 4.5. The detection data were not sufficient to produce POD curve fits for 11 of the 42 stainless steel cases and 4 of the 14 carbon steel cases.

For stainless steel, available data for the far-side access case produces an optimistic view of inspector performance. The flaws used by PDI for far-side detection tests were selected only if they had measurable far-side ultrasonic signals. Consequently, the resulting POD curves for this category represent an upper bound performance expectation because the far-side flaws were positioned in a manner that would allow detection using current NDE methods. Since additional research will be required in order to approximate the true far-side POD on an unbiased set of flaws, it was decided to eliminate all the stainless steel far-side access cases from consideration in this study. The hypothetical fatigue flaws postulated in the Section XI Appendix L are circumferential. Therefore, POD curve cases involving axial crack geometry were eliminated for stainless steel. Crack geometry (axial versus circumferential) does not significantly affect POD for carbon steel, so circumferential and axial data were combined for this material. Appendix L focuses on circumferential flaws because axial welds are generally not present at fatigue-sensitive locations in Class 1 nuclear piping. The expected flaws are circumferential cracks. If axial cracks need to be postulated, the assumption in Appendix L is to use the same aspect ratios as specified for circumferential cracks.

Because Appendix L analyses are concerned primarily with thermal fatigue, PDI test results for inspections of intergranular stress corrosion cracking flaws were not considered in these evaluations.

Therefore, POD curve fits for 14 of the 42-stainless steel cases in Table 4.4 and 14 of the 14-carbon steel cases in Table 4.5 were evaluated in this study. The statistically based POD plots for each of these cases are provided in the Appendix.

POD curves were estimated by performing a logistic regression on detection scores using the model

$$POD(s) = logistic(\beta_1 + \beta_2 \cdot s) \tag{4.1}$$

where $s$ represents the through-wall depth of the inspected flaw. Based on trends of various flaw detection studies, it was assumed that the probability of flaw detection is insensitive to flaw length. This trend is particularly true when the flaw length is significantly greater than the flaw depth, which is the case for both natural flaws and flaws in the PDI specimens. The logistic, *logistic(z)*, function, as defined by

$$logistic(z) = (1 + \exp(-z))^{-1} \tag{4.2}$$

and the two parameters $\beta_1$ and $\beta_2$ are estimated by the fitting procedure to determine the POD curve. To estimate the parameters, the model is fitted to detection data using general least squares (equivalent to maximum likelihood). The regression uses the detection/sizing data pairs ($Y_i$, $s_i$), where the index identifies a unique flaw/inspection observation in the PDI database, and $Y_i$ represents the detection

outcome ($Y_i$ = 1 represents a detection, while $Y_i$ = 0 represents a miss). The POD curve is therefore determined from a regression equation that can be expressed as

$$Y_i = logistic(\beta_1 + \beta_2 \cdot s_i) + E_i \quad (4.3)$$

with the regression algorithm choosing $\beta$'s so that the weighted sum of squares errors are minimized.

The procedure also produces an asymptotic covariance matrix for the beta parameters, which can be used to calculate confidence bounds on the fitted curves. It should be noted that the data ($Y_i$, $s_i$) employed in the regressions does not necessarily exhibit simple random binomial variability, a characteristic that the regression model assumes. At any individual flaw size, *s*, the detection observations will consist of a complicated combination of different flaws and inspectors. The variability around *POD(s)* (as represented by $E_i$) will therefore be a complicated mixture of *flaw-to-flaw* and *inspector-to-inspector* as well as simple binomial variability. A consequence of this variability structure is to cause the fitted confidence bound to be too optimistic. A regression model that accounted for flaw-to-flaw and inspector variability would have larger confidence bounds.

Each curve was evaluated for goodness of fit to the data. Attempts were made to reconcile the curve fits with the important inspection/material variables listed in Tables 4.5 and 4.6 and explain any anomalies identified in the estimated POD curves.

The fitted POD curves were generally close to unity over the range of flaw sizes present in the PDI data. In general, the PDI data were not very good at determining the "breakdown" flaw sizes for the inspection procedures; that is, the flaw sizes for which the POD begins to rapidly decrease. The false call scores for passing teams must be below 20%. Therefore, the "statistical POD" curves should intersect the y-axis at some point below 20%. Because no PDI performance data were available for very small flaw sizes (i.e., through-wall depth [TWD] much less than 10%), none of the fitted curves modeled POD well for small flaw sizes.

When the POD fits for each of the cases listed in Appendix A were compared to the variables that defined the cases (e.g., material type, pipe thickness), the following conclusions were reached:

1. *Available performance data for each fit are statistically adequate.* The POD curve fits generally explain the data over the 10% to 100% flaw size region, although there is some evidence of some significant deviations caused by flaw-to-flaw variations.

2. *The effects of pipe diameter cannot be separated from pipe thickness*. Pipe diameter and pipe thickness vary together in the samples, so it is impossible to determine which variable has an effect on POD. From knowledge of ultrasonic principles, one can conclude that the thickness effects should dominate the diameter effects for circumferential flaws. Therefore, thickness was retained and pipe diameter was excluded.

3. *Procedure type is insignificant*. Although there was some indication that automatic procedures had a higher POD than manual procedures, a decision was made to collapse the cases across procedure type.

4. *Combining PASS and FAIL data is most reasonable*. It would be most valuable to estimate the POD performance for passing individuals, and to achieve this end one would naturally include PASS test results in the calculation. Originally, POD curves were calculated using only PASS test results to estimate this performance. However, it was pointed out that a typical test candidate took the test more than once before passing, so the performance would be best estimated using both passed and failed tests. As a result, both passed and failed data were combined in the POD curve calculations even though these data include results from inspectors who were unsuccessful.

5. *All cases for ferritic materials can be collapsed*. Performance for ferritic materials is uniformly good, so all ferritic cases were combined to form one curve giving POD as a function of percent through-wall crack depth.

These conclusions allowed the performance cases listed in Tables 4.5 and 4.6 to be reduced to just four cases, which are defined by the variables "material" and "pipe thickness." The cases are

- CASE 1: Austenitic Stainless Steel, Pipe Thickness, $T1 \leq 10.2$ mm (0.4 in.)
- CASE 2: Austenitic Stainless Steel, Pipe Thickness, 10.2 mm (0.4) < $T2$ < 38.1 mm (1.5 in.)
- CASE 3: Austenitic Stainless Steel, Pipe Thickness, $T3 \geq 38.1$ mm (1.5 in.)
- CASE 4: Carbon and Low-Alloy Steel, All Pipe Thicknesses.

The POD curves associated with these four cases are plotted in Figures 4.1 through 4.4. To allow the reader to see a complete set of statistical curves for the four cases, Figures 4.1 through 4.4 have been combined into Figure 4.5, and the corresponding logistic regression data in Table 4.9 are provided for the full range of through-wall depth (0% to 100%). However, the curves are not considered realistic for flaw sizes less than 10% through-wall depth. The corresponding logistic regression data for each curve also is provided in Table 4.9 (Gosselin et al. 2002, 2005). Each figure plots the best estimate POD curve (solid line) and associated 95% confidence bounds (broken line) against through-wall depth. As one can see, Cases 1 and 4 generally display very little change in POD with TWD, and the POD is quite near 1. The other two cases (2 and 3) exhibit lower POD, and POD varies by about 20 percentage points between large and small flaws. Cases 1, 2, and 3 show that pipe thickness has an effect on POD. It should be emphasized that these curves provide legitimate estimates for POD only in the region where data exist, which is in the 10% to 100% TWD range for these curves.

Comparisons of the best-estimate logistic fits are shown in Figure 4.5 for Cases 1, 2, 3, and 4. It is seen that for smaller crack sizes, the performance for the ferritic case is better than all of the stainless steel cases. This is consistent with expectations. The performance for the thinnest stainless steel category T1 was better than that for the thicker T2 and T3 categories. Because the material path for ultrasonic beam transmission is less for the thinner sections, these results are also expected. However, for the same TWD cracks, better performance was observed for the thicker T3 stainless steel samples than for the intermediate thickness T2 samples. Although not shown here, the T2 and T3 curves tend to approach one another when POD is plotted against actual crack depth. Therefore it would appear that this difference is caused by the larger physical crack sizes in the T3 samples and the corresponding uncertainties associated with the smaller number of observations at these larger crack sizes.

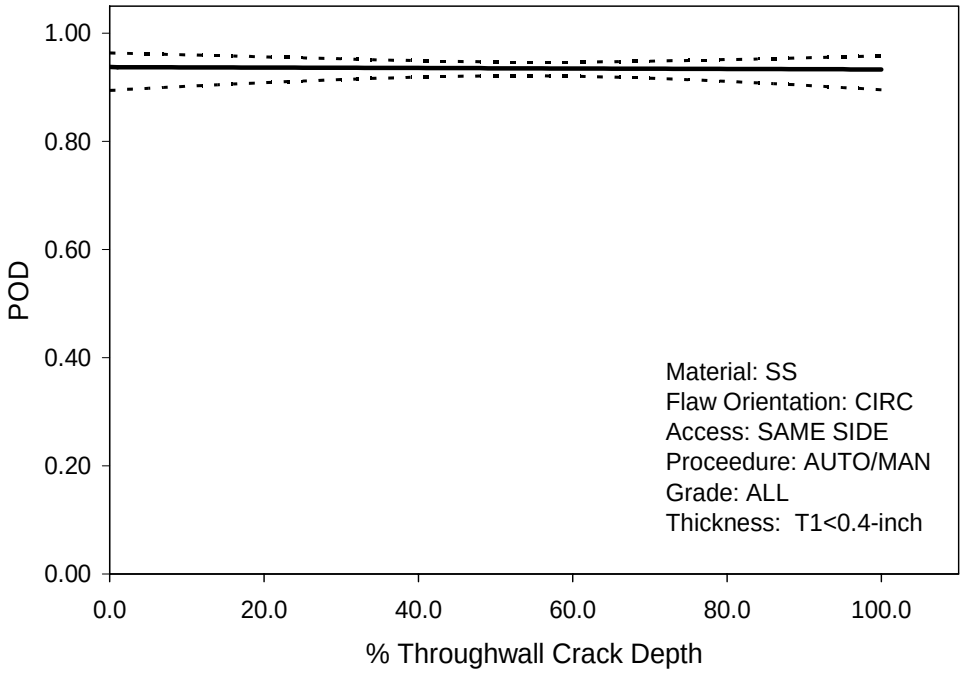


**Figure 4.1 Case 1 Austenitic Stainless Steel Best-Estimate (solid line) and 95% Confidence (broken line) POD Curves for Thickness <10.2 mm (0.4 in.)**

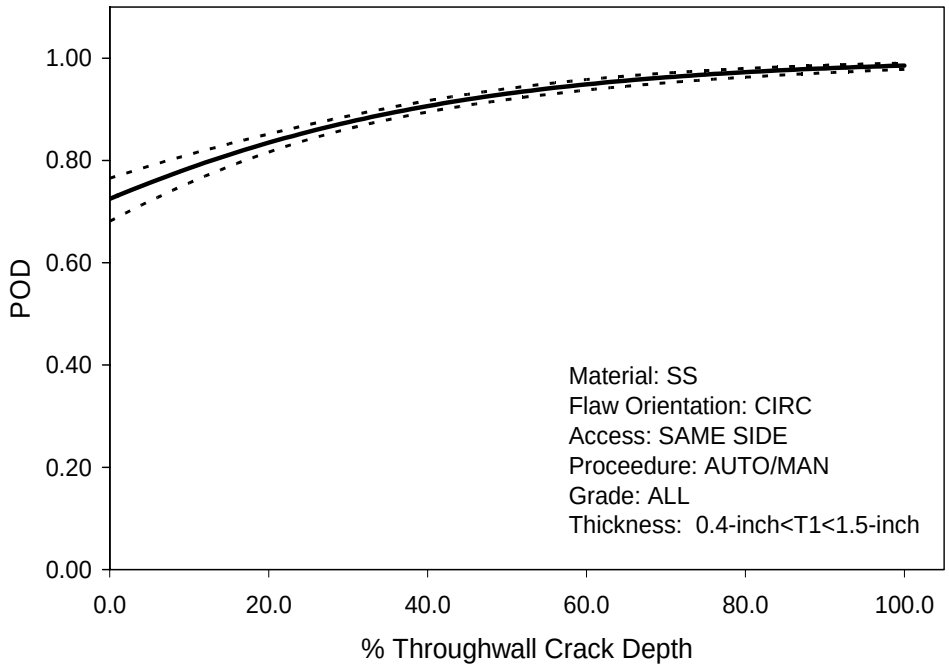


**Figure 4.2 Case 2 Austenitic Stainless Steel Best-Estimate (solid line) and 95% Confidence (broken line) POD Curves for Thickness 10.2 mm (0.4 in.) to 38.1 mm (1.5 in.)**

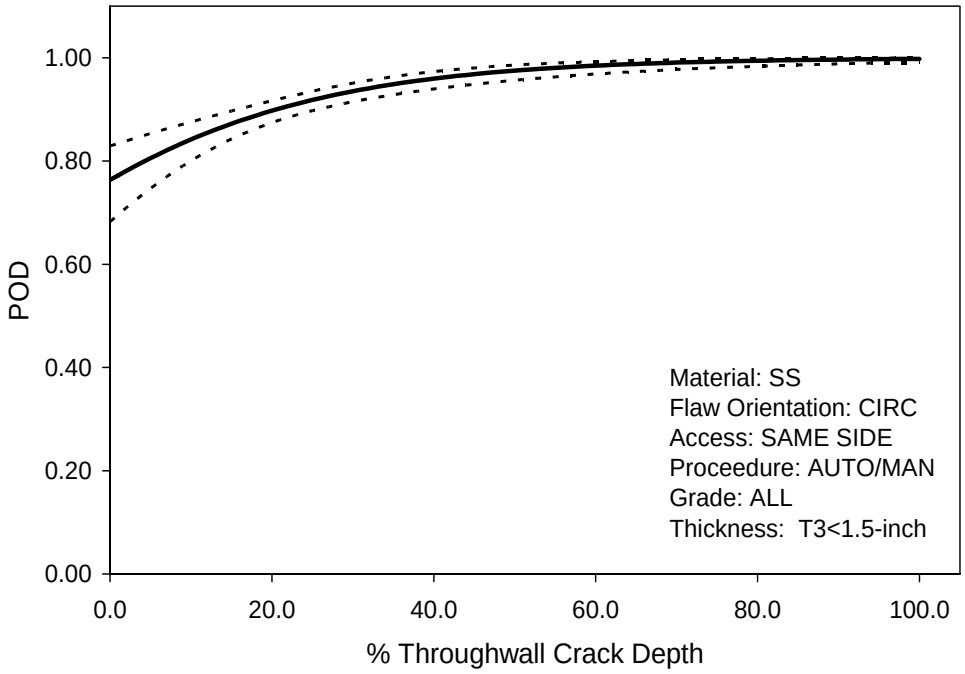


**Figure 4.3 Case 3 Austenitic Stainless Steel Best-Estimate (solid line) and 95% Confidence (broken line) POD Curves for Thickness >38.1 mm (1.5 in.)**

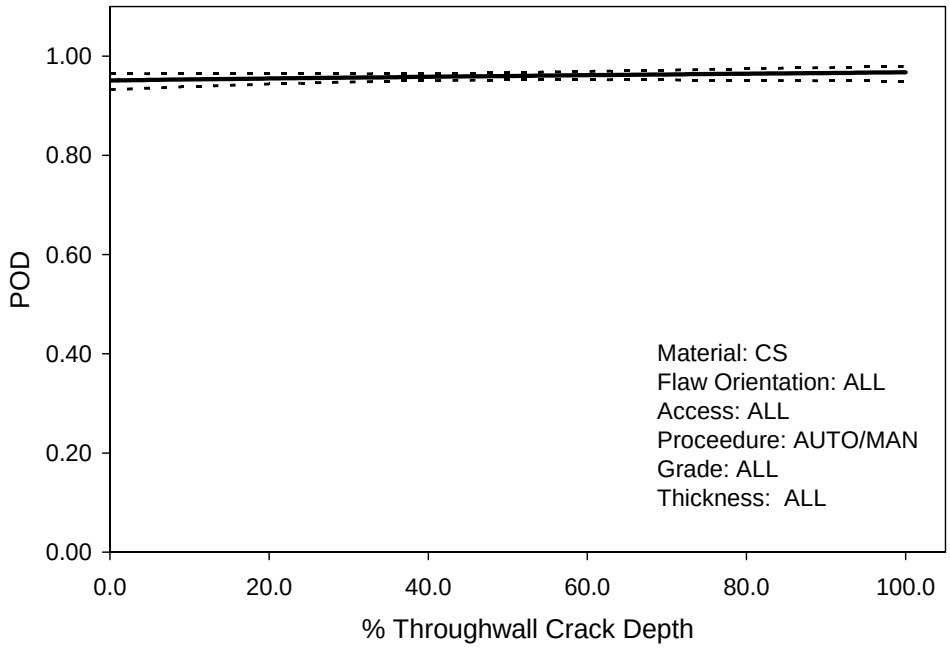


**Figure 4.4 Case 4 Carbon and Low Alloy Steel Best-Estimate (solid line) and 95% Confidence (broken line) POD Curves for All Thicknesses**

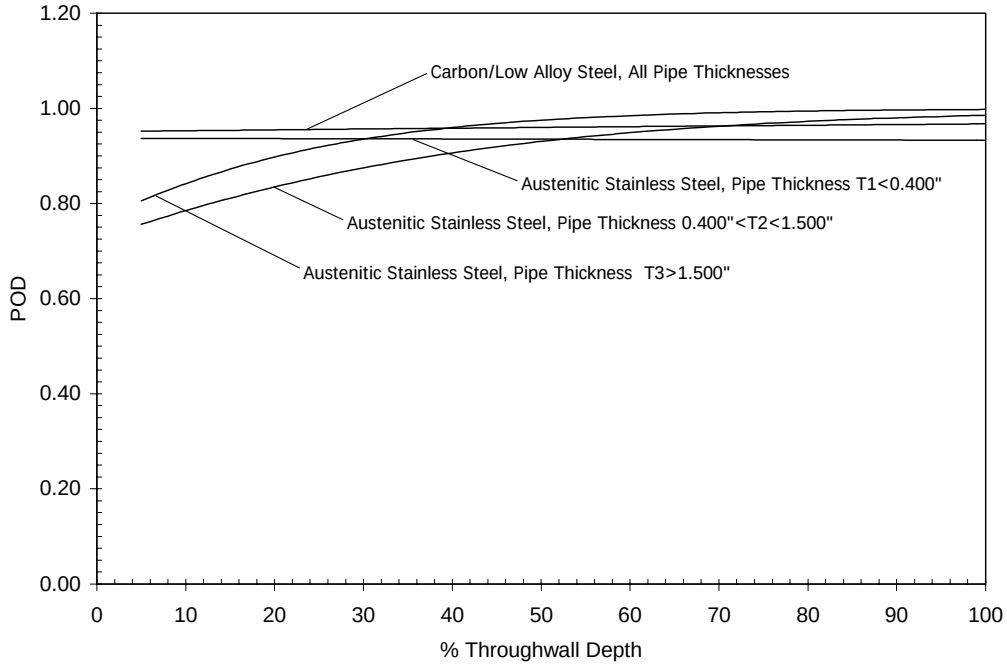


**Figure 4.5 Best-Estimate Logistic Curve Fits for Cases 1, 2, 3, and 4**

For large TWD values, the POD for cracks in the T2 and T3 thickness is better than for the thinner T1 samples. More significantly, the POD estimates for both the T2 and T3 stainless steel cases tend to approach/exceed the performance measured for the ferritic material cases. These results are suspect because the physics associated with ultrasonic inspections of austenitic stainless steel materials would never predict that NDE performance for stainless would be better than that for ferritic materials. As it turns out, the number of tests associated with the larger crack depth-to-thickness ratios in the T2 and T3 specimens was small and the uncertainties associated with the best-estimate fits in these ranges were very large. In comparison, the uncertainties associated with the ferritic cases and the smaller size stainless steel cracks were much smaller.

## 4.5 Concluding Remarks

The initial NDE performance demonstration evaluations and POD curves developed in this report represent the first step in trying to answer a very basic question: "How reliable are nuclear system piping inspections in the field??" One of the challenges in answering this question is relating the performance models developed in this project to the performance expectations in the field.

The PDI program has generated a large amount of data that can be used to derive NDE performance relative to combinations of controlling performance variables. Because the PDI inspection teams use common testing procedures/inspection protocols and inspection-equivalent equipment, added confidence can be obtained in statistical calculations based on these performance data. Also the knowledge gained from PDI performance data has allowed the relative difficulty of assembled test specimen sets to be

**Table 4.9 Logistic Regression Results for PDI Fatigue Crack Detection Performance Data**

| % Depth | Case 1 LOW | Case 1 MEAN | Case 1 HIGH | Case 2 LOW | Case 2 MEAN | Case 2 HIGH | Case 3 LOW | Case 3 MEAN | Case 3 HIGH | Case 4 LOW | Case 4 MEAN | Case 4 HIGH |
|---|---|---|---|---|---|---|---|---|---|---|---|---|
| 0.0 | 0.89426 | 0.93733 | 0.96357 | 0.68104 | 0.72497 | 0.76493 | 0.68242 | 0.76339 | 0.82890 | 0.93227 | 0.95104 | 0.96480 |
| 2.0 | 0.89582 | 0.93725 | 0.96288 | 0.69706 | 0.73774 | 0.77472 | 0.70945 | 0.78095 | 0.83885 | 0.93356 | 0.95143 | 0.96468 |
| 4.0 | 0.89735 | 0.93716 | 0.96218 | 0.71257 | 0.75012 | 0.78425 | 0.73485 | 0.79755 | 0.84848 | 0.93482 | 0.95182 | 0.96455 |
| 6.0 | 0.89886 | 0.93707 | 0.96147 | 0.72755 | 0.76211 | 0.79353 | 0.75851 | 0.81319 | 0.85781 | 0.93604 | 0.95220 | 0.96444 |
| 8.0 | 0.90033 | 0.93699 | 0.96075 | 0.74197 | 0.77369 | 0.80255 | 0.78038 | 0.82788 | 0.86686 | 0.93722 | 0.95258 | 0.96433 |
| 10.0 | 0.90178 | 0.93690 | 0.96003 | 0.75582 | 0.78487 | 0.81133 | 0.80043 | 0.84165 | 0.87567 | 0.93837 | 0.95296 | 0.96423 |
| 12.0 | 0.90319 | 0.93682 | 0.95929 | 0.76908 | 0.79565 | 0.81987 | 0.81865 | 0.85450 | 0.88427 | 0.93949 | 0.95334 | 0.96414 |
| 14.0 | 0.90457 | 0.93673 | 0.95855 | 0.78175 | 0.80601 | 0.82817 | 0.83507 | 0.86648 | 0.89268 | 0.94057 | 0.95371 | 0.96406 |
| 16.0 | 0.90592 | 0.93665 | 0.95781 | 0.79382 | 0.81598 | 0.83624 | 0.84974 | 0.87761 | 0.90091 | 0.94160 | 0.95408 | 0.96399 |
| 18.0 | 0.90723 | 0.93656 | 0.95706 | 0.80529 | 0.82554 | 0.84409 | 0.86277 | 0.88794 | 0.90897 | 0.94261 | 0.95445 | 0.96394 |
| 20.0 | 0.90851 | 0.93648 | 0.95631 | 0.81615 | 0.83470 | 0.85172 | 0.87428 | 0.89749 | 0.91683 | 0.94357 | 0.95481 | 0.96390 |
| 22.0 | 0.90974 | 0.93639 | 0.95555 | 0.82642 | 0.84348 | 0.85915 | 0.88443 | 0.90632 | 0.92442 | 0.94448 | 0.95517 | 0.96388 |
| 24.0 | 0.91095 | 0.93630 | 0.95480 | 0.83610 | 0.85187 | 0.86637 | 0.89339 | 0.91446 | 0.93168 | 0.94536 | 0.95553 | 0.96388 |
| 26.0 | 0.91210 | 0.93622 | 0.95405 | 0.84520 | 0.85989 | 0.87339 | 0.90135 | 0.92195 | 0.93854 | 0.94618 | 0.95589 | 0.96391 |
| 28.0 | 0.91322 | 0.93613 | 0.95330 | 0.85375 | 0.86754 | 0.88021 | 0.90846 | 0.92884 | 0.94495 | 0.94696 | 0.95624 | 0.96396 |
| 30.0 | 0.91428 | 0.93604 | 0.95257 | 0.86176 | 0.87483 | 0.88684 | 0.91487 | 0.93516 | 0.95087 | 0.94769 | 0.95659 | 0.96403 |
| 32.0 | 0.91530 | 0.93596 | 0.95184 | 0.86926 | 0.88178 | 0.89325 | 0.92069 | 0.94096 | 0.95629 | 0.94837 | 0.95694 | 0.96414 |
| 34.0 | 0.91626 | 0.93587 | 0.95113 | 0.87628 | 0.88839 | 0.89945 | 0.92600 | 0.94627 | 0.96121 | 0.94899 | 0.95728 | 0.96428 |
| 36.0 | 0.91716 | 0.93578 | 0.95045 | 0.88286 | 0.89468 | 0.90543 | 0.93089 | 0.95112 | 0.96565 | 0.94955 | 0.95763 | 0.96446 |
| 38.0 | 0.91799 | 0.93570 | 0.94979 | 0.88903 | 0.90065 | 0.91117 | 0.93540 | 0.95556 | 0.96963 | 0.95006 | 0.95796 | 0.96467 |
| 40.0 | 0.91874 | 0.93561 | 0.94917 | 0.89482 | 0.90631 | 0.91667 | 0.93957 | 0.95961 | 0.97319 | 0.95051 | 0.95830 | 0.96492 |
| 42.0 | 0.91941 | 0.93552 | 0.94859 | 0.90027 | 0.91169 | 0.92192 | 0.94345 | 0.96331 | 0.97637 | 0.95090 | 0.95864 | 0.96520 |
| 44.0 | 0.92000 | 0.93543 | 0.94806 | 0.90540 | 0.91679 | 0.92692 | 0.94705 | 0.96668 | 0.97919 | 0.95123 | 0.95897 | 0.96552 |
| 46.0 | 0.92048 | 0.93535 | 0.94759 | 0.91024 | 0.92161 | 0.93166 | 0.95042 | 0.96975 | 0.98169 | 0.95152 | 0.95930 | 0.96588 |
| 48.0 | 0.92085 | 0.93526 | 0.94719 | 0.91481 | 0.92618 | 0.93615 | 0.95356 | 0.97254 | 0.98390 | 0.95175 | 0.95963 | 0.96626 |
| 50.0 | 0.92111 | 0.93517 | 0.94687 | 0.91913 | 0.93051 | 0.94039 | 0.95649 | 0.97509 | 0.98585 | 0.95193 | 0.95995 | 0.96668 |

**Table 4.9 (contd)**

| % Depth | Case 1 LOW | Case 1 MEAN | Case 1 HIGH | Case 2 LOW | Case 2 MEAN | Case 2 HIGH | Case 3 LOW | Case 3 MEAN | Case 3 HIGH | Case 4 LOW | Case 4 MEAN | Case 4 HIGH |
|---|---|---|---|---|---|---|---|---|---|---|---|---|
| 52.0 | 0.92124 | 0.93508 | 0.94663 | 0.92323 | 0.93459 | 0.94438 | 0.95923 | 0.97740 | 0.98758 | 0.95207 | 0.96027 | 0.96712 |
| 54.0 | 0.92125 | 0.93500 | 0.94649 | 0.92710 | 0.93846 | 0.94814 | 0.96180 | 0.97950 | 0.98910 | 0.95216 | 0.96059 | 0.96758 |
| 56.0 | 0.92111 | 0.93491 | 0.94643 | 0.93078 | 0.94211 | 0.95168 | 0.96420 | 0.98141 | 0.99043 | 0.95223 | 0.96091 | 0.96807 |
| 58.0 | 0.92085 | 0.93482 | 0.94647 | 0.93427 | 0.94555 | 0.95499 | 0.96645 | 0.98315 | 0.99161 | 0.95225 | 0.96122 | 0.96856 |
| 60.0 | 0.92046 | 0.93473 | 0.94659 | 0.93758 | 0.94880 | 0.95810 | 0.96856 | 0.98473 | 0.99264 | 0.95225 | 0.96154 | 0.96907 |
| 62.0 | 0.91994 | 0.93464 | 0.94680 | 0.94073 | 0.95187 | 0.96101 | 0.97053 | 0.98616 | 0.99355 | 0.95223 | 0.96184 | 0.96959 |
| 64.0 | 0.91931 | 0.93455 | 0.94709 | 0.94372 | 0.95476 | 0.96373 | 0.97238 | 0.98746 | 0.99435 | 0.95218 | 0.96215 | 0.97011 |
| 66.0 | 0.91856 | 0.93447 | 0.94744 | 0.94655 | 0.95749 | 0.96627 | 0.97412 | 0.98863 | 0.99505 | 0.95210 | 0.96246 | 0.97064 |
| 68.0 | 0.91772 | 0.93438 | 0.94785 | 0.94925 | 0.96006 | 0.96864 | 0.97574 | 0.98970 | 0.99566 | 0.95201 | 0.96276 | 0.97117 |
| 70.0 | 0.91678 | 0.93429 | 0.94832 | 0.95181 | 0.96248 | 0.97086 | 0.97727 | 0.99067 | 0.99620 | 0.95191 | 0.96306 | 0.97170 |
| 72.0 | 0.91576 | 0.93420 | 0.94883 | 0.95424 | 0.96476 | 0.97292 | 0.97870 | 0.99155 | 0.99668 | 0.95179 | 0.96336 | 0.97223 |
| 74.0 | 0.91466 | 0.93411 | 0.94937 | 0.95656 | 0.96690 | 0.97485 | 0.98004 | 0.99235 | 0.99709 | 0.95165 | 0.96365 | 0.97276 |
| 76.0 | 0.91349 | 0.93402 | 0.94995 | 0.95875 | 0.96892 | 0.97664 | 0.98129 | 0.99307 | 0.99745 | 0.95151 | 0.96395 | 0.97329 |
| 78.0 | 0.91225 | 0.93393 | 0.95055 | 0.96084 | 0.97082 | 0.97831 | 0.98247 | 0.99372 | 0.99777 | 0.95135 | 0.96424 | 0.97381 |
| 80.0 | 0.91095 | 0.93384 | 0.95117 | 0.96283 | 0.97261 | 0.97987 | 0.98357 | 0.99432 | 0.99805 | 0.95118 | 0.96453 | 0.97432 |
| 82.0 | 0.90960 | 0.93375 | 0.95180 | 0.96471 | 0.97429 | 0.98131 | 0.98460 | 0.99485 | 0.99829 | 0.95100 | 0.96481 | 0.97483 |
| 84.0 | 0.90819 | 0.93366 | 0.95244 | 0.96650 | 0.97587 | 0.98266 | 0.98557 | 0.99534 | 0.99851 | 0.95082 | 0.96510 | 0.97534 |
| 86.0 | 0.90672 | 0.93357 | 0.95310 | 0.96821 | 0.97735 | 0.98391 | 0.98648 | 0.99578 | 0.99869 | 0.95063 | 0.96538 | 0.97584 |
| 88.0 | 0.90522 | 0.93348 | 0.95375 | 0.96982 | 0.97875 | 0.98507 | 0.98733 | 0.99618 | 0.99886 | 0.95043 | 0.96566 | 0.97633 |
| 90.0 | 0.90366 | 0.93339 | 0.95442 | 0.97136 | 0.98006 | 0.98615 | 0.98813 | 0.99654 | 0.99900 | 0.95022 | 0.96594 | 0.97681 |
| 92.0 | 0.90206 | 0.93330 | 0.95508 | 0.97282 | 0.98129 | 0.98715 | 0.98888 | 0.99687 | 0.99912 | 0.95001 | 0.96621 | 0.97729 |
| 94.0 | 0.90041 | 0.93321 | 0.95574 | 0.97421 | 0.98245 | 0.98809 | 0.98958 | 0.99717 | 0.99923 | 0.94980 | 0.96649 | 0.97776 |
| 96.0 | 0.89873 | 0.93312 | 0.95641 | 0.97552 | 0.98353 | 0.98895 | 0.99024 | 0.99743 | 0.99933 | 0.94957 | 0.96676 | 0.97822 |
| 98.0 | 0.89700 | 0.93303 | 0.95707 | 0.97677 | 0.98455 | 0.98975 | 0.99085 | 0.99768 | 0.99941 | 0.94935 | 0.96703 | 0.97867 |
| 100.0 | 0.89523 | 0.93294 | 0.95772 | 0.97796 | 0.98551 | 0.99050 | 0.99143 | 0.99790 | 0.99949 | 0.94912 | 0.96729 | 0.97912 |

controlled in a consistent manner. However, when used to develop POD models, there are limitations. These limitations stem primarily from the fact that both Appendix VIII and the PDI implementation program were designed as a qualification screening process in which minimum threshold acceptance criteria are applied to NDE inspector test results and were not designed to specifically determine/measure POD. The more significant of these limitations are as follows:

- The treatment of far-side access in stainless steel specimens may not represent all conditions expected to occur in the field. Because of the difficulties associated with inspecting stainless steel welds when inspection access is limited to the far side, each PDI test specimen was screened to ensure that the far-side flaw was detectable using the best available technology. Therefore, the performance results represent a best effort and are applicable only to cases in which far-side flaws in stainless steel welds can be detected. Additional research will need to be completed in order to relate these conditional results to POD expectations in the field.

- The flaws selected for Appendix VIII performance demonstration tend to be planar and do not include flaws with depths significantly below 10% through-wall thickness (i.e., below the flaw acceptance criteria in ASME Section XI Table IWB-3410-1). Consequently, assumptions were needed regarding the shape of the POD curves below 10% through-wall thickness. As described in Section 5, the POD curves from the statistical correlations were extrapolated down to flaw depths of 5% through-wall thickness. A linear interpolation was used for flaw depths between zero depth (with POD = 0.0) and the 5% depth.

- The performance results that were based on observations only in the PASS qualification category (i.e., observations in which the inspector passed the Appendix VIII requirements) are optimistically high. In many cases, these same inspectors also contributed to the failed observation counts, and the inspector's performance is expected to degrade between requalification periods because most examinations in the field are performed on good materials that rarely have recordable defects.

- There exists a wide range of field conditions, many of which are not directly represented in the PDI test specimen sets and test conditions.

- The inspector acts alone during the performance testing rather than as part of a team in the field where he would receive additional input when characterizing and sizing defects.

These preliminary results support the following conclusions:

- Excellent NDE performance for fatigue cracks can be expected for ferritic materials. Very little difference was observed between the POD curves for all the ferritic cases considered in this study. Therefore, NDE performance can be represented by a single POD curve.

- Very good performance can be expected also for circumferential cracks in stainless steel when the crack is located on the same side of the weld in which the NDE examination is made. For these conditions, POD depended primarily on component thickness. In all these cases, inspector qualification had a small effect on the resulting POD curves.

- A POD curve with an asymptotic upper limit at large flaw sizes appears to be justified. Therefore, these data will be very useful in helping to improve existing asymptotic factors currently assumed in pc-PRAISE and other probabilistic fracture mechanics software.

- Because the PDI data are limited to flaw sizes greater than 5% through-wall depth, future analyses will need to consider false call probabilities to better define the shape of the POD curves at very small flaw sizes.

Future analyses will need to compare these POD results with those obtained from earlier performance round-robin studies (e.g., pipe inspection round robin, Programme for the Inspection of Steel Components [PIRR, PISC]). These comparisons can be used to help quantify the performance improvements associated with the implementation of Appendix VIII and its contribution to improving reactor safety (i.e., reduction in core damage frequency).

# 5 Evaluation of Improved Detection Capability on Leakage Probability

This section describes calculations performed by PNNL to examine how component reliability (i.e., leakage probabilities) is affected when the improved POD curves in Section 4 are assumed for different inspection strategies.

The calculations were performed using an enhanced version of the pc-PRAISE probabilistic fracture mechanics computer code (Khaleel et al. 2000). The pc-PRAISE calculations of through-wall crack frequencies account for benefits of inservice inspections. This feature was originally implemented into the fatigue crack initiation version of pc-PRAISE. Although the operational capability of the ISI model was verified, it was not needed for the scope of work documented in NUREG/CR-6674 (Khaleel et al. 2000). Because the calculations described in this report represent the first significant application of the new ISI capability with new POD curves, additional enhancements were necessary to facilitate the calculations in this report.

The probabilistic fracture mechanics calculations were based on the design loadings in NUREG/CR-6260 (Ware et al. 1995) for a 76.2-mm (3-in.) NPS Schedule 160 charging line nozzle in a Westinghouse pressurized water reactor (PWR). The sensitivity calculations included an evaluation of the relative contributions to failure probabilities of preexisting fabrication flaws versus fatigue cracks initiated by service-related fatigue stresses. Several inspection strategies, PDI performance-based POD curves, and corresponding pc-PRAISE POD error function parameters ($a^*$, $\varepsilon$, and $\nu$) were considered in this study.

## 5.1 Modifications to pc-PRAISE Code

To facilitate the calculations described in this report, PNNL implemented several additional changes to the NUREG/CR-6674 version of the pc-PRAISE code.

### 5.1.1 Dimension and Output Changes

Dimension statements in pc-PRAISE were changed to increase the maximum number of inservice inspection occurrences from 8 to 100. Print statements were added to pc-PRAISE to provide data on crack sizes as a function of time so that the code could be applied in a deterministic manner. The code was changed to allow fractional years as output intervals if the user provides a table of times at which output is desired and allows up to 200 output times per run.

### 5.1.2 Preexisting Crack Simulations

The code was modified to predict failure probabilities for preexisting cracks to be calculated with the same logic used to simulate failure due to initiated fatigue cracks. This permitted the improved input format for stress transients (developed only for the initiation model) to be used to address preexisting cracks. In this case, the number of cycles to initiate a crack was internally set to one cycle so a crack

appears as soon as the first stress cycle occurs, and the size of the initiated crack was assigned to a value simulated from a lognormal distribution of flaw depths rather than being assigned a fixed flaw depth.

### 5.1.3 S-N Cycles-to-Failure

Additional enhancements were made to pc-PRAISE to include a fatigue life fraction (SNFACTOR) adjustment to the Argonne National Laboratory (ANL) S-N fatigue curve cycles-to-failure. This option allowed the simulation of initiated crack depths other than the 3 mm (0.118 in.) crack depth associated with the ANL S-N curves.

### 5.1.4 Crack Initiation and Growth Correlation

In pc-PRAISE, the manner in which initiated cracks around the circumference are correlated is defined by the user through a control variable IICORR. In order to support many of the aspect ratio sensitivity calculations in Section 6, an additional user option for IICORR was added to pc PRAISE. By setting IICORR = 2, the inside surface cracks about the circumference are correlated in the following manner:

- The equations for predicting crack growth rates (da/dN) for all cracks around the circumference of each simulated weld are assigned a common value.

- The fatigue crack initiation times (XITIME) for all cracks around the circumference of each simulated weld are assigned a common simulated initiation time.

- Flaw half-length minus flaw depth ($c - a$) for all the cracks in each of the simulated welds have common simulated values of flaw length. However, the values of ($c - a$) are simulated and allowed to vary from weld-to-weld.

- The values of common da/dN and XITIME are sampled to simulate different values from weld to weld.

### 5.1.5 Improved POD Input for PFM Software

Improved POD input for pc-PRAISE software is shown in Figure 5.1. For each case, the best-estimate logistic regression data was applied between 5% and 100% TWD. A linear extrapolation was assumed below 5% TWD. Because no credit is taken for false calls, the POD curves are assumed to start at zero POD and 0% TWD. In light of the uncertainties associated with the T2 and T3 stainless steel cases at larger crack sizes, it was decided to limit the maximum POD estimates for stainless steel to be less than or equal to the POD performance measured for ferritic steel. In essence, this places an upper limit on the maximum POD of approximately 97% for the T2 and T3 stainless steel cases.

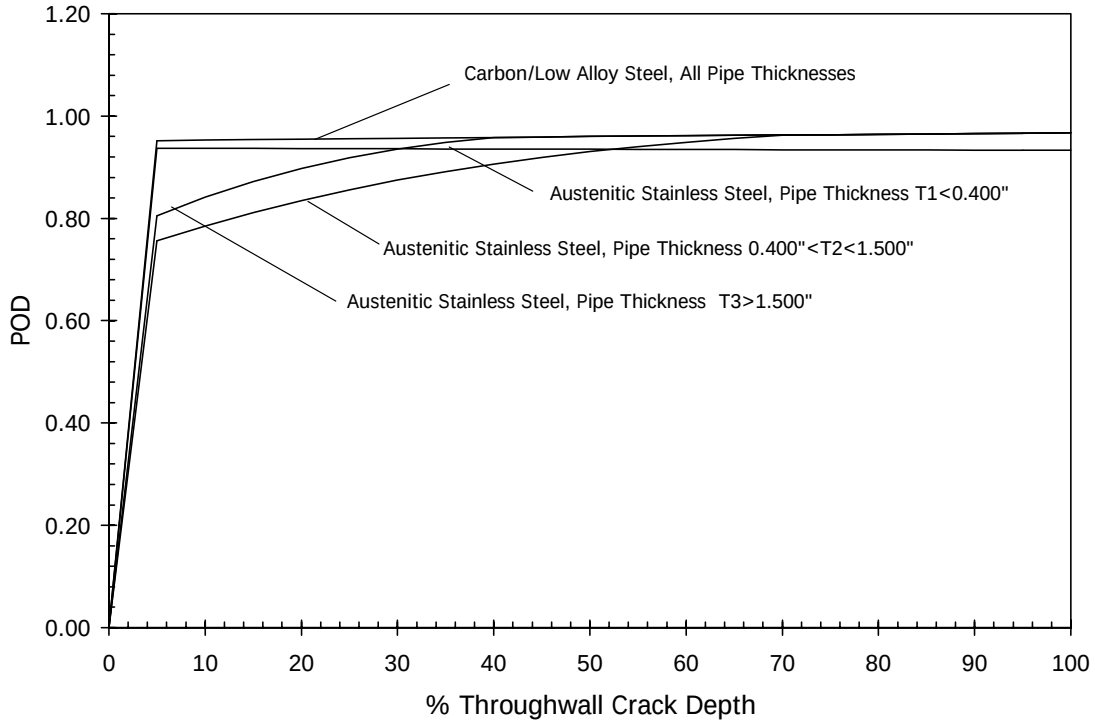


**Figure 5.1 pc-PRAISE PDI Performance-Based POD Curves for all Carbon and Austenitic Stainless Steel Piping (25.4 mm = 1.0 in.)**

## 5.2 Methodology for Through-Wall Crack Calculations

Calculations were performed to estimate the probability that fatigue cycles will result in through-wall cracks and leaks to the pressure boundary of piping components. The current study focuses on the contribution of *initiated* fatigue cracks but also provides estimates of the contributions of *pre-existing* cracks. The crack initiation methodology consists of two parts. The first part calculates the probability that fatigue cracks will initiate as a function of time over the operating life of the plant. The second part evaluates the probability that these initiated cracks will grow to become through-wall cracks.

Stress amplitudes and the numbers of stress cycles are provided as inputs to the probabilistic calculations of piping failure probabilities. The number of cycles to crack initiation is a function of the number and severity of these stress cycles and the material type, water/air environment, temperature, dissolved oxygen content, sulfur content, and strain rate. The material types addressed by pc-PRAISE are carbon steel, low-alloy steel, 304/316 austenitic stainless steel, and 316NG stainless steel. The statistical models of NUREG/CR-6335 (Keisler et al. 1995) are used to calculate the number of cycles to crack initiation corresponding to given probabilities (or percentiles) of the material S-N curves.

The crack propagation was assumed to start from a 3 mm (0.118 in.) deep initiated flaw, which can then grow to the critical size (through-wall) for component failure. This initiation flaw size was the crack size estimated to give a measurable 25% load drop in standard fatigue test specimens. Sensitivity calculations

were performed by PNNL to evaluate the effect of changing this crack depth from 3 mm (0.118 in.) to 2 mm (0.078 in.) or 4 mm(0.157 in.). The resulting changes in the calculated probabilities of through-wall cracks were at most a factor of two. It was decided to exclude the initial crack depth as a simulated variable, in part because the uncertainty in the initial crack depth is indirectly captured by the statistical scatter in the data based on the load drop approach used to define crack initiation.

The cyclic stress levels from piping stress reports (Ware et al. 1995) can be used to calculate both crack initiation and crack growth. However, it should be noted that these stresses included effects of stress concentrations in a manner prescribed by the ASME Code and the effects of through-wall stress gradients due to radial thermal gradients. In many cases, the stress indices addressed very high local stresses (e.g., weld root stress concentrations) with values up to 2.0. Because surface stresses are not indicative of internal stress levels remote from the peak stresses, adjustments are made by pc-PRAISE for deeper cracks to account for the effects of the through-wall stress variations. Cyclic stresses are broken into uniform stress components and thermal gradient stress components in accordance with the set of rules described in NUREG/CR 6674 and later summarized in this report.

### 5.2.1 Fatigue Crack Initiation

The pc-PRAISE code fatigue crack initiation model in NUREG/CR-6674 estimates the probability of initiating a 3-mm-deep (0.118 in.) fatigue crack. This model incorporates the fatigue life models developed by ANL and reported in NUREG/CR-6335. These models are based on existing fatigue (S-N) data, foreign and domestic, for carbon, low-alloy, and stainless steels used in the construction of nuclear power plant components. Only data obtained on smooth specimens tested under fully reversed loading conditions were considered. A lognormal statistical distribution was fit by ANL to the S-N data to describe the scatter in the fatigue data. The parameters of the probabilistic fatigue initiation curves were based on the ANL revised fatigue curves published in NUREG/CR-6335. The equations for stainless steels included recent updates for fatigue life correlations provided to PNNL by ANL.

The equations for cycles to failure were coded as a FORTRAN subroutine for implementation into probabilistic fracture mechanic codes such as pc-PRAISE. The calling program provides values for the stress amplitude, material type, sulfur content (for ferritic steels), temperature, whether the environment is water or air, dissolved oxygen content of the water, and the strain rate for the stress cycle.

Figure 5.2 was generated from data obtained from a series of calls to the subroutine. Each of the curves corresponds to the indicated percentile of data having cycles to failure less than or equal to the indicated percentile. The solid curve of Figure 5.2 is the median or $50^{th}$ percentile curve for cycles to crack initiation. All inputs for strain rates, dissolved oxygen, and sulfur were assigned as bounding values that are unlikely to be present simultaneously at these maximum values for any given component.

#### 5.2.1.1 Fatigue Crack Initiation Depth

The ANL S-N model associates fatigue life with a surface flaw depth of about 3 mm (Chopra and Shack 2001, Chopra 2002, Gavenda et al. 1997) and is based on consideration of the 25% load drop criteria used to denote fatigue failure of smooth push-pull specimens in fatigue testing procedures. Consequently, for a given alternating stress or strain, these S-N curves represent the number of cycles

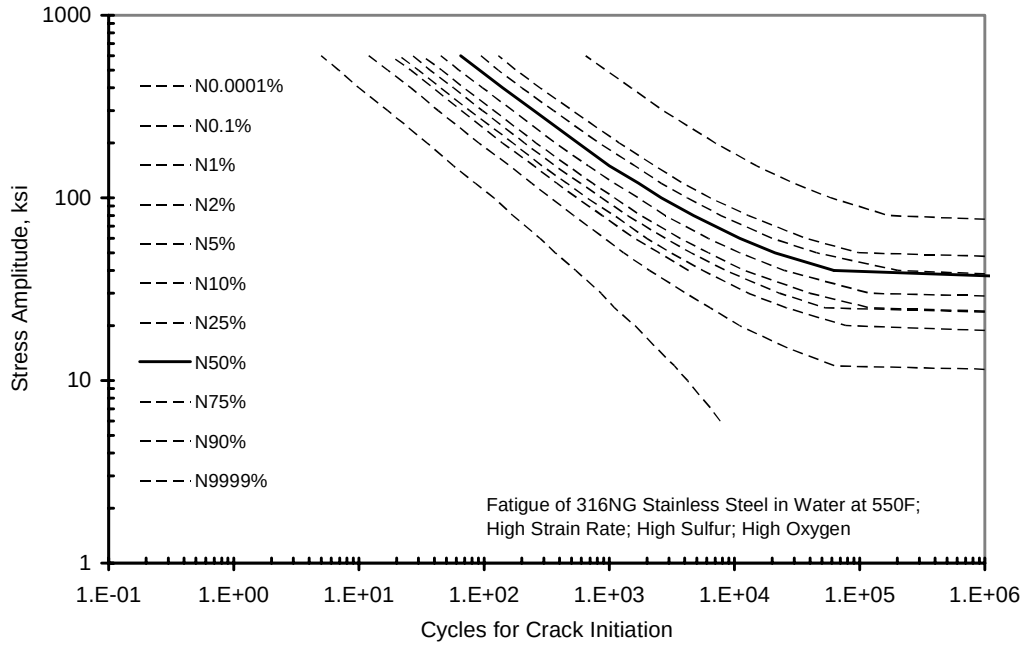


**Figure 5.2 Example of Probabilistic S-N Curves for Type 316NG Stainless Steel**

necessary to initiate and subsequently grow a crack to a 3-mm (0.118 in.) depth. A 3 mm (0.118 in.) deep crack in a 76.2 mm (3 in.) Schedule 160 pipe corresponds to approximately 27% TWC depth and represents considerable crack growth beyond crack initiation.

In NUREG/CR-6717, Chopra and Shack (2001) provide a discussion of the fatigue crack initiation mechanism in piping and pressure vessel steels. The growth of surface cracks may be divided into two regimes: an initial period, Stage I, which involves growth of microstructurally small cracks (MSC) and a propagation period, Stage II, which involves growth of mechanically small cracks that can be predicted by fracture mechanics methodologies. Stage I has been defined as the "initiation stage," and Stage II has been defined as the "propagation stage." Schematic illustrations (Gavenda et al. 1997) of the growth and velocity of small cracks in smooth specimens as a function of fatigue life fraction are shown in Figures 5.3 and 5.4. The transition from the initiation stage to the propagation stage occurs over a crack depth range from 0.15 mm (0.005 in.) to 0.25 mm (0.01 in.) (Chopra and Shack 2001; Chopra 2002).

For this example, an initiation crack depth of 0.5 mm (0.02 in.) was selected. This crack depth is near the start of the propagation region, yet sufficiently greater than the transition range to ensure that the subsequent crack growth can be predicted by linear elastic fracture mechanics (LEFM).

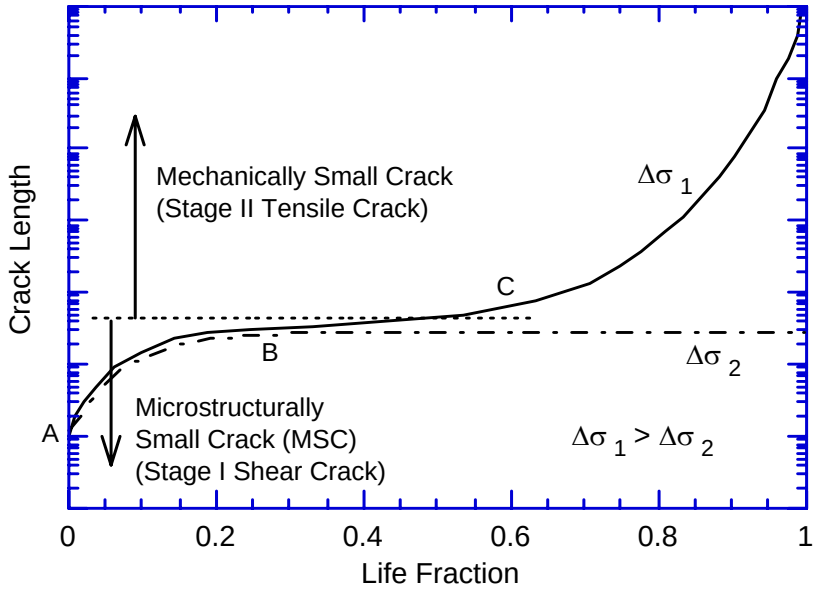


**Figure 5.3 Growth of Cracks in Smooth Fatigue Specimens (Chopra and Shack 2001; Gavenda et al. 1997)**

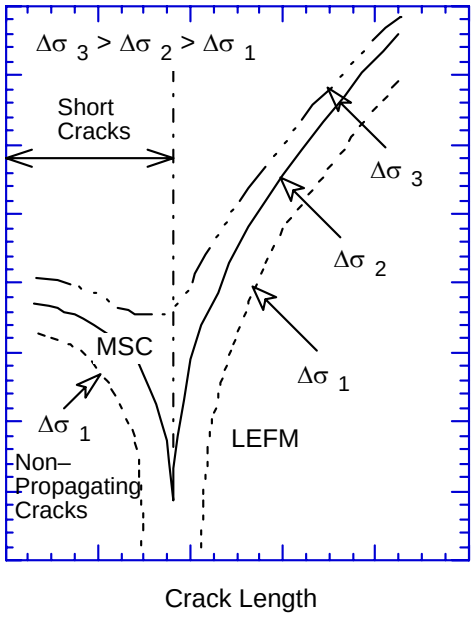


**Figure 5.4 Crack Velocity as a Function of Crack Length (Chopra and Shack; Gavenda et al. 1997)**

#### 5.2.1.2 Fraction of S-N Curve Fatigue Life - SNFACTOR

Sensitivity calculations were performed to determine the fraction of the ANL S-N curve fatigue life that would be associated with an initiation crack depth of 0.5 mm (0.02 in.) rather than a depth of 3 mm (0.118 in.). TWC probability calculations assumed that six cracks initiated around the inside

circumference. In all cases, da/dN, S-N cycles to failure, and the median crack shape ($c - a$) were correlated about the circumference. This way, for each replication all six cracks initiated at the same time with the same length and grew at the same rate. The TWC probability for a 3-mm (0.118 in.) initiation crack depth with no reduction on S-N curve cycles-to-failure (SNFACTOR = 1) was first determined. Three other cases were run where the initiation crack depth was reduced to 0.5 mm (0.02 in.) and the S-N curve cycles to failure were reduced by SNFACTORS of 0.3, 0.4, and 0.5. The resulting TWC probabilities are compared in Figure 5.5. In this case, the TWC probability for the 0.5 mm (0.02 in.) initiation crack depth with a SNFACTOR = 0.3 was the same as when the initiation crack depth was 3 mm (0.118 in.) and the SNFACTOR was equal to one.

In a recent study, Chopra (2002) examined crack depth as a function of fatigue cycles for smooth austenitic stainless steel push pull specimens in light water reactor (LWR) coolant environments. A plot of the largest crack depth as a function of fatigue cycles for austenitic stainless steels in air and water is shown in Figure 5.6. These results show that the number of cycles required to produce a 0.5 mm (0.02 in.) and 3 mm (0.118 in.) crack in a PWR environment are approximately 800 and 2,600, respectively, and suggest that the fraction of fatigue life for a 0.5 mm (0.02 in.) crack would be approximately 0.31.

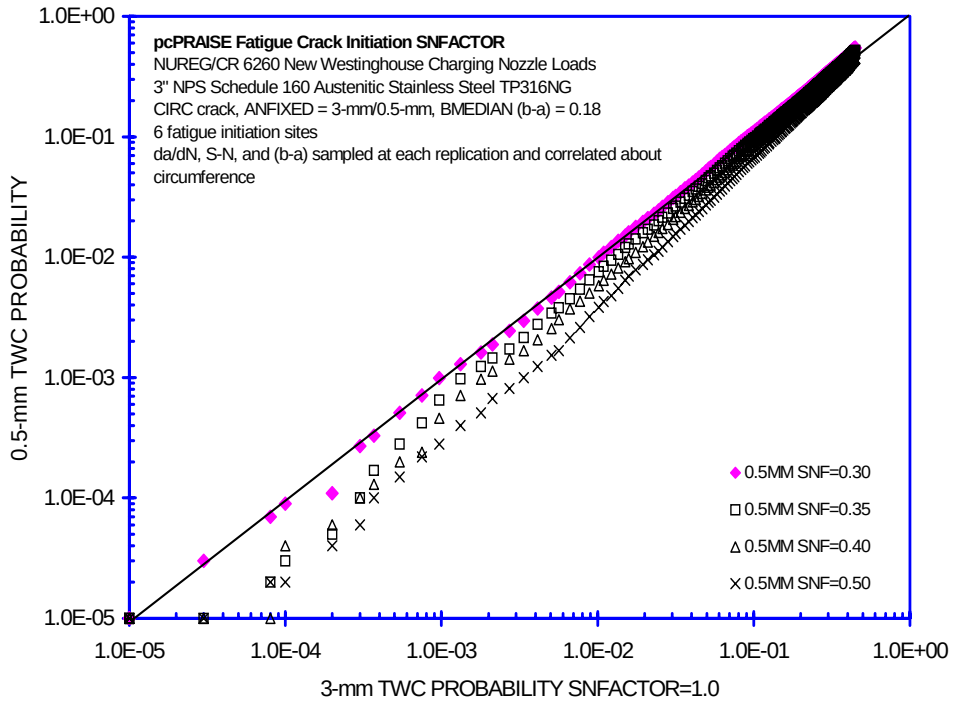


**Figure 5.5 pc-PRAISE SNFACTOR for 0.5-mm (0.02 in.) Initiated Crack Depth (25.4 mm = 1 inch)**

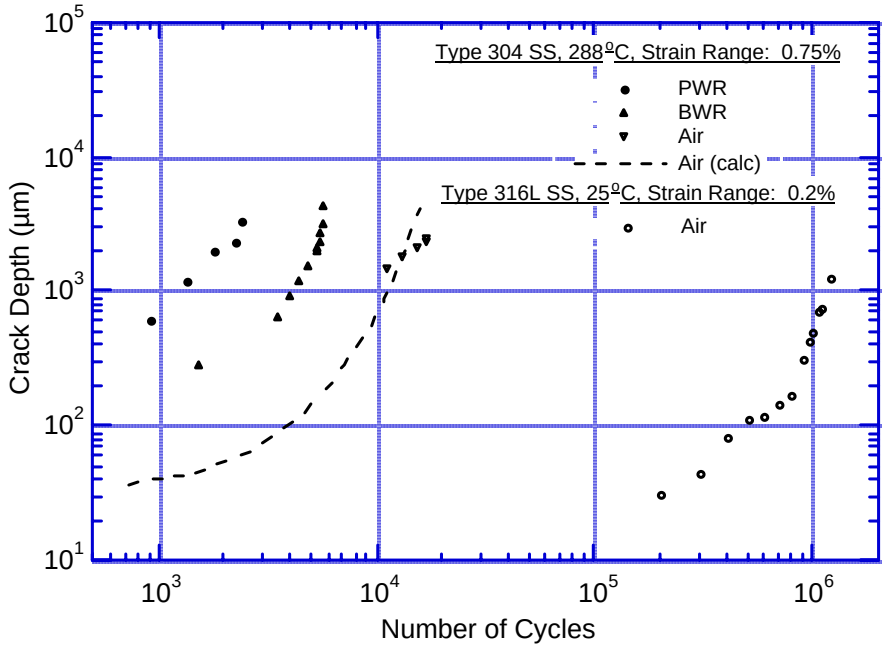


**Figure 5.6 Depth of Largest Crack Plotted as a Function of Fatigue Cycles for Austenitic Stainless Steels in Air and Water (Chopra 2002a, 2002b)**

#### 5.2.1.3 Multiple Crack Initiation

The enhanced version of pc-PRAISE addresses crack initiation at multiple sites by subdividing the pipe circumference into a set of zones 50.8 mm (2 in.) long. The amplitude of cyclic stresses at each site can vary in a manner specified by user input such that the fatigue cracks may initiate at some sites much sooner or later than at other sites. The model also assumes no correlation between the random scatter in crack initiation times from one site to the next. Thus, a different selection from the family of S-N curves (as shown by the example of Figure 5.2) is sampled at random for each of the various sites around the pipe circumference.

The enhanced version of pc-PRAISE simulates the initiation of fatigue cracks at multiple sites around the circumference of a weld, a phenomenon often seen in service-induced cracking of pipe welds. Details of this part of the fracture mechanics model are described in NUREG/CR-6674. The crack growth calculations simulate the growth (depth and length) of the individual cracks and combine adjacent cracks into a single larger crack in accordance with proximity rules.

### 5.2.2 Treatment of Size Effects

The equations developed by ANL to predict probabilities of fatigue-crack initiation are based on a statistical treatment of data from tests of small specimens. An additional term, *ln(4)*, is included to bring the equation into empirical agreement with some test data on 228.6 mm (9 in.) diameter vessels. This term is intended to account for size, geometry, and surface-finish differences between small fatigue test specimens and actual components.

The pc-PRAISE model accounts for multiple initiation sites with each site covering some 50.8 mm (2 in.) of the pipe circumference. The probability of crack initiation therefore increases as the number of specified initiation sites is increased. This means that the fracture-mechanics model itself indirectly accounts for size effects, and inclusion of the *ln(4)* term of the ANL equation can result in a double counting of size effects. Therefore, the *ln(4)* term of the ANL equation was modified when used to address crack initiation at multiple sites. The pc-PRAISE multiple-site model was calibrated to achieve agreement of calculated cycles to crack initiation with experimental data from the tests of the 228.6 mm (9 in.) diameter vessels described in the ANL reports. The conclusion from this calibration effort was that the cycles to failure from the ANL equation needed to be increased by a factor of about 3.0. The net result was a factor of 3/4 applied to the number of cycles to failure from the small-specimen data. In contrast, the ANL equation uses a factor of 1/4, but bases the fatigue-life prediction on consideration of a single initiation site.

### 5.2.3 Fatigue Crack Growth

As for crack initiation, the calculations for fatigue crack growth were based on data that accounted for the effects of environment on the growth rates. The equations for fatigue crack growth rates were unchanged from the previous version of the pc-PRAISE code (Harris and Dedhia 1992). These equations did not address the specific factors that enhance the crack growth rates in the same level of detail and rigor as in the ANL correlations for crack initiation.

For this study, the fatigue crack growth rates were calculated using the existing stainless steel crack growth law in the pc-PRAISE code (Harris et al. 1981). The environmentally enhanced fatigue crack growth rate data as a function of effective stress intensity factor, along with the least square curve-fit used for the pc-PRAISE crack growth law, are shown in Figure 5.7. The fatigue crack growth rate in pc-PRAISE is given by

$$\frac{da}{dN} = C\left[\frac{\Delta K}{(1-R)^{\frac{1}{2}}}\right]^m$$

where $\Delta K$ = $K_{max} - K_{min}$, $MPa\sqrt{m}$ $(ksi\sqrt{inch})$

$R$ = $K_{min} / K_{max}$

$C$ = lognormally distributed constant = $10.04 \times 10^{12}$ m / cycle / $MPa\sqrt{m}$ or $1.59 \times 10^{-13}$ $MPa\sqrt{m}$ $(9.14 \times 10^{-12}$ in / cycle / $ksi\sqrt{inch})$

$K_{max}$ = maximum stress intensity factor during the transient $MPa\sqrt{m}$ $(ksi\sqrt{inch})$

$K_{min}$ = minimum stress intensity factor during the transient $MPa\sqrt{m}$ $(ksi\sqrt{inch})$

$a$ = crack depth m (in.)

$N$ = number of fatigue cycles

$m$ = crack growth exponent.

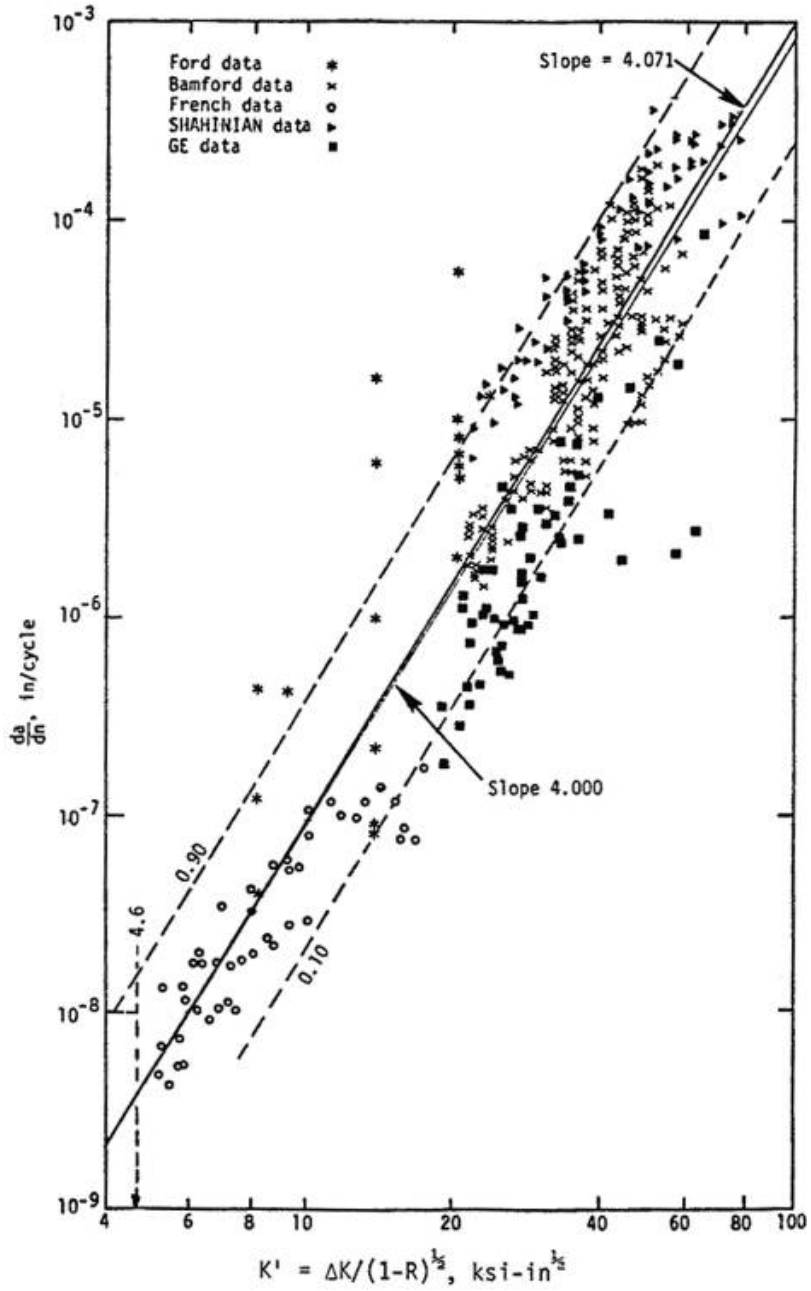


**Figure 5.7 Fatigue Crack Growth Rate Data as a Function of Effective Stress Intensity and Least Squares Curve Fit (Harris et al. 1981)**

The literature suggests that the crack growth rates for stainless steel in water, at lower rates of cycling, can be greater that those assumed in pc-PRAISE. However, in this evaluation, high strain rate loading transients are assumed along with a PWR water environment. Therefore, it is assumed that the existing pc-PRAISE crack growth model is considered reasonable. A crack growth $\Delta K$ threshold of $5.06\ \text{MPa}\sqrt{\text{m}}$ ($4.6\ \text{ksi}\sqrt{\text{inch}}$) was assumed.

The random variations in fatigue crack-growth rates were not correlated with the random variations in the cycles to crack initiation. If such correlations were to exist, the predictions for probabilities of through-wall cracks could be nonconservative as indicated by sensitivity calculations described below. The simplifying assumption greatly facilitated the calculations and has a good technical basis because the technical literature (Wire and Li 1996) provides evidence to support the assumption of independence. In general, crack initiation and crack growth involve different material damage mechanisms, such that environment and loading rates affect the mechanisms for crack initiation and growth differently.

It was assumed that crack growth occurred under conditions of zero R-ratio. While this assumption will be conservative for transients with very high stress amplitudes, crack-growth rates for cases of high-cycle/low-stress fatigue could be underestimated. The pc-PRAISE model for predicting multiple crack initiations from site to site around the circumference of a given weld also assumed that random variations in the number of cycles to crack initiation were uncorrelated from site to site.

### 5.2.4 Treatment of Through-Wall Stress Gradients

Inputs for cyclic stresses can be taken from piping stress reports as was done in the NRC-funded research project at Idaho National Laboratory (INL) as described in NUREG/CR-6260. Such data give only peak stresses for the surface locations at which the initiation of fatigue cracks is evaluated and do not describe the corresponding variations of the stresses through the section thickness. It is appropriate to use these peak stresses for the initiation aspect of fatigue cracking. However, it is unrealistic to assume that these peak stresses are uniformly distributed through the thickness of the component.

The approach used for the current calculations was to decompose the peak stress into a component of uniform stress and a component of through-wall gradient stress. Details of the approach are described in NUREG/CR-6674. A standardized (quadratic) stress gradient was developed based on stress solutions for heating and cooling ramps and step changes in surface temperatures.

Because results of detailed stress calculations were not available from the work of NUREG/CR-6260, rules were developed by PNNL to assign only a fraction of the peak stress to the uniform stress category. The remaining fraction was assigned to the through-wall gradient category. In many cases, the values of peak stresses can be greater than 690 MPa (100 ksi), which implies that most of the stresses are due to heating and cooling transients or are due to geometric stress concentrations. In other cases, the number of stress cycles can be very large, which also suggests thermal transients. Another consideration is that the ASME Code limits do not permit membrane stresses (including secondary stresses) to be more than three times the code design stress (i.e., $<3S_m$). For typical piping materials, the $3S_m$ limit implies that all stress ranges (or $2S_a$) greater than 45 ksi should be treated as gradient stresses.

The rules used to assign stresses to the uniform and gradient categories were as follows:

- Seismic stresses were treated as 100% uniform stress.

- Stresses greater than 310 MPa (45 ksi) were treated as having a uniform component of 310 MPa (45 ksi), with the remainder being assigned to the gradient category.

- For transients with more than 1,000 cycles over a 40-year life, it was assumed that 50% of the stress was uniform stress and 50% through-wall gradient stress. In addition, the uniform stress component was not permitted to exceed 69 MPa (10 ksi).

These rules are significantly more realistic than assuming a uniform stress through the full thickness of the component. The approach described above ensures that shallow initiated cracks will at first be subjected to the peak surface stresses but allows for a reduction in crack-growth rates as the cracks grow into regions of lower stress levels.

## 5.3 Charging Line Nozzle Design Conditions

The charging line nozzle in a Westinghouse PWR connects the charging inlet piping from the chemical and volume control system (CVCS) to the reactor coolant system (RCS) cold legs; see Figure 5.8 (Gosselin et al. 2002; Simonen and Gosselin 2001). During plant operation, these cold leg injection locations are used to maintain the required water inventory in the RCS by maintaining programmed water level in the pressurizer (PZR). Charging flow is initiated, and the normal letdown flow path is established through the letdown orifices. A continuous feed (charging) and bleed (letdown) stream is maintained to and from the RCS. The charging flow rate is automatically controlled to maintain liquid level in the pressurizer. A constant letdown rate is established through the selection of a specific combination of flow orifices. A simple sketch of the CVCS is shown in Figure 5.9 (Gosselin et al. 2002).

Letdown water leaves the RCS and flows through the shell side of the regenerative heat exchanger where it gives up its heat to makeup water being returned to the RCS. The letdown water then flows through letdown orifices where its pressure is reduced, then through a nonregenerative heat exchanger, followed by a second pressure reduction by a low-pressure letdown valve. After passing through a mixed-bed demineralizer where ionic impurities are removed, the water flows through the reactor coolant filter and into the volume control tank via a spray nozzle. The charging pumps take the coolant from the volume control tank and send it back to the RCS through the tube side of the regenerative heat exchanger where it is reheated before entering the RCS cold legs.

### 5.3.1 Design Temperature Transients

The more significant temperature variations in the charging line downstream of the regenerative heat exchanger can be due to any one or combination of the following changes (Simonen and Gosselin 2001):

- Condition A: variations in the letdown and/or charging line flow rates
- Condition B: variation in the charging temperature upstream of the regenerative heat exchanger
- Condition C: variations in the letdown temperature upstream of the regenerative heat exchanger.

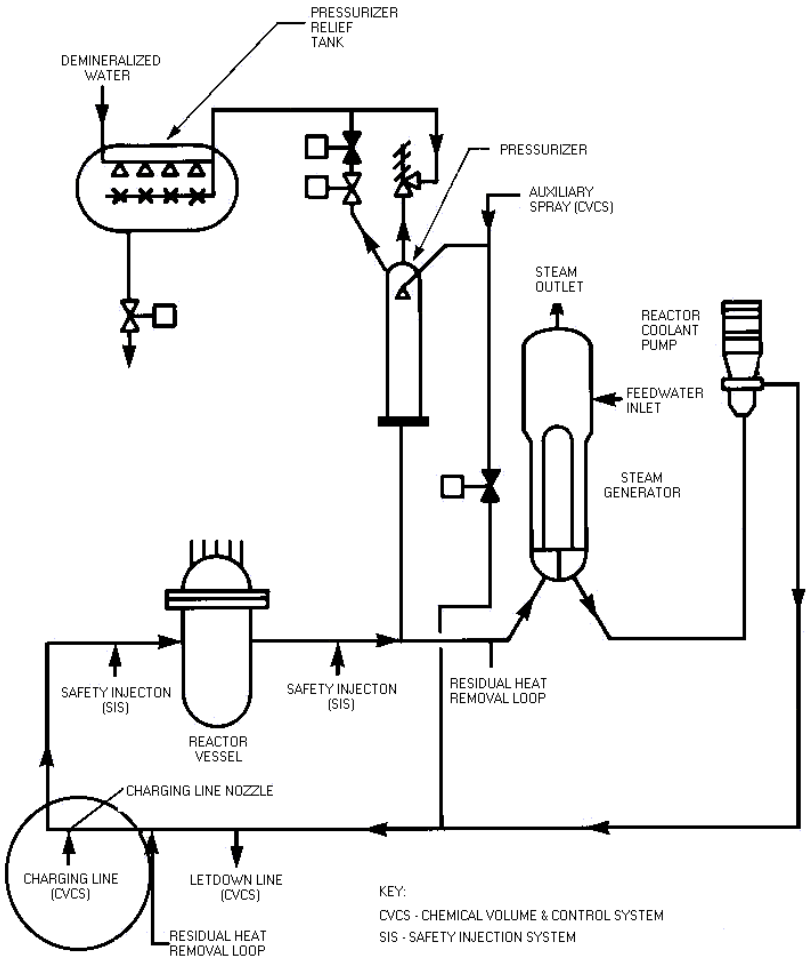


**Figure 5.8 Westinghouse PWR Primary Coolant Loop (Gosselin et al. 2002; Simonen and Gosselin 2001)**

Because letdown normally is drawn from the cold leg, these temperature variations reflect the variations in $T_{cold}$. Because normal temperature variations in the RCS cold legs are comparatively minor, transient conditions associated with Condition C are typically not considered in Class 1 charging line nozzle fatigue analyses. For the most part, the operating transients relating to Conditions A and B that tend to dominate the charging line nozzle design fatigue usage include the following:

- normal charging and letdown shutdown and subsequent return to service
- loss of charging and subsequent return to service
- charging flow increase and subsequent decrease
- letdown flow increase and subsequent decrease.

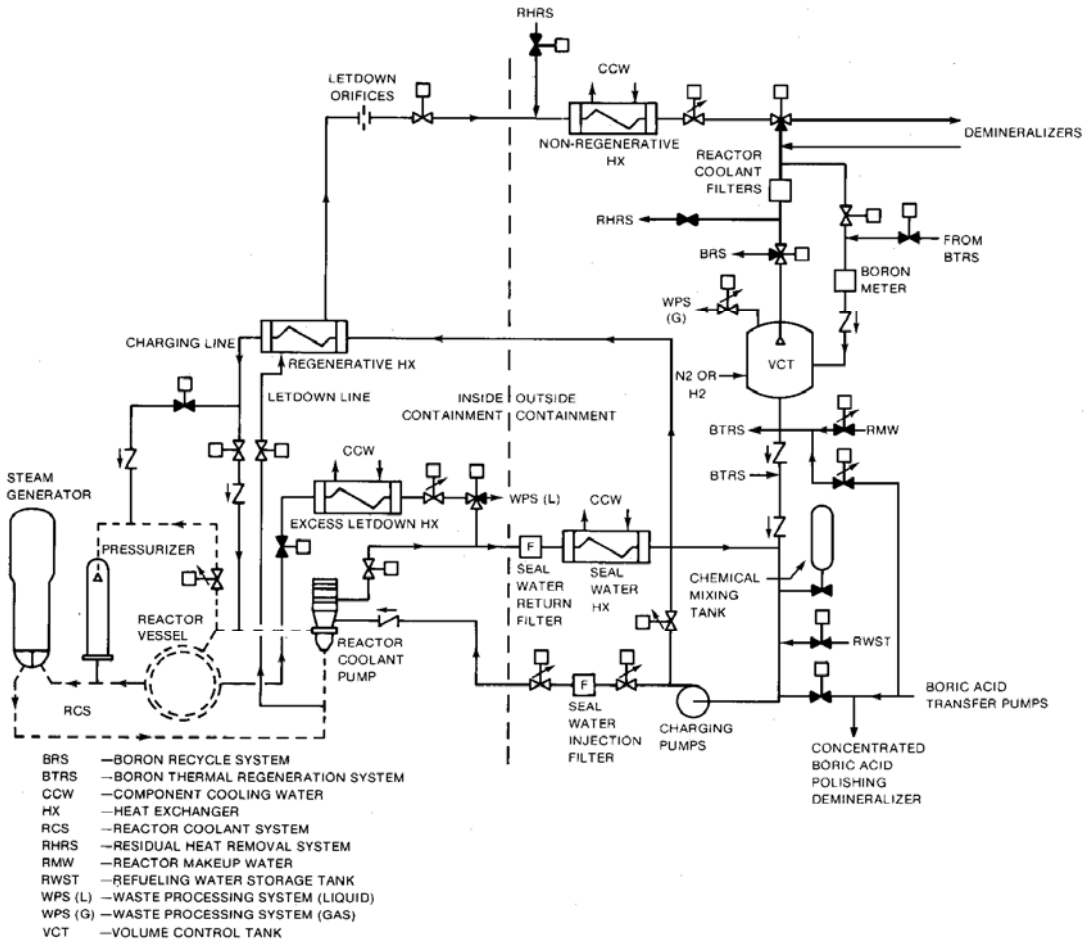


**Figure 5.9 Westinghouse Chemical and Volume Control System (CVCS) (Gosselin et al. 2002)**

#### 5.3.1.1 Normal Charging and Letdown Shutdown and Subsequent Return to Service

In this event, the charging and letdown flow is secured and subsequently returned to service while the plant is at normal operating pressure and temperature. Letdown flow is first secured, causing the charging nozzle temperature to decrease rapidly from 265°C (500°F) to 21.1°C (70°F). Once letdown is secured, charging flow is stopped and the charging nozzle temperature (i.e., RCS cold leg temperature) increases from 21.1°C (70°F) to 291.1°C (556°F). Upon the return to service, the charging flow is first established, causing the charging nozzle temperature to decrease rapidly from 291.1°C (556°F) to 21.1°C (70°F). Letdown flow is then restored, causing the charging nozzle temperature to increase from 21.1°C (70°F) to 265°C 500°F.

#### 5.3.1.2 Loss of Charging and Subsequent Return to Service

In this event, charging flow is lost and re-initiated during normal plant operation. This event is evaluated with and without letdown flow present. In either case, the charging nozzle is assumed to undergo step temperature changes between 21.1°C (70°F) and 293.3°C (560°F).

#### 5.3.1.3 Charging Flow Increase and Subsequent Decrease

Because letdown flow is fixed in the Westinghouse CVCS design, charging flow changes can result any time plant reactor power changes. In this case, the charging flow responds to the increase/decrease in pressurizer liquid level caused by the changes in reactor coolant average temperature. For design purposes, a 50% step change in charging flow is assumed for each load cycle. This results in rapid temperature changes of approximately 37.8°C (100°F) at the charging nozzle. Because the changes in charging flow will occur automatically during plant operation, thousands of cycles are typically assumed to occur over the life of the plant.

#### 5.3.1.4 Letdown Flow Increase and Subsequent Decrease

Unlike charging flow, letdown flow can be changed manually only by changing the letdown orifice configuration (adding or removing the number and size of the flow orifices on line). Because for every change in letdown flow there is a corresponding change in charging flow, temperature transients at the charging nozzle will result. For design purposes, letdown flow is typically assumed to change 60% due to the addition and subsequent removal of a second letdown flow orifice. This can result in rapid charging nozzle temperature changes of approximately 37.8°C (100°F)-51.7°C (125°F).

### 5.3.2 Design Transient Stresses and Cumulative Usage Factor

For this study, the design transient load pair combinations and alternating stresses used for a new vintage Westinghouse charging line nozzle in NUREG/CR-6260 also were assumed. The design transient, load pair combinations, alternating stresses ($S_{ALT}$ ), number of allowable cycles (N), number of assumed cycle occurrences (n), and corresponding fatigue usage (u) are shown in Table 5.1. In the Ware et al. study (1995), an effort was made to reduce conservatism in the licensees' calculations. Ware identified some 17 potential changes that could be used to reduce conservatism in his analysis. Several changes were found from review of the licensees' design stress reports. These mainly consisted of changes to the ASME Code since the edition of record for the plants' licensing bases and the anticipated numbers of cycles for some transients exceeding the number of design basis cycles. For the charging line nozzle, a list of the potential conservative assumptions and those removed in the Ware study is shown in Table 5.1 and is reflected in Table 5.2 (Ware et al. 1995; Simonen and Gosselin 2001).

**Table 5.1 Assessment of NUREG/CR-6260 Westinghouse Charging Nozzle Design Analysis Assumptions**

| Design Analysis Assumptions | Potential | Used | Comments |
|---|---|---|---|
| Correct CUF calculation | No | No | Analysis appear to be correct |
| Detailed load pairs | No | No | Detailed load pairs were used |
| Stress Concentration/ Fatigue Strength Reduction Factor | Yes | No | Insufficient information |
| $S_m$ value | Yes | Yes | Conservative $S_m$ used |
| Material property changes | No | No | No changes, Summer 1979 addenda used |
| Fatigue curve E value | No | No | Proper adjustment was made |
| Code analysis changes | No | No | No changes, Summer 1979 addenda used |
| Actual cycles | Yes | No | No data for numbers of actual cycles |
| High temperature rates | Yes | No | Actual rates probably less than design |
| Detailed stress modeling | Yes | No | NB-3600 analysis used |
| Conservative thermal parameters | Yes | No | Conservative heat transfer coefficients may have been used |
| Time phasing of stresses | Yes | No | Maximums of $\Delta T_1$, $\Delta T_2$, and $T_a$-$T_b$ terms may have been used |
| Number of Operating Basis Earthquakes (OBE) | No | No | Only 20 OBE cycles were assumed |
| CC N-411 damping | No | No | CC N-411 damping used |
| Number of hydro-tests | No | No | Hydrostatic pressure tests did not contribute to CUF |
| Fatigue monitoring | Yes | No | Actual transients probably less severe than design |
| Plastic analysis | Yes | No | Elastic plastic finite element analysis could be used |

Based on the loading conditions in Table 5.2, the CUF at 40 years (including reactor water effects) was estimated to be 3.978. In this case, the high fatigue usage is caused primarily by the large number of cycles associated with the loss of letdown and loss of charging flow transients. It is expected that for most PWRs, the actual cycles of these types of transients are less than the numbers assumed in these calculations. Assuming that the occurrence of these loading cycles is uniformly distributed over 40 operating years, the charging nozzle design limit (CUF = 1) would be reached during the tenth year of plant operation.

## 5.4 Probabilistic Fracture Mechanics Calculations

Probabilistic fracture mechanics sensitivity calculations were performed based on the design loadings in NUREG/CR-6260 for a 76.2-mm (3-in.) NPS Schedule 160 charging line nozzle in a Westinghouse PWR. The sensitivity calculations included an evaluation of the relative contributions to failure probabilities of preexisting fabrication flaws versus fatigue cracks initiated by service-related fatigue stresses. The inspection strategies, NDE performance (POD), and corresponding pc-PRAISE POD error function parameters ($a^*$, $\varepsilon$, and $\nu$) considered in this study are summarized in Table 5.3.

**Table 5.2 NUREG/CR-6260 New Vintage Westinghouse Charging Nozzle CUF Results**

| LOAD PAIR | $S_{ALT}$ | N | n | u |
|---|---|---|---|---|
| Loss of charging-prompt return/null | 133.44 | 66 | 120 | 1.818 |
| Loss of charging-delayed return/null | 132.78 | 66 | 12 | 0.182 |
| Normal charging and letdown shutdown/null | 101.06 | 182 | 60 | 0.330 |
| Loss of letdown-delayed return/null | 56.05 | 1673 | 8 | 0.005 |
| Reactor trip/OBE | 54.23 | 1993 | 20 | 0.010 |
| Loss of letdown-delayed return/flow increase | 47.47 | 4565 | 4 | 0.001 |
| Loss of charging-prompt return/flow increase | 46.47 | 355 | 120 | 0.022 |
| Step increase in charging/flow increase | 41.74 | 14611 | 14276 | 0.977 |
| Step increase in charging/flow decrease | 40.87 | 18864 | 124 | 0.007 |
| Letdown increase/flow decrease | 38.49 | 28848 | 1076 | 0.037 |
| Letdown increase/reactor trip | 37.35 | 33544 | 30 | 0.001 |
| Letdown increase/flow increase | 36.74 | 36555 | 13294 | 0.364 |
| Cooldown/flow increase | 35.48 | 44239 | 5 | 0.000 |
| Flow decrease/flow increase | 34.88 | 48763 | 1101 | 0.023 |
| Flow decrease/reactor trip | 34.13 | 55414 | 10 | 0.000 |
| Letdown increase/letdown decrease | 32.33 | 78577 | 89 | 0.001 |
| Letdown increase/flow decrease | 31.17 | 102284 | 14311 | 0.140 |
| Reactor trip/flow decrease | 30.33 | 126777 | 5 | 0.000 |
| | | | **CUF** | **3.918** |

## 5.5 Probability of Detection Curves

Prior to the POD studies presented in this report, UT performance models used for structural reliability evaluations in nuclear power plant piping had not changed substantially since the early 1980s. Since that time, the POD models employed by the NRC and much of the industry were based on work performed by Lawrence Livermore Laboratory (Harris et al. 1981). These models assumed that the POD was a function of flaw size (i.e., length, depth, area) and that the POD will be zero for very small cracks and will be 100% for very large cracks. UT performance was modeled by the following lognormal error-function (erfc) relationship and was incorporated into an early version of the pc-PRAISE computer code:

$$POD = 1 - P_{ND} = 1 - \frac{1}{2} \cdot \text{erfc}\left[ \nu \cdot \ln\left( \frac{A}{A^*} \right) \right]$$

where $P_{ND}$ = nondetection probability
$A$ = crack area
$\nu$ = slope of nondetection probability function at 50% $P_{ND}$
$A^*$ = crack area 50% $P_{ND}$.

**Table 5.3 Inservice Inspection Strategy Evaluation Cases**

| Case | Inspection Strategy | POD | a, in. | ε | ν |
|---|---|---|---|---|---|
| BASE | No volumetric ISI | NA | NA | NA | NA |
| 1A | ISI every 10 years for 60 years | A | 0.0359 | 0.005 | 1.600 |
| 1B | ISI every 10 years for 60 years | VG | 0.1077 | 0.020 | 1.600 |
| 1C | ISI every 10 years for 60 years | M | 0.2872 | 0.100 | 1.600 |
| 1P | ISI every 10 years for 60 years | SST2 | PDI SS 0.4 < t < 0.15 | | |
| 2A | ISI at 2-year frequency starting at year 10 | A | 0.0359 | 0.005 | 1.600 |
| 2B | ISI at 2-year frequency starting at year 10 | VG | 0.1077 | 0.020 | 1.600 |
| 2C | ISI at 2-year frequency starting at year 10 | N | 0.2872 | 0.100 | 1.600 |
| 2P | ISI at 2-year frequency starting at year 10 | SST2 | PDI SS 0.4 < t < 0.15 | | |
| 4A | ISI at 4-year frequency starting at year 10 | A | 0.0359 | 0.005 | 1.600 |
| 4B | ISI at 4-year frequency starting at year 10 | VG | 0.1077 | 0.020 | 1.600 |
| 4C | ISI at 4-year frequency starting at year 10 | N | 0.2872 | 0.100 | 1.600 |
| 4P | ISI at 4-year frequency starting at year 10 | SST2 | PDI SS 0.4 < t < 0.15 | | |
| 6A | ISI at 6-year frequency starting at year 10 | A | 0.0359 | 0.005 | 1.600 |
| 6B | ISI at 6-year frequency starting at year 10 | VG | 0.1077 | 0.020 | 1.600 |
| 6C | ISI at 6-year frequency starting at year 10 | M | 0.2872 | 0.100 | 1.600 |
| 6P | ISI at 6-year frequency starting at year 10 | SST2 | PDI SS 0.4 < t < 0.15 | | |
| A = Advanced POD; VG = Very Good POD; M = Marginal POD; P = PDI Performance POD. 25.4 mm = 1 in. | | | | | |

Additional work in 1992 (Harris and Dedhia 1992) recognized that UT can fail to detect very large flaws and that the POD curve asymptotically approaches a probability that is greater than zero (i.e., a POD < 1). As such, the POD erfc relationship in pc-PRAISE was changed to the following present-day form:

$$POD = 1 - P_{ND} = 1 - \left\{ \varepsilon + \frac{1}{2}(1-\varepsilon) \cdot \mathrm{erfc}\left[ \nu \cdot \ln\left( \frac{A}{A^*} \right) \right] \right\}$$

where $\varepsilon$ = smallest possible $P_{ND}$ for very large cracks.

In previous PNNL studies (Khaleel et al. 1999) that examined the effects of alternative inspection strategies on nuclear power plant piping systems, parameters for the pc-PRAISE POD model were estimated. When used with the pc-PRAISE erfc model, these parameters were intended to bound POD performance levels for inspection teams in the field. The parameters were arrived at through an informal expert judgment elicitation process using PNNL staff members with specialized knowledge of UT

performance data from previous round-robin studies and from early industry performance demonstration efforts. In estimating the POD curves, it was recognized that industry performance demonstration testing required inspection teams to detect large flaws with a relatively high level of reliability. However, this high level of detection reliability requirement was relaxed for relatively small flaws.

Three NDE performance levels were considered:

*Advanced Performance Level* – This POD performance curve corresponds to an inspection team whose performance is significantly better than expected for teams that have passed the Appendix VIII qualification test. Such teams would need to apply advanced NDE technologies and/or procedures that are not currently available to inspectors in the field.

*Very Good Performance Level* – At this POD performance level, inspection teams are expected to perform at a level that exceeds the minimum level necessary to pass the Appendix VIII qualification test.

*Marginal Performance Level* – At this POD performance level, an inspection team is expected to have only a small chance of satisfying the performance demonstration requirements of Appendix VIII. This performance level would not be representative of current-day standards for wrought stainless steel; however, it may be representative of current-day UT performance of cast stainless steels.

The resulting wrought stainless steel pc-PRAISE POD parameters for each performance level are show in Table 5.3. The above pc-PRAISE POD performance curves are compared to the PDI performance based POD curve in Figures 5.10, 5.11, and 5.12. We can see that for long shallow cracks, the advanced performance level POD in pc-PRAISE would predict a better performance compared to the PDI data. This is consistent with expectations because the advanced POD curve would correspond to the performance expected from very knowledgeable examiners using state-of-the-art equipment under ideal (laboratory) conditions. However, for short cracks that are less then 25% through-wall depth, the PDI performance results are significantly better than estimated for the advanced performance level.

When compared to the very good performance level POD curve, the PDI performance for small cracks was significantly better than what had been expected for through-wall crack depths below 25% at length-to-depth ratios greater than 10. The conservatism associated with the very good pc-PRAISE performance model is even more pronounced for a flaw length-to-depth ratio of two. However, the PDI performance (although still good) falls short of that expected for larger flaws.

### 5.5.1 Preexisting Flaws

An implied assumption in the current calculations is that component failures are due primarily to fatigue cracks that initiate after the components enter service and that failures caused by preexisting fabrication flaws make only small contributions to the failure probabilities. Sensitivity calculations were performed to determine if it is reasonable to neglect the fabrication flaws. The method used to estimate the number and sizes of fabrications flaws is described here.

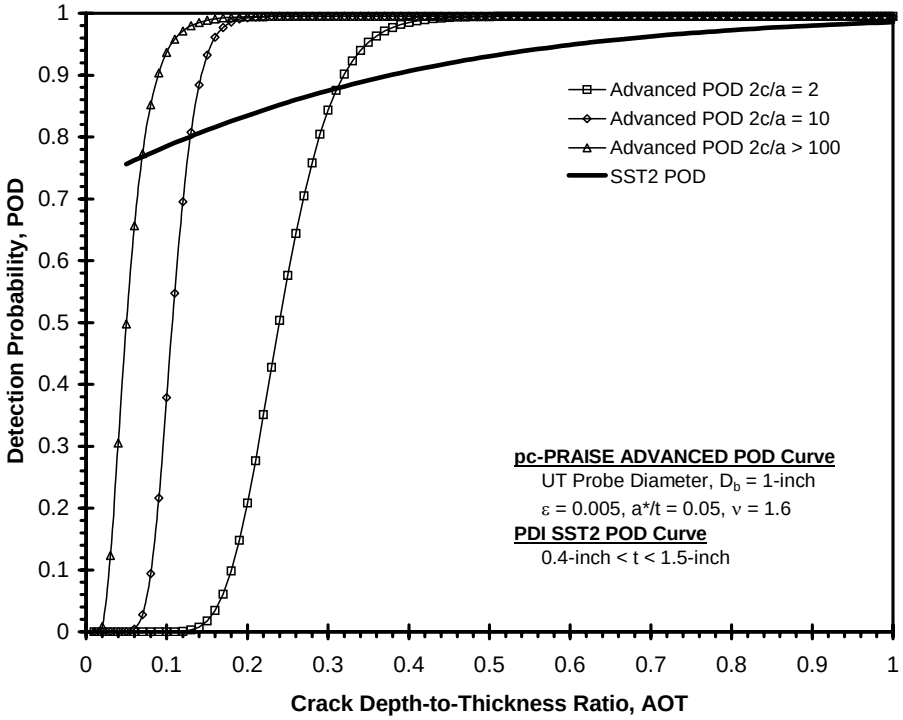


**Figure 5.10 pc-PRAISE Advanced POD and PDI SST2 POD Comparison (25.4 mm = 1 in.)**

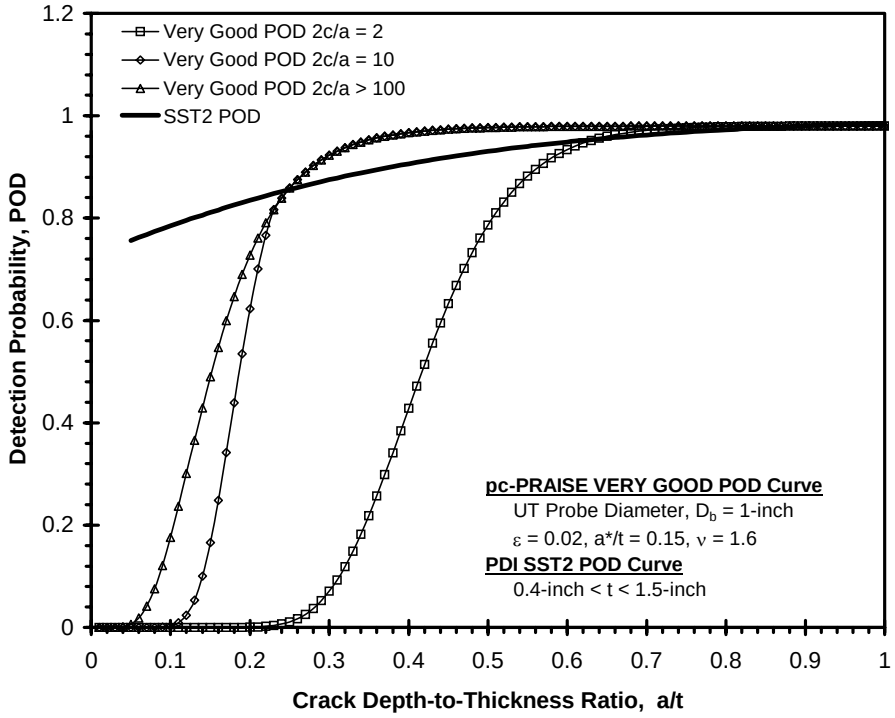


**Figure 5.11 pc-PRAISE Very Good POD and PDI SST2 POD Comparison (25.4 mm = 1 in.)**

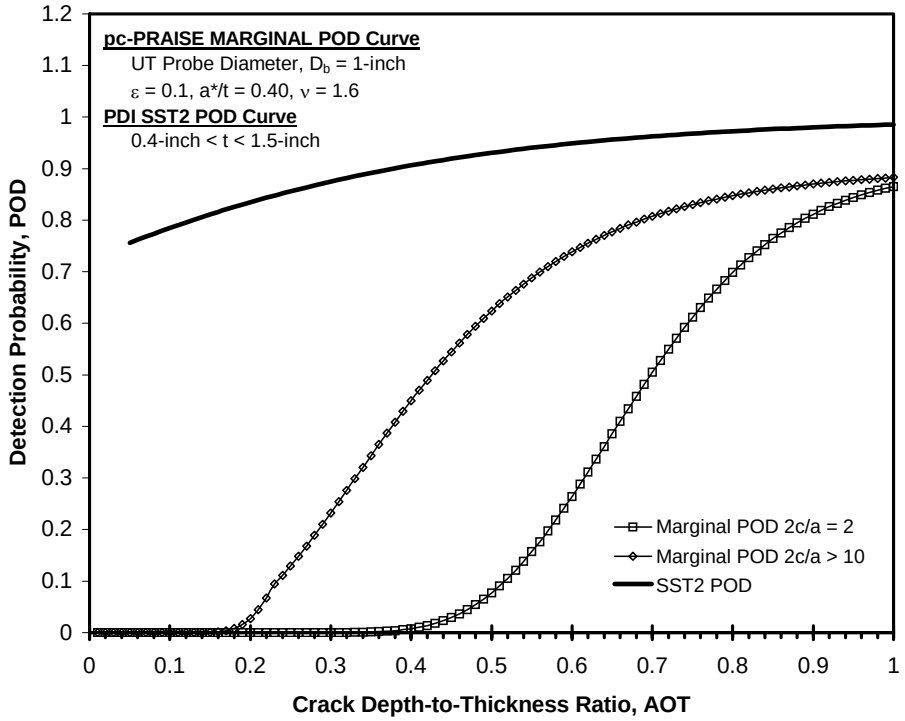


**Figure 5.12 pc-PRAISE Marginal POD and PDI SST2 POD Comparison (25.4 mm = 1 in.)**

The estimation methodology is described by Khaleel et al. (1999). These publications describe applications of the PRODIGAL code to a range of piping welds and the statistical correlations used to generate predictive equations that apply to welds of stainless steel and ferritic steels, wall thickness ranging from 6.35 mm (0.25 in.) to 63.5 mm (2.5 in.), manual metal arc and tungsten inert gas welding, and welds that are inspected or not inspected during construction by radiographic methods.

The particular weld addressed by the current work is as follows:

- material type = stainless steel
- inner diameter = 66.5 mm (2.62 in.)
- wall thickness = 11.1 mm (0.437 in.)
- welding rocess = tungsten inert gas
- inspection = radiographic testing.

The distribution of flaw depths is described by a lognormal distribution with the following parameters:

- median flaw depth = 2.51 mm (0.099 in.)
- shape parameter = standard deviation of *ln* (flaw depth, in.) = 0.2331
- number of flaws per weld = 0.0282.

A flaw density of 0.0282 flaws per weld means that only one weld in 35 will have a preexisting flaw at the inner surface of the pipe. The pc-PRAISE code for preexisting flaws predicts that a weld without a flaw will never fail in fatigue, which means that the corresponding failure probability can never exceed 0.0282. In contrast, the calculated failure probability for the case of initiated fatigue cracks can become 100%—but only if the number and severity of the cyclic stresses are sufficiently large.

### 5.5.2 Baseline Failure Probabilities

Because the nominal pipe size of the charging nozzle in this study is less than 101.6 mm (4 in.), volumetric inspections are not required by the ASME Code Section XI, and only outside surface examinations (i.e., dye penetrant tests) are performed every 10 years. Because thermal fatigue is the dominant degradation mechanism for this component, crack initiation is expected to occur at the inside surface/counterbore of the weld. Obviously, outside surface examinations cannot detect internal cracking; therefore, the baseline failure probability calculations assumed that no volumetric inspections would be performed on the charging nozzle.

The relative contributions to the charging nozzle baseline failure probabilities for preexisting fabrication flaws versus fatigue cracks initiated by service stresses are shown in Figure 5.13 (Simonen and Gosselin 2001). For this component, the presence of preexisting fabrication flaws dominated failure probability very early in plant life (within the first 5 years of operation). By the $10^{th}$ year of operation, the contribution to failure probability from fabrication defects is insignificant, and component failures are due primarily to fatigue cracks that initiate after the components enter service. This suggests that it would be reasonable to neglect the fabrication flaws.

## 5.6 Failure Probabilities with Inservice Inspection

Sensitivity calculations were performed to examine how different inservice inspection strategies affect charging nozzle reliability. Several inspection strategies and POD cases were considered. Each case is described in Table 5.3. Figures 5.14 through 5.19 show predicted cumulative leak (through-wall crack) probabilities/leak frequencies as a function of plant operating time (0-60 years) for “advanced,” “very good,” and “marginal” POD curves. In Figures 5.20 and 5.21, the baseline leak frequency is compared with 10-year, 8-year, and 6-year augmented inspection frequencies assuming a POD based on performance demonstration data (Table 5.3 Cases 6P, 7P, and 8P).

For the baseline case, the cumulative leak probability at 10 years (when the calculated CUF becomes 1.0) is approximately $1.0 \times 10^{-1}$ or 1 chance in 10 that the weld will fail. Under continued operation between 10 and 35 years, when no volumetric inspections are performed, the leak probability continues to increase at an increasing rate. After year 35, the baseline failure probability increases at a decreasing rate. When the calculated CUF = 1.0, the design failure frequency is approximately $3.2 \times 10^{-2}$ per year. The effectiveness of inspection programs implemented after year 10 could therefore be evaluated on their ability to maintain failure frequencies below this design threshold value.

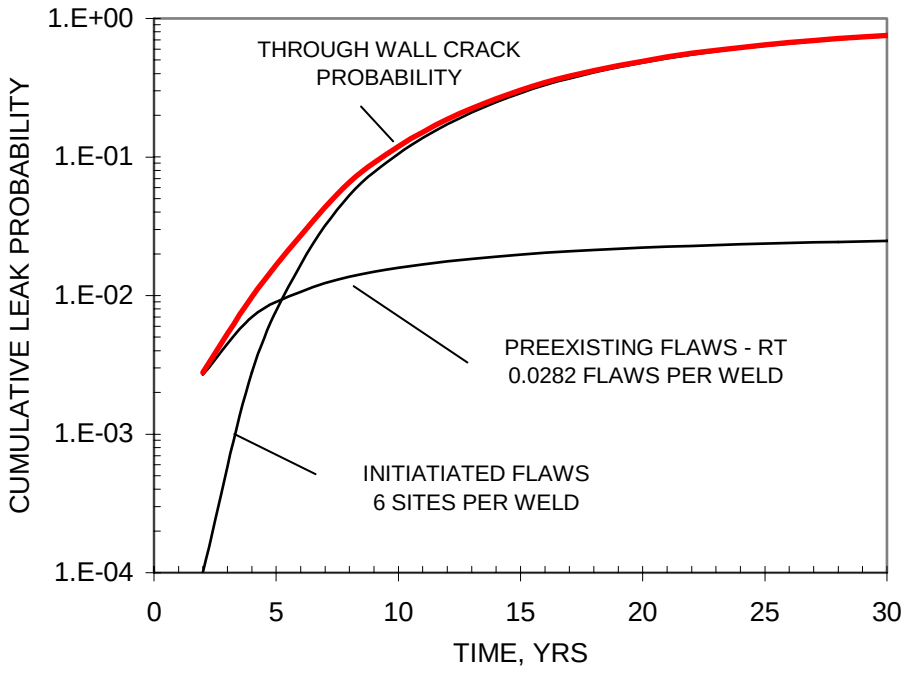


**Figure 5.13 Cumulative Leak Probability Versus Time (Simonen and Gosselin 2001)**

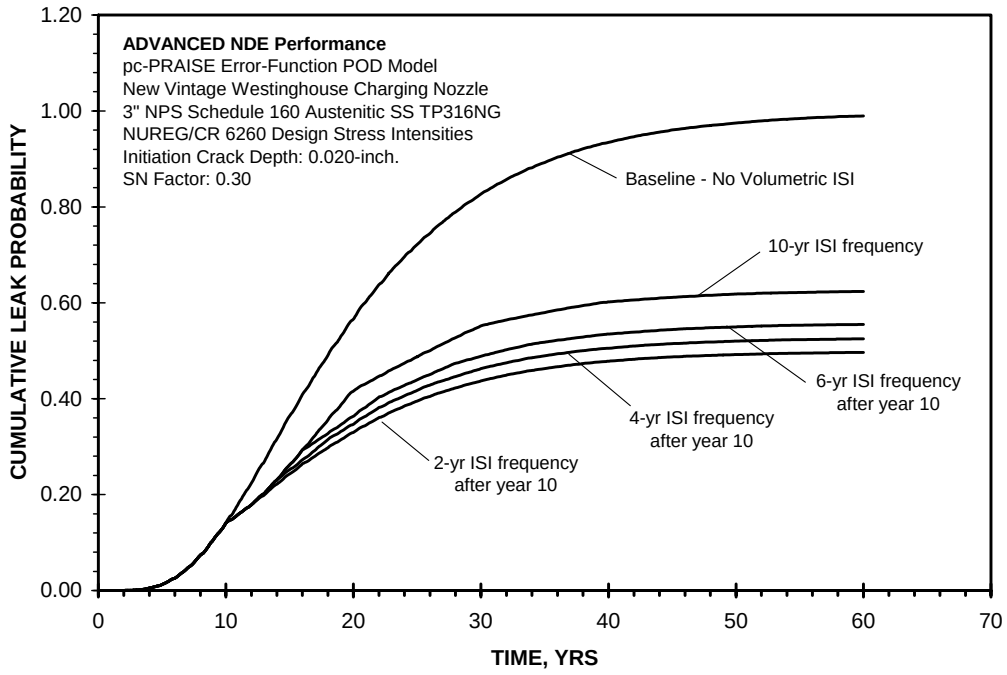


**Figure 5.14 Inspection Strategy Leak Probability Comparisons for Advanced POD (25.4 mm = 1 in.)**

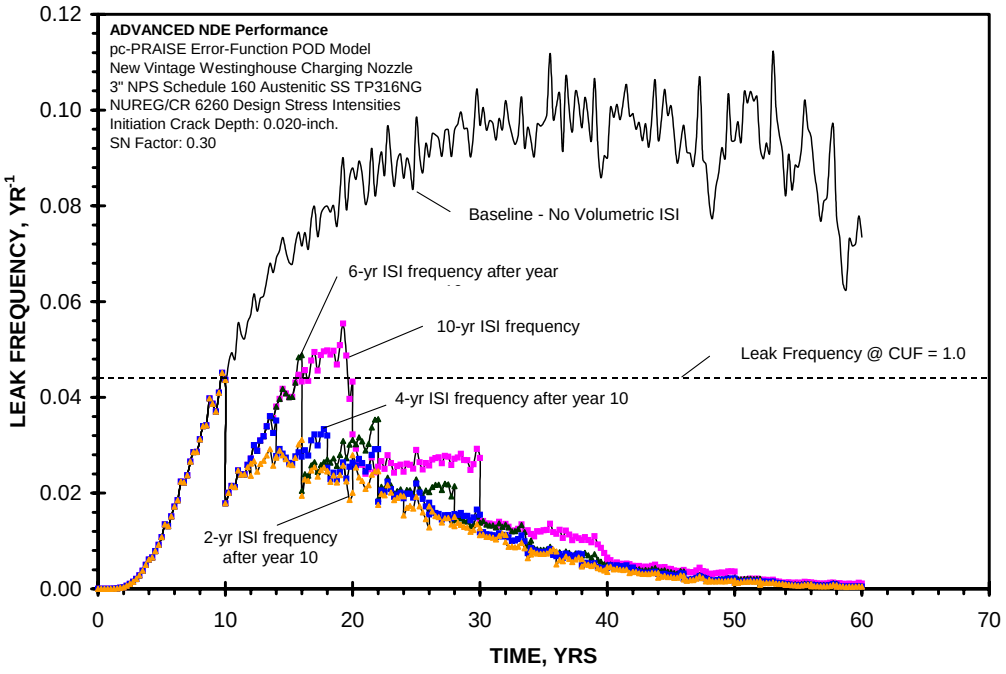


**Figure 5.15 Inspection Strategy Leak Frequency Comparisons for Advanced POD (25.4 mm = 1 in.)**

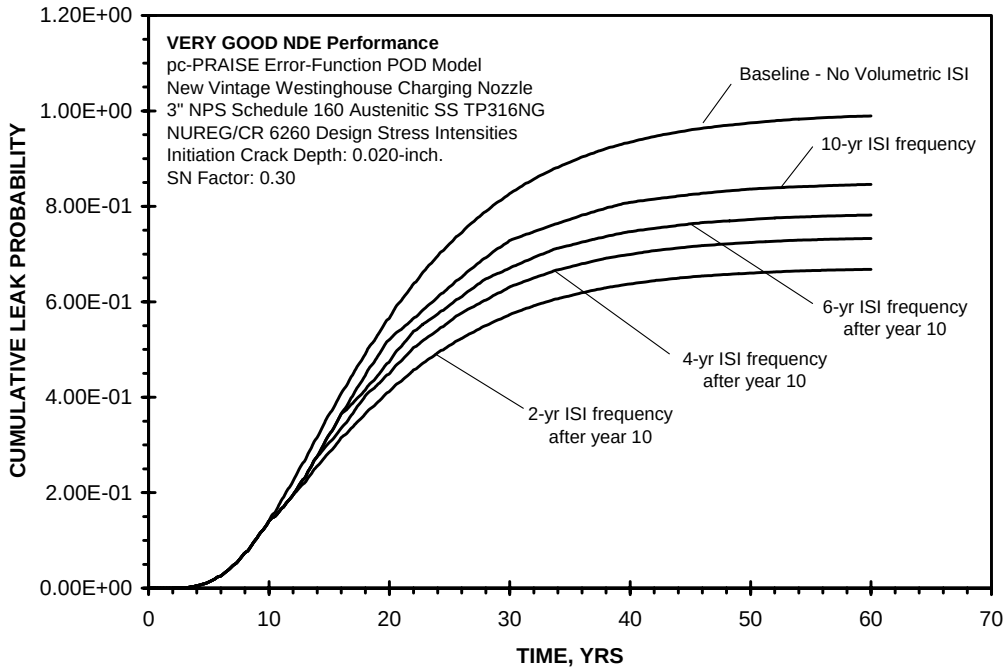


**Figure 5.16 Inspection Strategy Leak Probability Comparisons for Very Good POD (25.4 mm = 1 in.)**

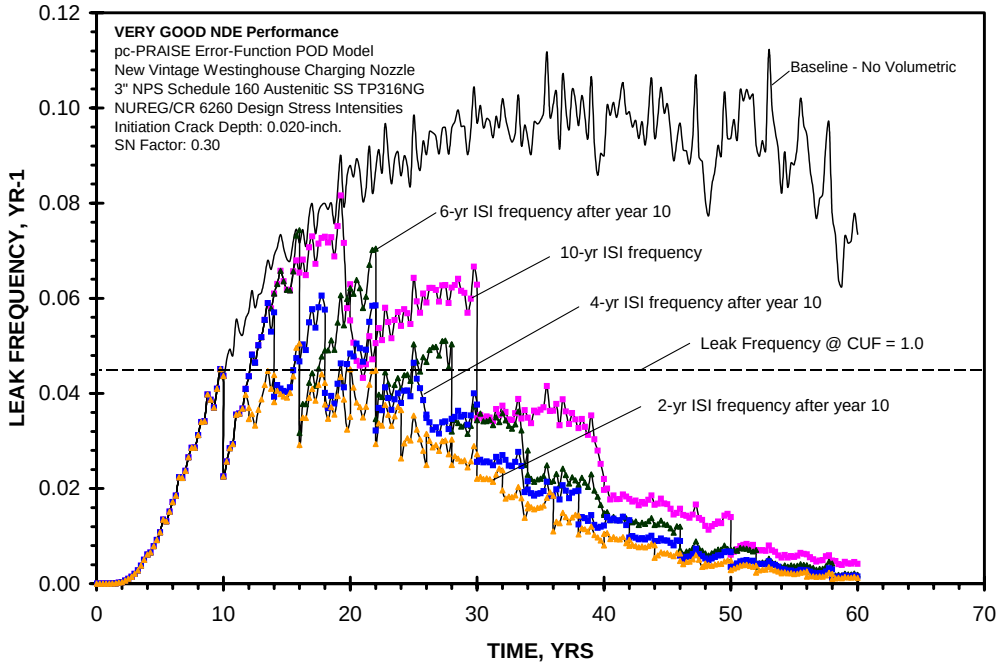


**Figure 5.17 Inspection Strategy Leak Frequency Comparisons for Very Good POD (25.4 mm = 1 in.)**

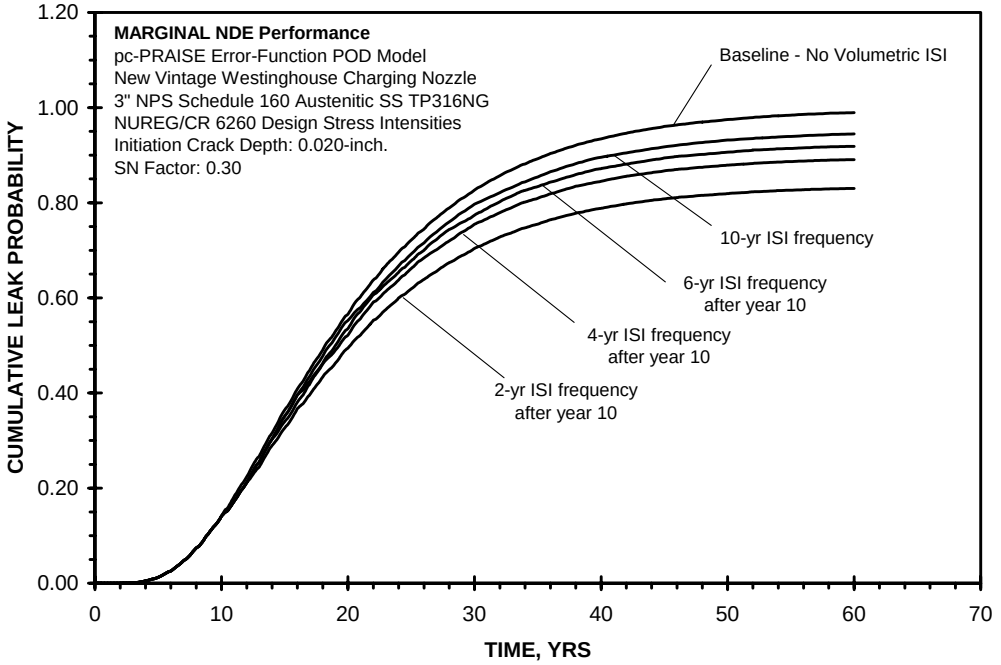


**Figure 5.18 Inspection Strategy Leak Probability Comparisons for Marginal POD (25.4 mm = 1 in.)**

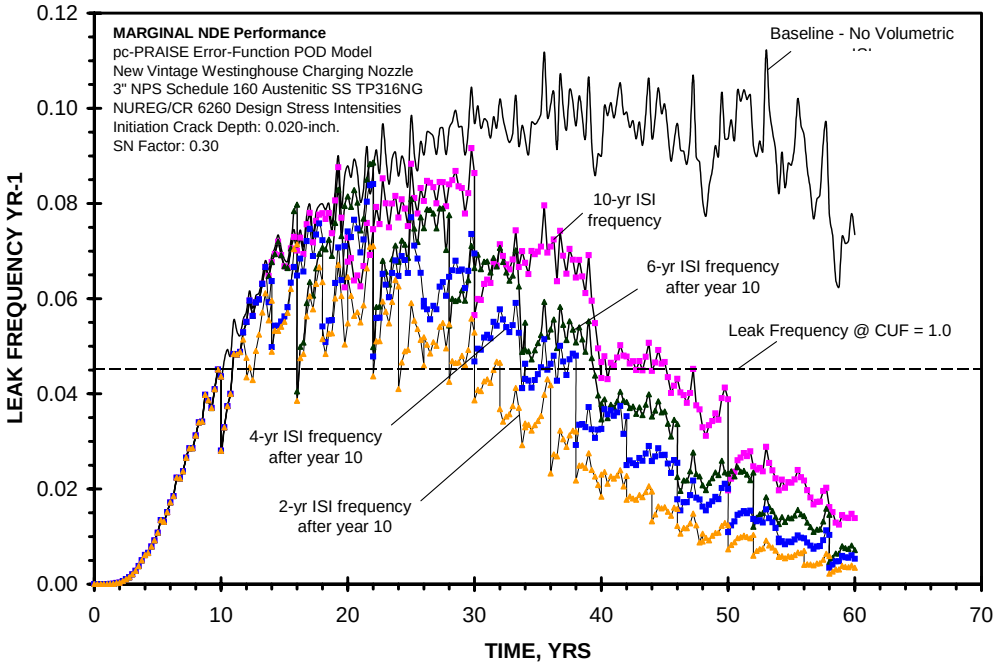


**Figure 5.19 Inspection Strategy Leak Frequency Comparisons for Marginal POD (25.4 mm = 1 in.)**

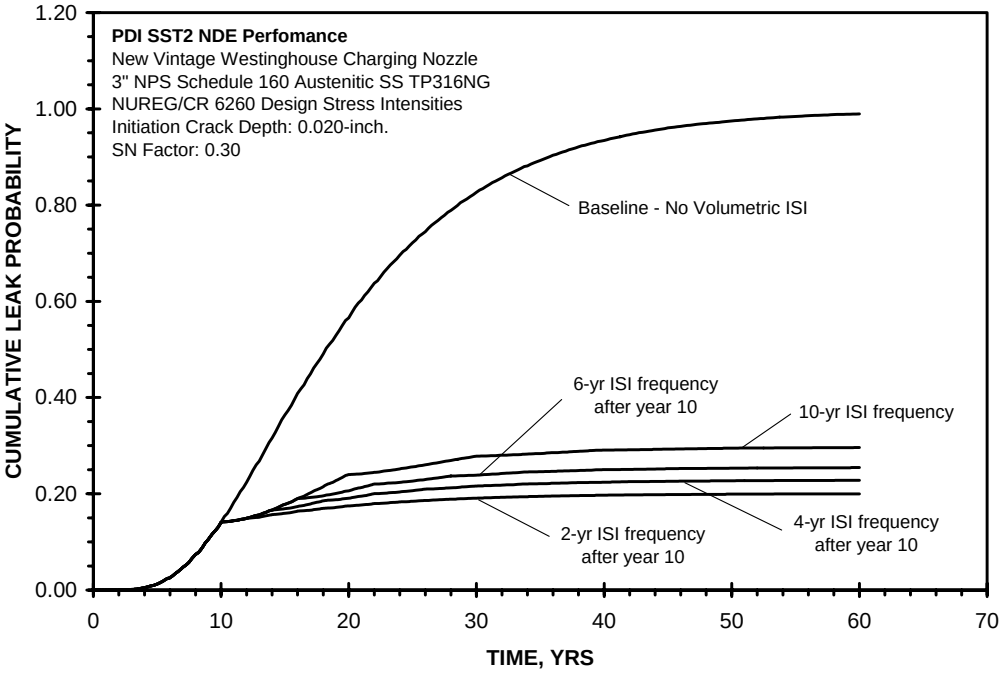


**Figure 5.20 Inspection Strategy Leak Probability Comparison for Performance-Based POD (25.4 mm = 1 in.)**

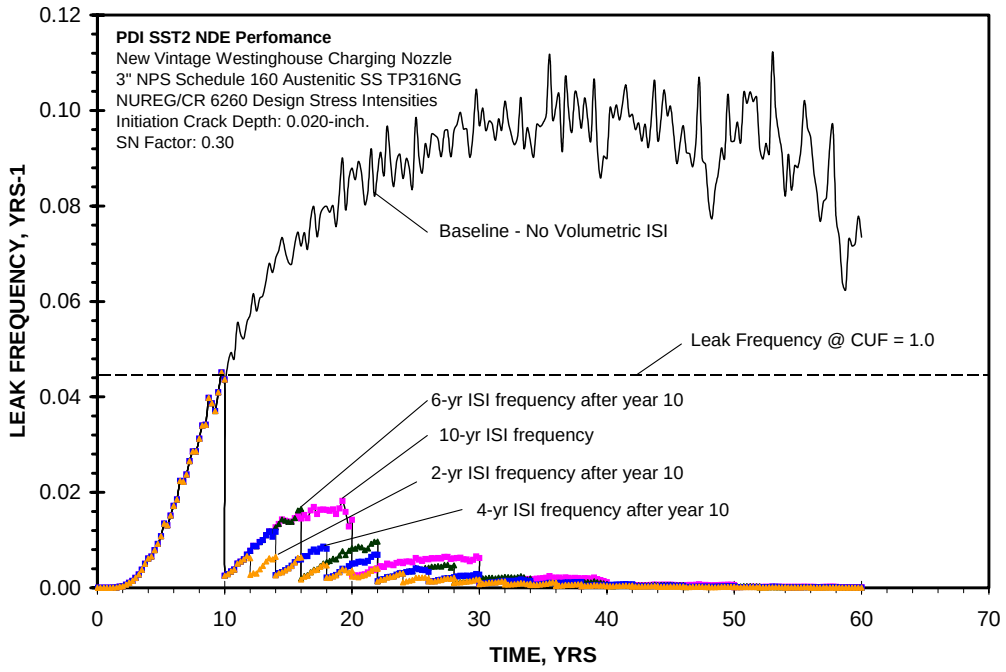


**Figure 5.21 Inspection Strategy Leak Frequency Comparison for Performance-Based POD (25.4 mm = 1 in.)**

Under the loading conditions imposed in this study, performing a volumetric examination once every 10 years will not ensure that the charging nozzle failure probability remains below the design threshold value. For "advanced" NDE performance, significant reductions can be attained with the more aggressive 2-year and 4-year inspection frequencies. For the "very good" NDE performance, normal 10-year inspection frequency will not reduce failure frequency until operating year 30. In this case, a 2-year inspection frequency would be necessary to remain below the design threshold frequency. When a "marginal" NDE performance is assumed, the various inspection strategies have a very small impact on component reliability out to 40-years of operation. When a PDI performance-based POD curve is assumed, all inspection strategies show a significant reduction in component failure frequency after the first inspection at operating year 10. This is due primarily to the improved ability to detect small cracks and repair small cracks early in plant life.

## 5.7 Concluding Remarks

Recent work at PNNL and EPRI has shown that for all ferritic material components and for wrought stainless steel components with configurations that allow inspection from the same side of the weld of the postulated defect, the ability to detect fatigue cracks (TWC depths 10-25%) is much better than originally assumed in Appendix L. Because smaller defects can be detected and repaired earlier in plant life, significant improvements in component reliabilities result from the performance of periodic inspections. Very good NDE performance can be expected at flaw depths consistent with allowable flaw depths specified in ASME Section XI Tables IWB-3514-1 and 3514-2. Therefore, the hypothetical flaw depths currently specified in ASME Section XI Appendix L can be reduced to the depths specified in Tables IWB-3514-1 and 3514-2.

# 6 Effect of Aspect Ratio on Growth of Cracks

The classical approach for evaluating the acceptability of a flaw in a component is reflected in Article A-1000, ASME Section XI Appendix A. The following steps are included:

- Determine the actual flaw configuration from inspection results.
- Characterize the flaw and resolve it into a shape that can be analyzed.
- Determine the stresses at the location for all normal/upset and emergency/faulted conditions.
- Establish material resistance to fracture (fracture toughness).
- Determine the allowable end-of-life or end-of-evaluation period flaw size, with consideration of all normal/upset and emergency/faulted conditions.
- Perform crack growth analysis to ensure that the flaw will remain at a size less than the allowable flaw size.

In the 1992 Edition of Section XI Appendix A, the Code was silent on the effect of aspect ratio in performing a crack growth analysis. In the 1993 Addenda, Article A-5000 was revised to specifically include an update of both the surface depth (a) and the surface length (l) when evaluating crack growth. The latter would require that crack growth analysis be conducted using a variable aspect ratio. This considerably complicates the analysis for crack growth.

In this section, deterministic crack growth analysis is conducted to aid in understanding the effects of various loading types on the natural growth of cracks, considering both the depth and surface length growth.

## 6.1 Crack Growth Model

For this analysis, the fracture mechanics model is taken from ASME Section XI Appendix A (1995 Edition with 1997 Addenda). Although this model is for ferritic vessels, it incorporates the ability to consider both the deepest point and surface point stress intensity factors. In addition, it includes the capability to assess the effect of varying stress profiles through the wall because the stress intensity factor formulations assume the stress profile to be the sum of a series of polynomials with maximum order of three.

Section XI Appendix A has equations that may be used to predict both the surface and deepest point stress intensity factors. For the deepest point, the “G” coefficients are provided for a flaw aspect ratio (a/l) from 0 to 0.5 and for a crack depth ratio (a/t) from 0 to 0.8. For the surface point, the ranges are the same, except the lower range for the aspect ratio is 0.1. To allow for very small aspect ratios where the a/l might be less than 0.1, the relationships for the surface coefficients were extrapolated such that the

values at a/l = 0 would go to zero at a/t = 0. A typical example of a plot for the extrapolation for the $G_0$ term is shown in Figure 6.1. Note that the accuracy of this extrapolation does not have a significant effect on the results because aspect ratios were generally greater than 0.1 for most cases.

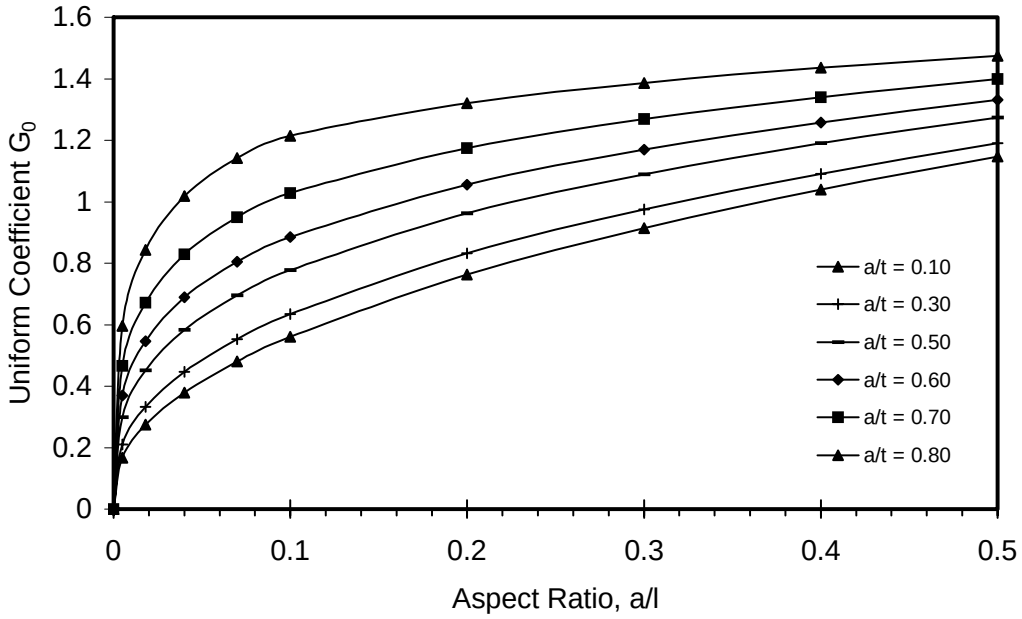


**Figure 6.1 Typical Extrapolation of Surface Crack Coefficients**

The basic equations in Section XI Appendix A show that the stress coefficients should be based on a curve fit of the stress distribution S(x) from the surface to the crack tip:

$$S(x) = C_0 + C_1 (x/a) + C_2 (x/a)^2 + C_3 (x/a)^3$$

where $\#C_n$ = $n^{th}$ constant for the stress curve fit polynomial expression
x = distance from the surface
a = crack depth.

For a well-behaved stress distribution throughout the entire wall thickness, a curve fit of the following form may be derived:

$$S(x) = B_0 + B_1 (x/t) + B_2 (x/t)^2 + B_3 (x/t)^3$$

where $\#B_n$ = $n^{th}$ constant for the alternate stress curve fit polynomial expression
t = component wall thickness.

This may be written also as

$$S = B_0 + B_1 (a/t) (x/a) + B_2 (a/t)^2 (x/a)^2 + B_3 (a/t)^3 (x/a)^3$$

Thus, it may be observed that the C coefficients required by the Section XI Appendix A equations can be directly related to the B coefficients for the polynomial through-wall stress distribution. This approach was used for this evaluation, such that a set of coefficients could be defined for a through-wall distribution.

For material crack growth properties, the curves as defined in Section XI Appendix A were used for ferritic materials for crack growth in water. Because no water environment curves are listed in Appendix C of the Code for austenitic materials, multipliers of 2 (for PWR environment) and 10 (for BWR environment) were applied to the air curves, as recommended in the ASME Appendix C basis document (EPRI 1986).

The effect of a crack growth threshold also was considered, using a lower bound for both austenitic and ferritic materials (Barson and Rolfe 1987).

$$\Delta K_{thres} = 6.4 \times (1 - 0.85 \times R) \text{ but not greater than } 6.05 \ \text{MPA}\sqrt{\text{m}} \ (5.5 \ \text{ksi}\sqrt{\text{inch}})$$

where $R = K_{min}/K_{max}$

$K_{min}$ = minimum stress intensity factor for load set pair, $\text{MPa}\sqrt{\text{m}}$ ($\text{ksi}\sqrt{\text{inch}}$)

$K_{max}$ = maximum stress intensity factor for load set pair, $\text{MPa}\sqrt{\text{m}}$ ($\text{ksi}\sqrt{\text{inch}}$).

## 6.2 Typical Component and Through-Wall Stress Profiles

The analysis was conducted for both 12.7 mm (0.5 in.) and 25.4 mm (1.0 in.) thick carbon steel and austenitic stainless steel piping. Several applied stress distributions were evaluated. The stress distributions and maximum stress magnitudes were chosen with consideration of typical Code-allowable stresses for various classifications of stresses.

A membrane stress, uniformly distributed across the wall was assumed to be 186 MPa (27 ksi). This is on the order of 1.5 $S_m$ (where $S_m$ is the basic allowable stress intensity for Class 1 components), representative of the allowable combination of primary pressure and bending tensile stress in the wall for a piping system. Addition of thermal bending stresses in the piping system could result in higher membrane stresses.

A bending stress ($S_{bend}$), linear between a positive (tensile) inside surface stress to negative (compressive) on the outside surface, was taken as 372 MPa (54 ksi). This is on the order of 3 $S_m$:

$$S_{bend} = 54 - 108 (x/t)$$

Thermal transients ($S_{ramp}$) result in nonlinear through-wall transients. In a study by PNNL, a generic thermal stress transient was developed (Khaleel et al. 2000). This stress distribution is representative of a thermal ramp transient.

$$S_{ramp} = 54 \times (1.0 - 3\,(x/t) + 1.5\,(x/t)^2)$$
$$= 54 - 162(x/t) + 81\,(x/t)^2$$

An alternative, more severe, stress gradient representative of a thermal shock transient ($S_{shock}$) was developed for this evaluation, based on evaluating a sudden injection of cold water into a safety injection nozzle:

$$S_{shock} = 81 \times (1.0 - 4.691(x/t) + 5.802(x/t)^2 - 2.357(x/t)^3)$$
$$= 81 - 380\,(x/t) + 470(x/t)^2 - 191\,(x/t)^3$$

The stress level for the thermal ramp transient was arbitrarily chosen to be on the order of $3S_m$. The thermal shock stress, exhibiting more of a peak stress, was taken to be about 60% larger than the thermal ramp transient.

A typical case was chosen as a combination of the thermal shock transient plus an additional 138-MPa (20-ksi) membrane stress. For all cases, the evaluation was conducted assuming cycling between the specific stress case and a zero-stress state. Figure 6.2 compares the five separate cases.

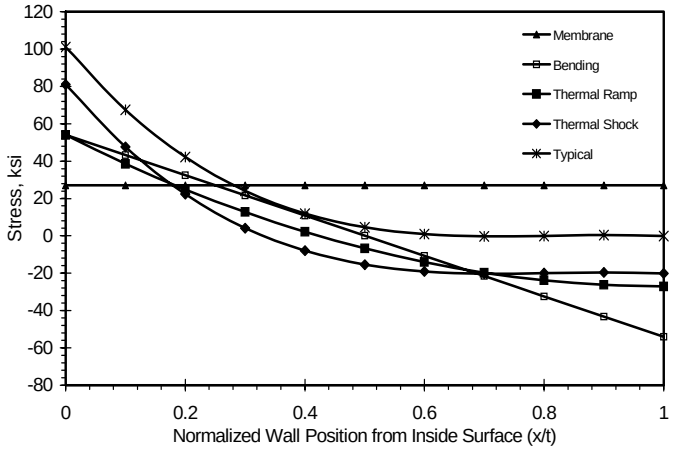


**Figure 6.2 Comparison of Stress Distribution for Loading Types Evaluated**

The effect of weld residual stresses ($S_{rs}$) also was considered, where two separate cases were evaluated. The one believed to be most realistic for welded piping with residual stresses along a circumferential crack is a through-wall distribution with zero average stress in the axial direction. This stress distribution is taken from NUREG-0313, Rev. 2 (Hazelton 1986), where a fourth-order polynomial is provided for the stress (ksi):

$$S_{rs} = 30 \times (1.0 - 6.91\,(x/t) + 8.687\,(x/t)^2 - 0.48\,(x/t)^3 - 2.027\,(x/t)^4)$$
$$= 30 - 207.3\,(x/t) + 260.61\,(x/t)^2 - 14.4\,(x/t)^3 - 60.81\,(x/t)^4$$

For use with Section XI Appendix A, which has only a third-order polynomial stress distribution, the following has been derived:

$$S_{rs} = 30 \times (1.0 - 7.196\,(x/t) + 10.342\,(x/t)^2 - 3.723\,(x/t)^3)$$
$$= 30 - 215.9\,(x/t) + 310.3\,(x/t)^2 - 111.7\,(x/t)^3$$

These are compared in Figure 6.3 and show excellent agreement up to a/t = 0.8. For the evaluation of residual stress effects, this is included with both cases of a load set pair in determining the range of stress intensity factor (e.g., with both the membrane stress case and with the zero load case). This produces the effect of a varying R-ratio through the wall for crack growth evaluation.

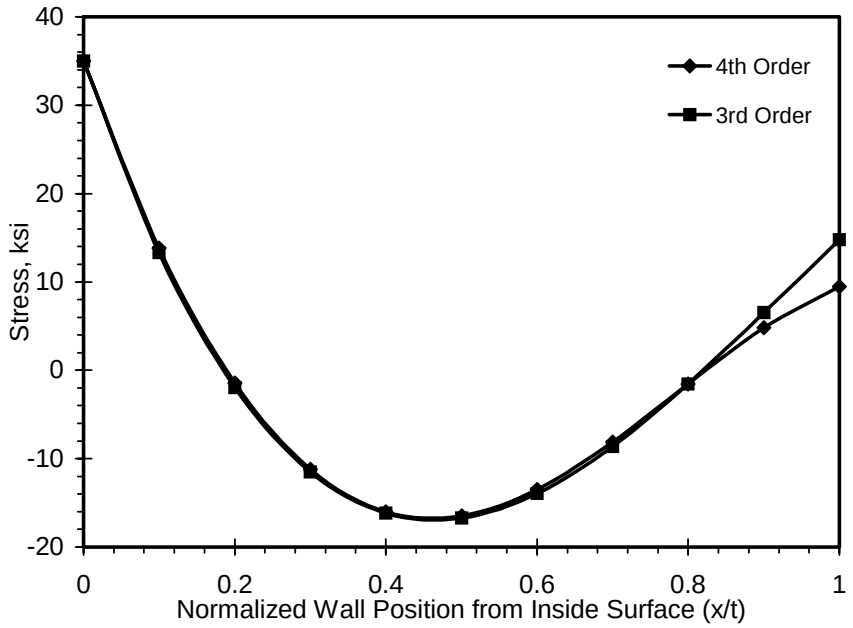


**Figure 6.3 Residual Stress Distribution (1 ksi = 6.897 MPa)**

For a case to evaluate an arbitrary effect of high R-ratio, it has been assumed that an arbitrary stress of 2069 MPa (300 ksi) membrane stress is added to both cases of the load set pair. Although there is no effect on the stress intensity factor range, this forces the consideration of a very high R-ratio for fatigue crack growth throughout the wall thickness.

## 6.3 Natural Crack Trajectories for Various Loads/Combinations

For all evaluations, crack growth was calculated using a model that grew the flaw in both the depth and length directions. Starting out with an initial assumed flaw size, the aspect ratio could then be tracked as a function of flaw depth for continued application of the load/zero-load cycling. This functional relationship is referred to as the natural aspect ratio trajectory because the aspect ratio changes during the process of crack growth through the wall.

For all cases, an initial flaw depth of 3 mm (0.118 in.) was chosen. This was consistent with work reported in NUREG/CR-6674 (Khaleel et al. 2000) that justified this as being an "engineering-size" crack.

The first case considers a 25.4-mm (1-in.)-thick carbon steel pipe with no residual stresses. The initial aspect ratio was taken as a/l = 0.5, a small circular crack with depth of 3 mm (0.118 in.) and surface length of 6.35 mm (0.25 in.). The results are shown in Figure 6.4. The following observations are made:

- For all loading types, the crack aspect ratio tends to decrease as the crack grows through the wall, showing that there is more rapid surface growth than depth growth.

- For the bending, ramp, and thermal shock loads, all of which have a zero stress average through the wall, the aspect ratio decreases faster for the steeper stress gradients.

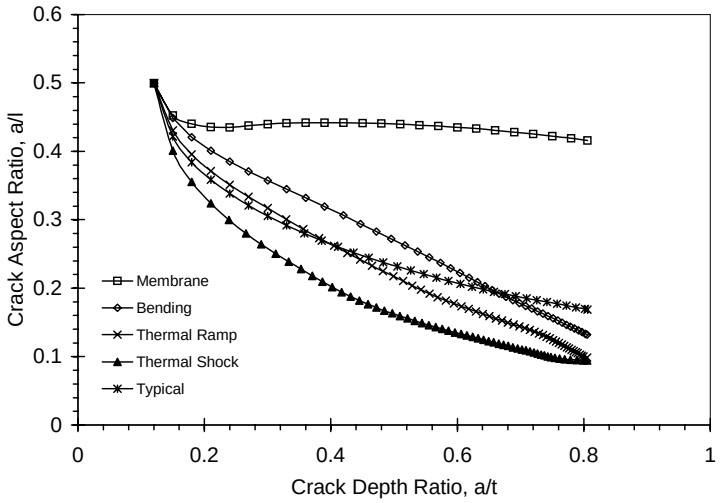


**Figure 6.4 Crack Growth Trajectories for 25.4 mm (1-in.) Thick Carbon Steel with No Residual Stresses, Initial a/l = 0.5**

- For the “typical” load, with contributions due to both membrane stress and a through-wall gradient, the aspect ratio tends to decrease rapidly for small crack depth (due to the relatively higher surface stresses). For deeper crack depth, there tends to be relatively more rapid depth growth due to the membrane stress contribution.

Figure 6.5 shows the same case, with residual stresses added. The residual stresses had the greatest effect on the membrane stress case because the surface length tended to grow more rapidly due to the contributions of the higher R-ratio near the inside surface. There is a slight decrease in the aspect ratio for the other types of loading.

The initial aspect ratio was then changed to a/l = 0.12, simulating an initial flaw with depth of 3 mm (0.118 in.) and a surface length of 25.4 mm (1.0 in.). The results are shown in Figure 6.6. The following observations are made.

When the initial flaw has a relatively long surface length, the aspect ratio initially tends to increase due to the crack growing predominantly in the depth direction.

At crack depths beyond 40-50% through-wall, the crack growth trajectories tend to grow to the similar aspect ratios observed for the case where a very large initial aspect ratio was used.

In Figure 6.7, the same case is run for a 12.7 mm (0.5-in.) thick component [initial aspect ratio a/l = 0.12 and initial crack depth of 3 mm (0.118 in.)]. A similar behavior is observed, except that the initial flaw begins more rapidly.

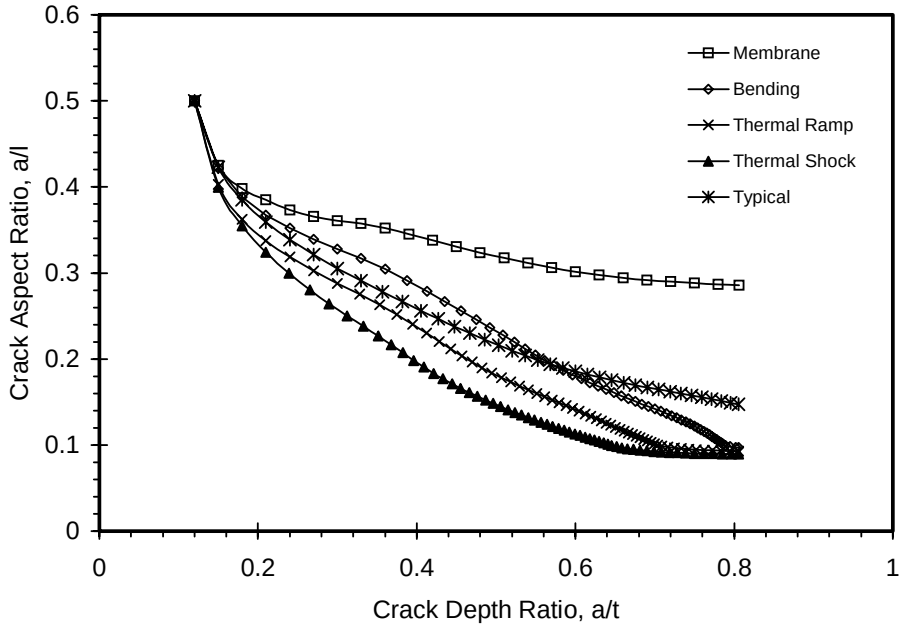


**Figure 6.5 Crack Growth Trajectories for 25.4 mm (1-in.) Thick Carbon Steel with Residual Stresses, Initial a/l = 0.5**

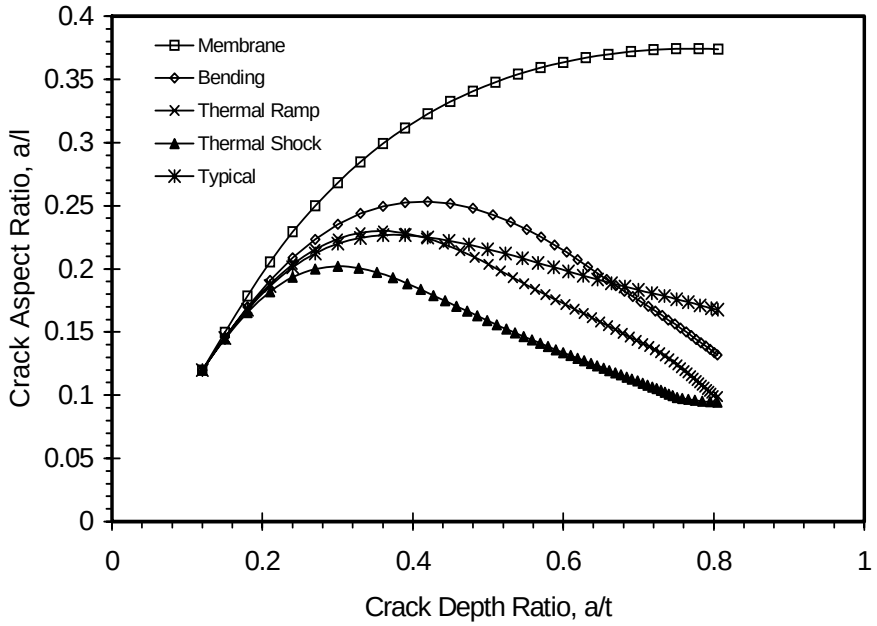


**Figure 6.6 Crack Growth Trajectories for 25.4 mm (1-in.) Thick Carbon Steel with No Residual Stresses, Initial a/l = 0.12**

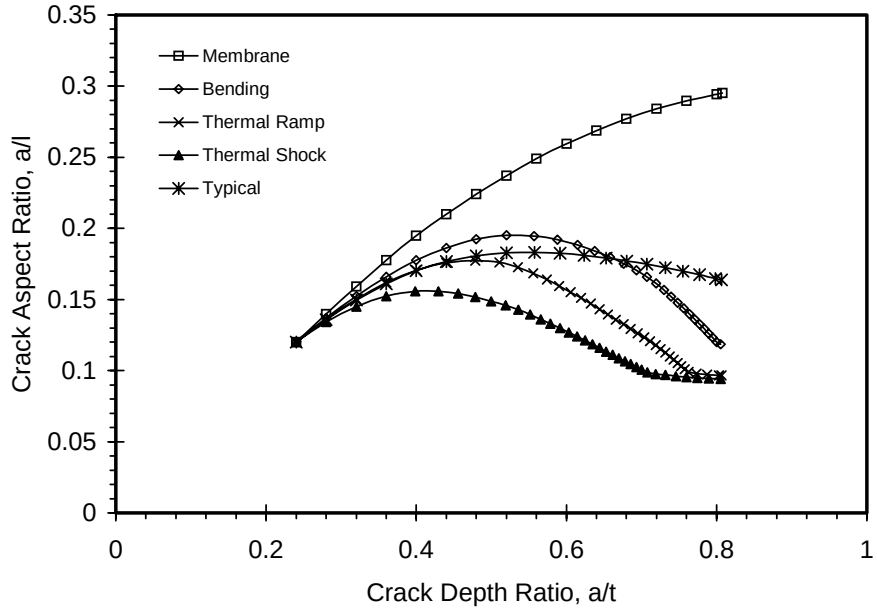


**Figure 6.7 Crack Growth Trajectories for 12.7 mm (0.5-in.) Thick Carbon Steel Without Residual Stresses, Initial a/l = 0.12**

There were no significant changes in the crack growth trajectories (as compared to the no-residual stress cases) when considering a change to stainless steel or by considering the effects of constant through-wall high residual stresses.

A portion of the results in this study has been shown in other similar studies. In Scott and Thorpe (1981), researchers at the United Kingdom Atomic Energy Authority (UKAEA) made predictions for the development of crack growth shapes for fatigue crack growth. Figure 6.8 shows crack growth trajectories for tensile (membrane loadings) that are not unlike those from this work. As the crack approaches a/t = 0.8, the value of a/c was about 0.8 (a/l = 0.4). Similarly, for bending loading, there was a decrease in aspect ratio as shown in Figure 6.9. Iida et al. (2000) contains experimental work that exhibits the same behavior.

The significance of the current examples is that steeper gradients through the wall are shown to result in significantly lower aspect ratios as the crack tip approaches the outside pipe wall. On the other hand, introduction of some portion of membrane loading into the load set pair results in more rapid depth crack growth such that surface crack growth does not lead to such small aspect ratios.

## 6.4 Thermal Striping Evaluation

As discussed in Section 3, field experience has shown aspect ratios quite low for crack leakage. However, it was observed that most field experience is not due to thermal transients as evaluated above but to thermal stratification, turbulence penetration, or hot/cold fluid mixing. To evaluate the effect of these more rapid loadings, stresses were developed for a 0.5-Hz sinusoidal thermal cycling in a 25.4 mm (1 in.) thick stainless steel pipe that would produce a 69 MPa (10 ksi) stress range at the inner surface. This was then combined with a typical 38.6 MPa (5.6 ksi) tensile membrane stress to account for a mean stress effect due to internal pressure. The third-order polynomial stress distributions shown in Figure 6.10 are a simplification of the actual stress distribution because the surface stress gradients were much steeper than shown and the stress ranges deeper in the pipe wall were not affected as much as shown by the cubic curve fit.

Three cases were evaluated. Two were with an initial a/l = 0.12 aspect ratio; one of these also included the residual stress distribution. The third case was an evaluation for an initial semicircular crack (a/l = 0.5). The results are shown in Figure 6.11.

Because most of the stress cycling was at the inside surface, the crack initially grew mainly in the length direction. The “equilibrium” aspect ratio was less than 0.1 for the case without residual stresses. For the case with residual stresses, the growth was essentially all in the length direction and the crack arrested at a depth $a/t \approx 0.2$.

The results of this evaluation demonstrate that highly cyclic loadings such as those attributed to thermal striping, turbulence penetration, and thermal mixing, can lead to mainly surface cracking with the associated, much lower, crack aspect ratios.

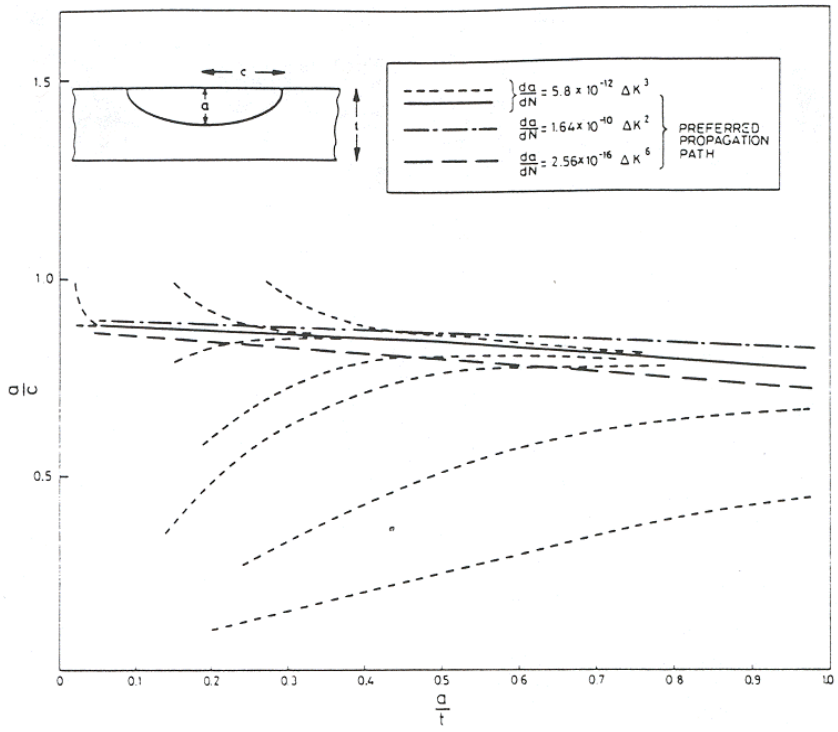


**Figure 6.8 Crack Growth Trajectories from UKAEA Study – Tensile Loading**

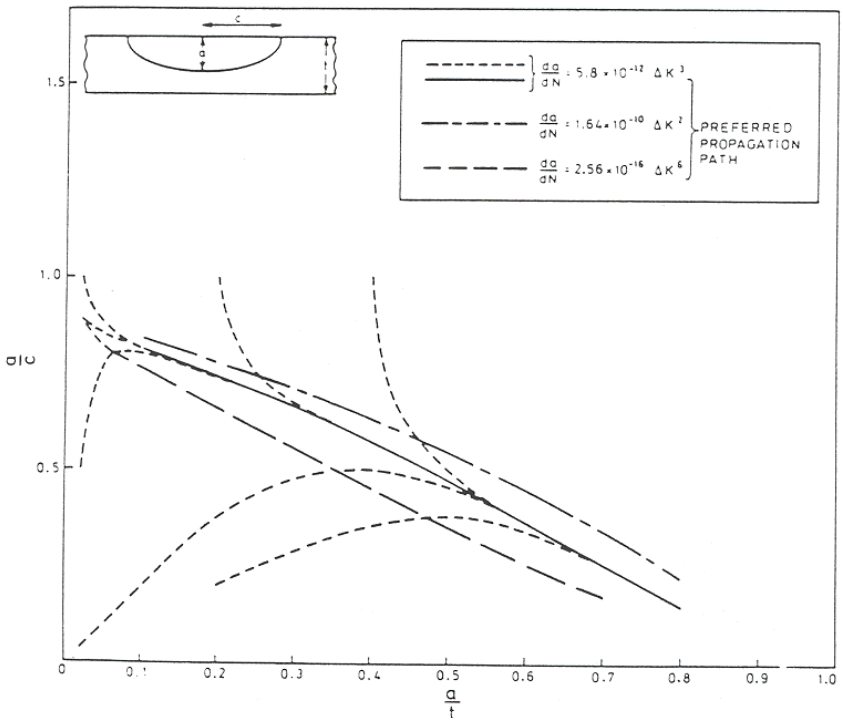


**Figure 6.9 Crack Growth Trajectories from UKAEA Study – Bending Loading**

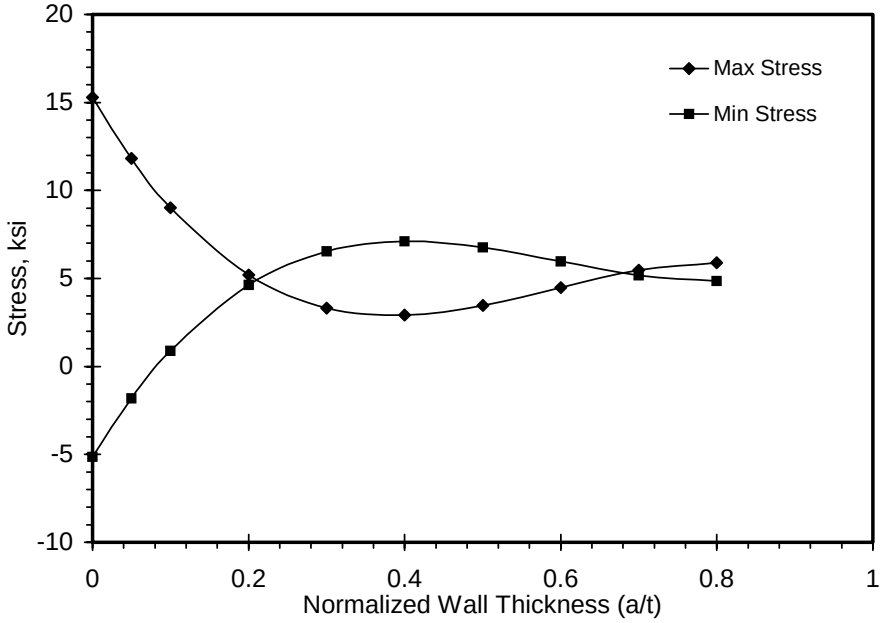


**Figure 6.10 Stress Distributions for Thermal Striping Analysis (1 ksi = 6.897 MPa)**

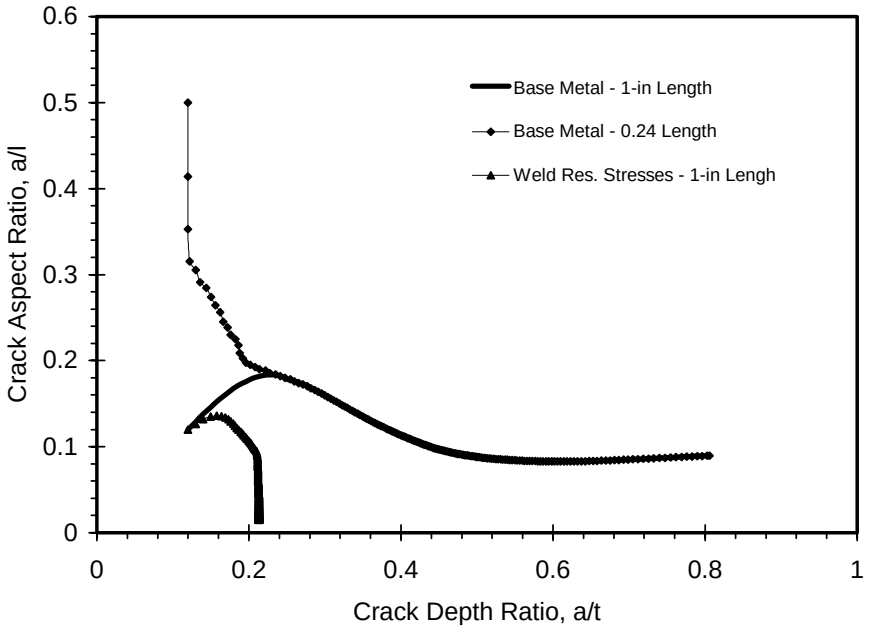


**Figure 6.11 Trajectories for Striping Evaluation (25.4 mm = 1 in.)**

## 6.5 Constant Versus Variable Aspect Ratio Crack Growth Analysis

Most of this crack growth evaluation concentrated on variable aspect ratio crack growth and the changes of aspect ratio for various types of loading. However, crack growth calculations are more difficult analytically than when one assumes a constant aspect ratio. To demonstrate the difference in results obtained, analyses were conducted for two cases. For both, a 12.7 mm (0.5 in.) carbon steel pipe with no residual stresses was assumed. An initial crack 3 mm (0.118 in.) deep and 25.4 mm (1 in.) long was assumed for the variable aspect ratio case. Then, constant aspect ratio crack growth for several assumed aspect ratios was computed, starting at the initial depth of a/t = 0.3, the Section XI Appendix L depth for a 12.7 mm (0.5 in.) thick component.

Figure 6.12 shows the results for the case for cycling only due to the assumed thermal shock transient. For this case, the crack growth rate for an a/l = 0.166 crack is less than that for the variable aspect ratio crack. Assuming a fixed aspect ratio of a/l = 0.1 produces a higher crack growth rate except for very deep cracks.

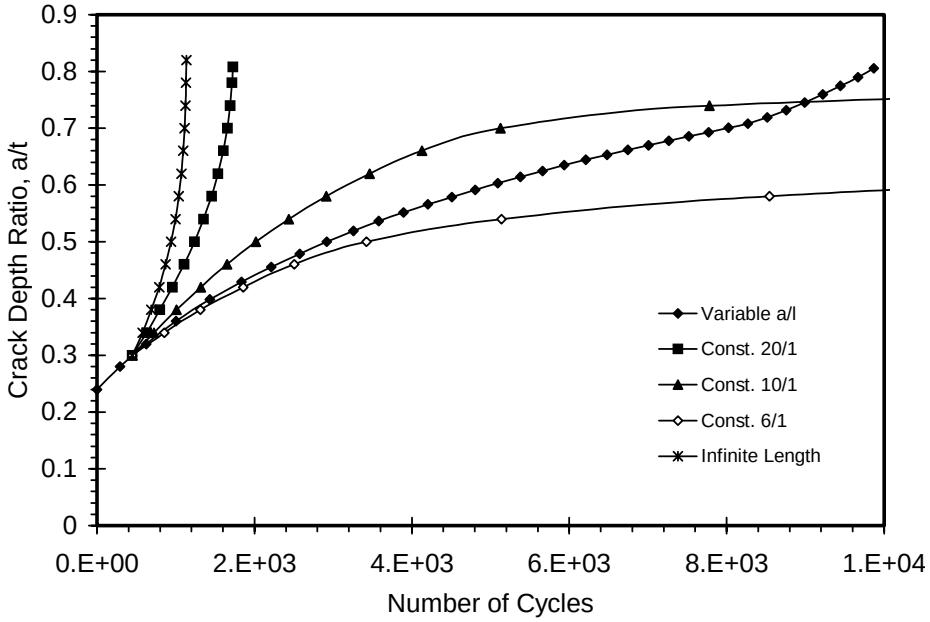


**Figure 6.12 Crack Growth for Thermal Shock Transient for Fixed and Variable Aspect Ratios**

The same evaluation for the typical transient demonstrated that the crack growth rate for all aspect ratios exceeds that of the variable aspect ratio crack, as shown in Figure 6.13. In this case, the assumption of a/l = 0.166 provides a very good approximation. This case is judged to be much more representative than only considering thermal shock cycling. Crack growth will generally be due to combinations of loads including pressure-induced membrane stresses and piping bending loads (producing primarily membrane-type loads) with some contributions due to both ramp and thermal transients.

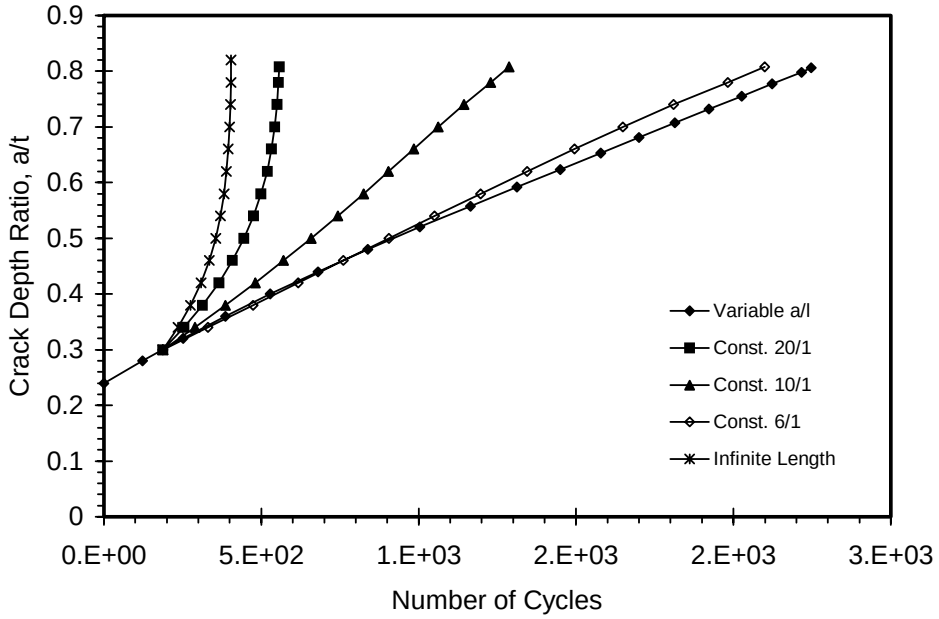


**Figure 6.13 Crack Growth for Typical Transient for Fixed and Variable Aspect Ratios**

## 6.6 Concluding Remarks

The deterministic crack growth calculations of this section show that a constant aspect ratio, a/l = 0.166, should be applicable for most plant transient crack growth evaluations. Alternative approaches may, however, be required for load set pairs where severe stress gradients exist. Section 7 develops a methodology to evaluate the effects of thermal gradient stresses and the initiation and growth of multiple fatigue cracks on component integrity.

# 7 Flaw Tolerance for Multiple Fatigue Cracks

This section describes the development of a methodology to address inspection frequencies that will ensure that the postulated cracks of the type presented in Section 5 do not exceed the Section XI allowable flaw sizes. Factors that govern the inspection frequencies include

1. the postulated through-wall depth and aspect ratio of the initial crack

2. the potential for small cracks to initiate at multiple sites and then link together to form single cracks that have long aspect ratios

3. the cyclic stresses that can grow the fatigue cracks

4. the effect of through-wall stress gradients and differences in fatigue crack growth for membrane stresses versus thermal gradient stresses

5. stainless steel or low-alloy steel piping material

6. the levels of primary stress and the acceptable sizes for the end-of-life flaws.

Sections 4 and 5 provide needed information regarding the appropriate depths for postulated cracks. However, no such source of information was available to guide the selection of flaw aspect ratios for these postulated flaws. Because the initial aspect ratio was known to be a critical input to the fatigue crack growth calculations, the work described in this section gives detailed consideration to flaw aspect ratios. In this regard, field failures show that fatigue cracking often results in relatively long flaws with large aspect ratios because several small fatigue cracks initiate and then link together into a single long crack. Therefore, it is often inappropriate to assume flaws with small aspect ratios, such as the 6:1 aspect ratio often used for ASME Code flaw tolerance evaluations. On the other hand, it may be overly conservative to always assume a full 360-degree circumferential crack.

The evaluations, as reported in the following sections, identify equivalent single crack aspect ratios between the extremes of a 6:1 ratio and a full circumferential crack that adequately account for the effects of multiple crack initiation. A final topic describes examples of calculations to demonstrate an Appendix L evaluation.

## 7.1 Overview of Methodology

The objective was to develop a methodology to calculate the allowable operating periods between Appendix L successive inspections. These operating periods are based on fatigue crack growth analyses using existing Section XI flaw evaluation rules. The initial crack depths, as determined by the method described in Sections 4 and 5 of this report, correspond to the flaw depths that can be detected with a high degree of reliability by ultrasonic examinations. End-of-operating-period flaw depths are based on Section XI fracture mechanics criteria for determining acceptable flaw sizes. The appropriate method for determining allowable flaw sizes depends on the piping material (austenitic or ferritic steel) and on the

relevant failure mode (limit load, elastic-plastic fracture mechanics, or linear elastic fracture mechanics. Flaw depths from Section XI have safety factors placed on the applied loads used to calculate unstable flaw sizes. The Appendix L procedure reduces calculated operating periods by a factor of two.

The Appendix L procedure is well defined in terms of 1) postulated flaw depths, 2) the allowable flaw depth at the end of the operating period, and 3) the rules for calculating the fatigue crack growth for the operating period. The one element that is most difficult to define is the beginning-of-operating-period length of the flaw (or aspect ratio) that should be postulated. It was determined from sensitivity calculations that alternative assumptions regarding flaw aspect ratios can lead to large differences in the calculations for allowable operating periods. There is evidence also from plant operating experience that flaw aspect ratios can become relatively large, and, in some cases, flaws can extend around the full pipe circumference. Cycle stresses can extend around the full inner circumference of a pipe, and fatigue cracks initiated at multiple sites can become one single long crack. The evaluations described here address this mechanism in detail.

Alternative treatments of flaw aspect ratio are as follows:

1. Calibration of the probabilistic fracture mechanics model to redefine the depth of the initiated fatigue crack from the 3 mm (0.118 in.) depth of the ANL data correlations to address a flaw depth of 0.5 mm (0.02 in.) that is more consistent with the initiation process for fatigue cracks.

2. Determination of the aspect ratio for a single crack [depth = 0.5 mm (0.02 in.)] that gives the same probability of through-wall crack (i.e., leak probability) as predicted by the multiple crack initiation model of the pc-PRAISE code.

3. Determination of the decrease in the aspect ratio for a single crack as it grows from the 0.5 mm (0.02 in.) initiated depth to become the postulated depth (detectable size) used for the damage tolerance evaluation of Appendix L.

4. Determination of the time period to grow the flaw of the multiple crack model from the initial postulated depth to the maximum allowable flaw depths permitted by ASME Section XI.

## 7.2 Calibration for 0.5 mm (0.02 in.) Deep Initiated Crack

The methodology began with calculations of fatigue crack growth using a flaw depth of 0.5 mm (0.02 in.). Consistent with ANL research on fatigue cracking, this depth was assumed to define the depth at which the processes of fatigue crack initiation end and fatigue crack growth process begins. Flaws of about 0.5 mm (0.02 in.) correspond to the smallest flaws for which crack growth can be predicted by fracture mechanics methods of the Paris crack growth law ($da/dN = C\ \Delta K^n$). On the other hand, fatigue tests with standard push-pull specimens determine fatigue lives by the load drop method, which corresponds to a crack depth of about 3 mm (0.118 in.). Therefore, calculations with the pc-PRAISE code based on the 3 mm (0.118 in.) crack required a modification to ensure that the results apply to the small 0.5 mm (0.02 in.) cracks of interest.

The modified pc-PRAISE calculations assigned a 0.5 mm (0.02 in.) depth to the initiated crack but also assigned a factor (less than unity) to account for the fewer number of stress cycles to produce a 0.5 mm (0.02 in.) crack compared to the number of cycles for a 3 mm (0.118 in.) crack. Rather than selecting a universal value for this factor based on the ANL work, we assigned this factor on a case-by-case basis (depending on the dimensions of the pipe, the piping material and the cyclic stresses). Calculations of leak probabilities for a 3 mm (0.118 in.) deep initial crack were performed first. This was followed by a series of calculations for the 0.5 mm (0.02 in.) crack, each assuming a different value (between 0.0 and 1.0) of the ratio between fewer number cycles to initiate a 0.5 mm (0.02 in.) crack compared to the number of cycles to initiate a 3 mm (0.118 in.) crack. The appropriate value of the ratio was selected such as to give leak probabilities that were approximately the same for the two values of initial flaw depth.

Figure 7.1 illustrates the calibration procedure for the case of a 254 mm (10 in.) diameter stainless steel pipe with a high level of cyclic stress [alternating stress = 897 MPa (130 ksi)]. The calculated leak probability for the baseline 3 mm (0.118 in.) initiated crack is shown with the solid curve, whereas trial results for the 0.5 mm (0.02 in.) crack are shown by the set of dashed curves. It is seen that the curve for SNFACTOR = 0.60 gives good agreement with the baseline case, and this value was selected for use for the pc-PRAISE calculations.

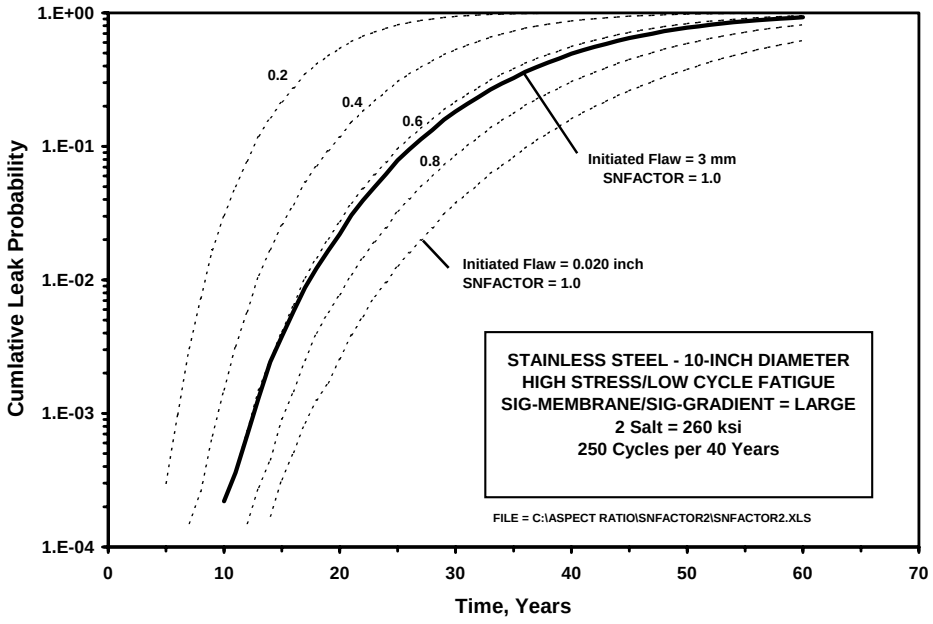


**Figure 7.1 Sample Calibration of pc-PRAISE Calculations to Account for Difference in Cycles to Fatigue Crack Initiation for 0.5 mm (0.02 in.)-Deep Crack Versus ANL Fatigue Curves for 3 mm (0.118 in.) Initiated Crack (25.4 mm = 1 in.)**

Table 7.1 gives the complete set of results for the pc-PRAISE calculations of the present report. The factor ranged from 0.05 to 0.80. The factor tends to have higher values for high-cycle stresses [alternating stress = 897 MPa (130 ksi)] than for low value of cyclic stress [alternating stress = 207 MPa (30 ksi)]. The values of the SNFACTOR given in Table 7.1 for the 207 MPa (30 ksi) alternating stress are presented only for purposes of information and were not used for any of the subsequent calculations presented in the following sections.

**Table 7.1 Calibrations of pc-PRAISE Calculations to Account for Difference in Cycles to Fatigue Crack Initiation for 0.5 mm (0.020-In.)-Deep Crack Versus ANL Fatigue Curves for 3 mm (0.118 in.)-Initiated Crack**

| NPS Pipe Size mm (in.) | SNFACTOR | | | |
|---|---|---|---|---|
| | Stainless Steel | | Low-Alloy Steel | |
| | High Stress Low Cycle | Low Stress High Cycle | High Stress Low Cycle | Low Stress High Cycle |
| 50.8 (2) | 0.60 | 0.05 | 0.60 | 0.50 |
| 254.0 (10) | 0.60 | 0.05 | 0.70 | 0.60 |
| 55.9 (22) | 0.70 | 0.20 | 0.80 | 0.60 |

## 7.3 Equivalent Single Crack Aspect Ratio

The pc-PRAISE models for fatigue crack initiation and growth simulate service experience by assuming that cracks can initiate at multiple sites around the circumference of a pipe. As cracks initiate at adjacent sites, these cracks will individually grow and become both deeper and longer. Eventually the lengths of the adjacent cracks will result in the linking of two or more adjacent cracks to form a single long crack. This process in the limit can create one long circumference crack that extends over the full circumference of the pipe. It is more convenient to address the linkage process with fracture mechanics models that simulate only a single crack. If such a model is applied, the initial length (or aspect ratio) of the single crack must be sufficient to give leak probabilities that are consistent with the multiple cracking behavior. The following discussion describes the method used to establish aspect ratios of these equivalent single cracks.

The multiple crack model was first developed to address the charging line example as described in Section 5 of this report. In this case, the piping had a nominal diameter of 76.2 mm (3 in.) and a wall thickness of 11.1 mm (0.438 in.), and the inner surface of the pipe was subjected to thermal transients as described in Section 5. Calculations to establish the aspect ratio of the equivalent single crack were performed with the pc-PRAISE code as follows.

The model for multiple cracking assumed that each initiation site was 50.8 mm (2 in.) long, which gave a total of four sites for fatigue cracks to initiate around the pipe circumference. Cracking was assumed to initiate at random times in accordance with the probabilistic fatigue correlations. All cracks had an initiated crack depth of 0.5 mm (0.02 in.). The initiated crack lengths were sampled from a length distribution described in Section 5. It was further assumed that cracks in a given weld initiated at all sites

at the same time, all cracks in a given weld had the same aspect ratio, and that the random variations in the crack growth rate parameter were addressed by giving the same parameter for all cracks in each simulated weld.

Another set of pc-PRAISE calculations was performed that assumed only single cracks. The initiation time for this crack was simulated in the same manner as for the multiple crack model. The initial depths of the cracks were 0.5 mm (0.02 in.). The aspect ratios of the 0.5 mm (0.02 in.) deep crack was not simulated but was assigned a range of deterministic values. Values ranged from small aspect ratios (2:1) to very large values (greater than 1000:1). The random parameter of the crack growth rate law was simulated from the same statistical distribution as was used for the multiple crack model. The calculated leak probabilities for the single crack were sensitive to the assigned values of the aspect ratios. Large aspect ratios gave leak probabilities that were equal to or greater than those from the multiple crack model. Small aspect ratios gave leak probabilities that were significantly less than predicted by the multiple crack model.

Figure 7.2 shows some results for the charging line example of Section 5. The plot compares leak probabilities from the single crack model to probabilities from the multiple crack model. In these calculations, the membrane stress component was assigned a stress range of 310 MPa (45 ksi), with the balance of the cyclic stress being treated as thermal gradient stress. It is seen in Figure 7.2 that the leakage probabilities for the 6:1 single crack are nearly a factor of 10 less than the leak probabilities from the multiple crack model. When the prescribed aspect ratio was increased to about 30:1, the leak probabilities for the single crack model become essentially the same as those predicted by the multiple crack model. This shows that the equivalent single crack must have an aspect ratio of 30:1 to approximate the predictions of the more realistic multiple crack model.

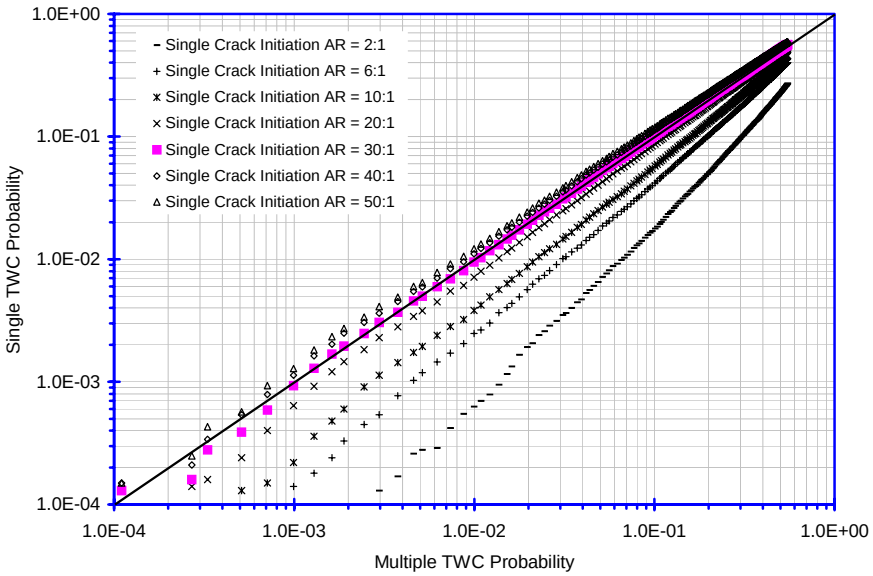


**Figure 7.2 Example of Calibration for Aspect Ratio of Equivalent Single Crack That Gives Same Through-Wall Crack Probability as Predicted by Multiple Cracking Model**

After the methodology for establishing the aspect ratios for equivalent single cracks was developed and demonstrated for the parameters of the charging line example of Section 5, more general calculations were performed to address stainless and low-alloy steels, wall thicknesses ranging from 5.54 mm (0.218 in.) to 54 mm (2.125 in.), and a wide range of cyclic membrane stresses expressed as a fraction of the thermal gradient stresses. Most applications of Appendix L are expected to involve high-amplitude thermal fatigue stresses, so the calculations were limited to the case of a relatively high level of cyclic stress [$2S_{ALT}$ = 1793 MPa (260 ksi)]. Because the methodology was based entirely on relative probabilities associated with crack growth calculations, the results should be insensitive to the value of $2S_{ALT}$ used.

Results of calculations for equivalent single cracks are summarized in Tables 7.2 and 7.3. In all cases, the aspect ratios of the equivalent single cracks were determined to be much greater than the 6:1 aspect ratio of the Section XI flaw used for ASME Code evaluations. In many cases, the aspect ratios were

**Table 7.2 Results of Calibrations to Determine Aspect Ratio of Equivalent Single Crack [Depth = 0.5 mm (0.02 in.)] that Gives the Same Leak Probabilities as Predicted by Multiple Cracking Model for Austenitic Stainless Steel Piping**

| Austenitic Stainless Steel Aspect Ratio of Equivalent Single Crack with Depth 0.02 in. | | | | | |
|---|---|---|---|---|---|
| $\sigma_M/\sigma_G$ | 2 in. Schedule 80 | 2 in. Schedule 160 | 6 in. Schedule 160 | 10 in. Schedule 160 | 22 in. Schedule 160 |
| | t = 0.218 in. | t = 0.344 in. | t = 0.719 in. | t = 1.125 in. | t = 2.125 in. |
| 0.0 | 118 | 190 | 590 | 977 | 1750 |
| 0.1 | 44 | 80 | 178 | 275 | 420 |
| 0.25 | 30 | 45 | 70 | 94 | 70 |
| 1.0 | 22 | 23 | 29 | 37 | 31 |
| 3.0 | 21 | 22 | 24 | 28 | 21 |
| 25.4 mm = 1 in. | | | | | |

**Table 7.3 Results of Calibrations to Determine Aspect Ratio of Equivalent Single Crack [Depth = 0.5 mm (0.02 in.)] that Gives the Same Leak Probabilities as Predicted by Multiple Cracking Model for Low-Ally Steel Piping**

| Low Alloy Steel Aspect Ratio of Equivalent Single Crack with Depth 0.02 in. | | | | | |
|---|---|---|---|---|---|
| $\sigma_M/\sigma_G$ | 2 in. Schedule 80 | 2 in. Schedule 160 | 6 in. Schedule 160 | 10 in. Schedule 160 | 22 in. Schedule 160 |
| | t = 0.218 in. | t = 0.344 in. | t = 0.719 in. | t = 1.125 in. | t = 2.125 in. |
| 0.0 | 69 | 135 | 600 | 1120 | 2350 |
| 0.1 | 33 | 65 | 194 | 450 | 1050 |
| 0.25 | 21 | 33 | 116 | 280 | 520 |
| 1.0 | 20 | 26 | 60 | 120 | 200 |
| 3.0 | 19 | 24 | 45 | 78 | 120 |
| 25.4 mm = 1 in. | | | | | |

found to be very large, particularly for piping with large wall thicknesses and for cyclic stresses that consist largely of thermal gradient stresses with little or no component of membrane stresses.

## 7.4 Aspect Ratio of Appendix L Postulated Crack

The calculations discussed in Section 7.3 established aspect ratios for equivalent single cracks having depths of 0.5 mm (0.02 in.), which is the minimum depth for which fatigue crack growth can be predicted with fracture mechanics models (e.g., Paris law). These crack depths were much shallower than the depths of the postulated Appendix L flaws described in Section 6. In this section, changes in aspect ratios as flaws grow from 0.5 mm (0.02 in.) depths to the depths of the Appendix L postulated cracks were evaluated. In all cases, the aspect ratios decrease significantly.

Deterministic calculations of fatigue crack growth were performed with the pc-PRAISE code. The initial flaw depths were 0.5 mm (0.02 in.), and the initial aspect ratios were those of Tables 7.2 and 7.3. Each crack growth calculation addressed a specific material (stainless steel or low-alloy steel), a specific pipe wall thickness, and specific transients (ratio of alternating membrane and thermal gradient stresses). Figure 7.3 shows typical results of four such calculations that started with an initial crack depth of 0.5 mm (0.02 in.) and continued until the crack depth became through-wall. In these calculations, the interest was not in the absolute time to attain through-wall crack depths but rather in the decrease in the crack aspect ratio as the flaw depth increased.

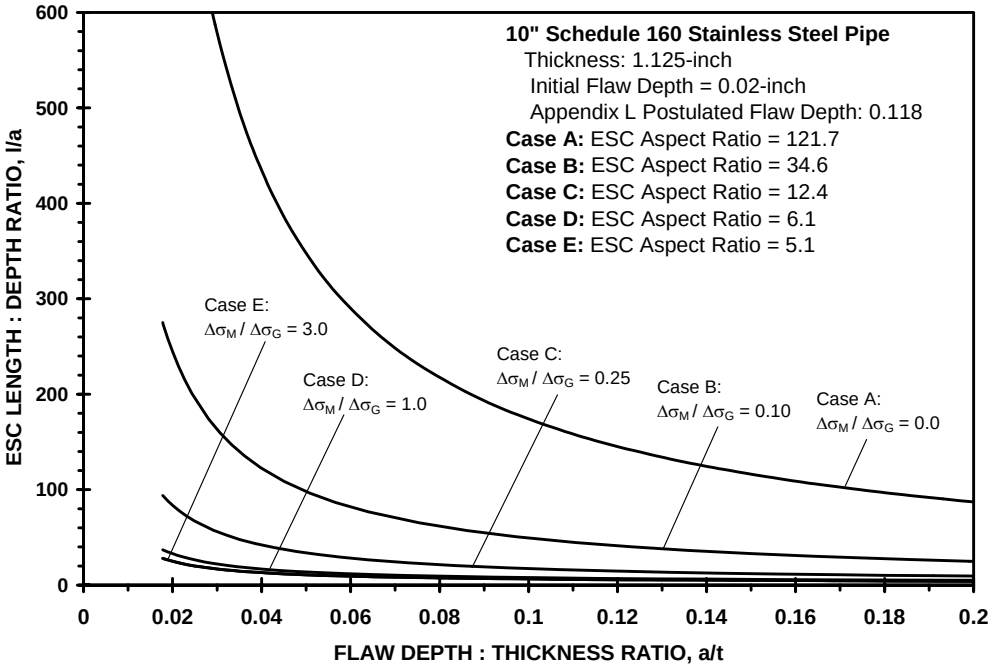


**Figure 7.3 Sample Calculation of Change in Aspect Ratio of Equivalent Single Crack That Gives the Same Through-Wall Crack Probability as Predicted by Multiple Cracking Model (25.4 mm = 1 in.)**

All four curves of Figure 7.3 assumed the same level of cyclic stress but had different fractions of this cyclic stress taken to be membrane stress as opposed to thermal gradient stress. The upper curve assumes that the stress is 100% thermal gradient stress. The other three curves assumed increasing fractions of membrane stress. In all cases, the aspect ratios began with relatively large values and then decreased significantly as the flaw depths increased. Although the fracture mechanics model simulated fatigue crack growth in both the depth and length directions, the amount of flaw growth in the length direction was insufficient to prevent a significant decrease in aspect ratio. The objective of generating the curves of Figure 7.3 was to determine the flaw aspect ratios for the depths of the Appendix L flaws as defined in Section 6. Labels for the curves of Figure 7.3 indicate both the initial aspect ratios for the 0.5 mm (0.02 in.) flaws and the decreased aspect ratios for the deeper flaws postulated by Appendix L.

A matrix of deterministic crack growth calculations was performed for parameters of Tables 7.2 and 7.3, which covered stainless and low-alloy steels, wall thicknesses from 5.54 mm (0.218 in.) to 54 mm (2.125 in.), and various ratios of membrane to gradient stresses ranging from 0.0 to 3.0. Tables 7.4 and 7.5 show results of these calculations and indicate the aspect ratios associated with the depths of the Appendix L postulated flaws.

**Table 7.4 Stainless Steel Equivalent Single Crack (ESC) Aspect Ratios for Appendix L Postulated Flaw**

| $\sigma_M/\sigma_G$ | 2 in. Schedule 80 a/t = 0.113 | 2 in. Schedule 160 a/t = 0.118 | 6 in. Schedule 160 a/t = 0.132 | 10 in. Schedule 160 a/t = 0.143 | 22 in. Schedule 160 a/t = 0.146 |
|---|---|---|---|---|---|
| | t = 0.218 in. | t = 0.344 in. | t = 0.719 in. | t = 1.125 in. | t = 2.125 in. |
| 0.0 | 95.6 | 93.9 | 124.3 | 121.7 | 113.1 |
| 0.1 | 35.7 | 39.6 | 37.7 | 34.6 | 27.6 |
| 0.25 | 24.4 | 22.4 | 15.3 | 12.4 | 6 |
| 1.0 | 18 | 12 | 7.4 | 6.1 | 3.5 |
| 3.0 | 17 | 9.7 | 6.5 | 5.1 | 2.8 |
| 25.4 mm = 1 in. | | | | | |

**Table 7.5 Low-Alloy Steel Equivalent Single Crack (ESC) Aspect Ratios for Appendix L Postulated Flaw**

| $\sigma_M/\sigma_G$ | 2 in. Schedule 80 a/t = 0.113 | 2 in. Schedule 160 a/t = 0.118 | 6 in. Schedule 160 a/t = 0.132 | 10 in. Schedule 160 a/t = 0.143 | 22 in. Schedule 160 a/t = 0.146 |
|---|---|---|---|---|---|
| | t = 0.218 in. | t = 0.344 in. | t = 0.719 in. | t = 1.125 in. | t = 2.125 in. |
| 0.0 | 56.1 | 67.1 | 127.0 | 140.1 | 152.4 |
| 0.1 | 26.9 | 32.6 | 41.6 | 56.7 | 68.6 |
| 0.25 | 17.3 | 16.9 | 25.2 | 35.7 | 34.4 |
| 1.0 | 16.5 | 13.5 | 13.6 | 15.9 | 14.0 |
| 3.0 | 15.7 | 12.6 | 10.7 | 10.9 | 9.2 |
| 25.4 mm = 1 in. | | | | | |

The results shown in Tables 7.4 and 7.5 define aspect ratios that can be used as inputs to Appendix L fatigue crack growth calculations performed to establish inspection periods. In this approach, the fracture mechanics model accounts for crack growth in both the depth and length directions. Table 7.4 is used to define the equivalent single crack aspect ratio for the application example in Section 7.5.

## 7.5 Application Example

The calculation in this section is an example intended to illustrate how the research findings in Sections 4 through 7 can be incorporated in a flaw tolerance evaluation. This example also demonstrates how the initiation and subsequent growth of multiple fatigue cracks can be accounted for in an Appendix L flaw tolerance assessment on a plant component subject to multiple design transient load pair combinations. The 76.2 mm (3 in.) Schedule 160 austenitic stainless steel Westinghouse charging nozzle, described in Section 5, was selected for this example.

### 7.5.1 Flaw Tolerance Evaluation Method

Prior to performing a flaw tolerance assessment, the absence of any indication or relevant indication at the component location where the fatigue usage limits are exceeded, or projected to be exceeded before the end of the evaluation period, must be verified first . In Appendix L, an indication is considered relevant if it exceeds the applicable acceptance standards referenced in Table IWB-3410-1. Otherwise, Appendix L is not applicable and the flaw then must be evaluated in accordance with IWB-3600. After the absence of any relevant defects has been verified, a flaw tolerance assessment is used to determine the maximum allowable operating period between successive inspections.

In this example, the current Appendix L flaw tolerance procedures were changed to incorporate the results and conclusions discussed in Section 7.4. The changes associated with the basic Appendix L flaw tolerance procedure are described here:

1. Determine the stresses at the postulated reference flaw location for normal operating (including upset and test), emergency, and faulted conditions. This example was based only on normal and upset conditions. In an actual application, the analyst would be required to consider both conditions, and the resulting successive inspection requirements would be based on the limiting case.

2. Postulate the existence of a hypothetical reference flaw. The Appendix L initial postulated reference flaw depths were reduced to the flaw depths specified in the ASME Section XI Table IWB-3514-1 for 6:1 aspect ratio flaws. The bases for this change were established in Sections 4 and 5. The initial postulated aspect ratio for the hypothetical flaw is obtained from Tables 7.4 and 7.5.

3. Determine the postulated flaw end-of-evaluation period flaw depth and the maximum allowable flaw depths for the applicable failure criteria and determine the time (allowable operating period) necessary for the postulated reference flaw to grow to the maximum allowable flaw depth.

4. Using the allowable operating period in step 3, define the successive inspection schedule. In accordance with Appendix L, the time between successive inspections cannot exceed 10 years.

### 7.5.2 Component Stresses

The operating pressure and temperature assumed for the charging nozzle in this example was 15.5 MPa (2.25 ksi) and 288°C (550°F). It was further assumed that primary bending stresses were negligible and the primary membrane stresses were a function of pressure only. Because emergency and faulted loads were not available, the flaw tolerance computations in this example considered only the normal and upset design transient load pair cycles and alternating stresses in Table 5.2.

Because the transient data in Table 5.2 identified only the peak alternating stress ($S_{ALT}$) for surface conditions, the nature of the through-wall stress distribution had to be assumed. Therefore, in this example, the peak alternating stress range ($2S_{ALT}$) for each load pair combination was decomposed into a uniform membrane component and a nonlinear thermal gradient component. Accordingly, a 138 MPa (20-ksi) uniform membrane alternating stress range and the remaining alternating stress was assigned to the nonlinear thermal gradient component. The resulting membrane and gradient stresses for each load pair combination are shown in Table 7.6.

Sensitivity evaluations of allowable operating periods, previously discussed in this section, show that the growth of fatigue cracks to through-wall depths is influenced significantly by the stress gradients. If much of the peak stresses are due to thermal gradient stresses, the level of stress decreases rapidly as the crack grows into the vessel wall. High stress gradients reduce the rate of crack growth relative to the rates for a membrane stress (uniform distribution). Therefore, the initial equivalent single crack aspect ratios in Tables 7.4 and 7.5 are dependent on the cyclic membrane stress-to-gradient (linear and nonlinear) stress ($\Delta\sigma_M/\Delta\sigma_G$).

If crack growth is caused by only a single dominant operational transient (or load pair), the ratio of membrane stress to gradient stress is readily determined. On the other hand, fatigue crack growth calculations must usually account for a collection of load pairs, and there is no single ratio of membrane to gradient stress. Thus, a weighting of the individual ratios of membrane stress to gradient stress is necessary to establish an effective ratio for the collection of load pairs. This method uses the Paris Law for fatigue crack growth to estimate the relative amount of crack growth caused by the stresses from each load pair.

The Paris Law is given by

$$da/dN = C\,(\Delta K)^m$$

This relationship predicts that the amount of crack growth from each load pair is proportional to the total number of stress cycles for the load pair and to the cyclic stress level for the load raised to the power m. The following equation was derived to appropriately weight the stress ratio of each load pair to establish a single ratio of membrane to gradient stress to characterize a collection of load pairs:

**Table 7.6 Sample Calculation of Equivalent Membrane-to-Gradient Stress Ratio for a Component Subjected to Multiple Transients**

| LOAD PAIR | $2Salt_i$ | $(\Delta\sigma_M)_i$ | $(\Delta\sigma_G)_i$ | $(\Delta\sigma_M/\Delta\sigma_G)_i$ | N | n | $Q_i = n\,(Salt)^4$ | $Q_i/\Sigma Q$ | $(Q_i/\Sigma Q)_i \times (\Delta\sigma_M/\Delta\sigma_G)_i$ |
|---|---|---|---|---|---|---|---|---|---|
| Loss of charging-prompt retum/null | 266.88 | 20 | 246.88 | 0.081 | 66 | 120 | 3.80E+10 | 2.83E-01 | 2.29E-02 |
| Loss of charging-delayed return/null | 265.56 | 20 | 245.56 | 0.081 | 66 | 12 | 3.73E+09 | 2.77E-02 | 2.26E-03 |
| Normal chatging and letdown shutdown/null | 202.12 | 20 | 182.12 | 0.110 | 182 | 60 | 6.26E+09 | 4.65E-02 | 5.11E-03 |
| Loss of letdown-delayed return/null | 112.1 | 20 | 92.1 | 0.217 | 1673 | 8 | 7.90E+07 | 5.87E-04 | 1.28E-04 |
| Reactor trip/OBE | 108.46 | 20 | 88.46 | 0.226 | 1993 | 20 | 1.73E+08 | 1.29E-03 | 2.91E-04 |
| Loss of letdown-delayed return/flow increase | 94.94 | 20 | 74.94 | 0.267 | 4565 | 4 | 2.03E+07 | 1.51E-04 | 4.03E-05 |
| Loss of charging-prompt return/flow increase | 92.94 | 20 | 72.94 | 0.274 | 355 | 120 | 5.60E+08 | 4.16E-03 | 1.14E-03 |
| Step increase in charging/flow increase | 83.48 | 20 | 63.48 | 0.315 | 14611 | 14276 | 4.33E+10 | 3.22E-01 | 1.02E-01 |
| Step increase in charging/flow decrease | 81.74 | 20 | 61.74 | 0.324 | 18864 | 124 | 3.46E+08 | 2.57E-03 | 8.34E-04 |
| Letdown increase/flow decrease | 76.98 | 20 | 56.98 | 0.351 | 28848 | 1076 | 2.36E+09 | 1.76E-02 | 6.17E-03 |
| Letdown increase/reactor trip | 74.7 | 20 | 54.7 | 0.366 | 33544 | 30 | 5.84E+07 | 4.34E-04 | 1.59E-04 |
| Letdown increase/flow increase | 73.48 | 20 | 53.48 | 0.374 | 36555 | 13294 | 2.42E+10 | 1.80E-01 | 6.74E-02 |
| Cooldown/flow increase | 70.96 | 20 | 50.96 | 0.392 | 44239 | 5 | 7.92E+06 | 5.89E-05 | 2.31E-05 |
| Flow decrease/flow increase | 69.76 | 20 | 49.76 | 0.402 | 48763 | 1101 | 1.63E+09 | 1.21E-02 | 4.87E-03 |
| Flow decrease/reactor trip | 68.26 | 20 | 48.26 | 0.414 | 55414 | 10 | 1.36E+07 | 1.01E-04 | 4.18E-05 |
| Letdown increase/letdown decrease | 64.66 | 20 | 44.66 | 0.448 | 78577 | 89 | 9.72E+07 | 7.23E-04 | 3.24E-04 |
| Letdown increase/flow decrease | 62.34 | 20 | 42.34 | 0.472 | 102284 | 14311 | 1.35E+10 | 1.00E-01 | 4.75E-02 |
| Reactor trip/flow decrease | 60.66 | 20 | 40.66 | 0.492 | 126777 | 5 | 4.23E+06 | 3.15E-05 | 1.55E-05 |
| | | | | | | **Σ** | 1.34E+11 | 1.00E+00 | **0.261** |

$$\frac{\Delta\sigma_M}{\Delta\sigma_G} = \sum_{i=1}^{n} \frac{Q_i}{Q_{TOTAL}} \cdot \left( \frac{\Delta\sigma_M}{\Delta\sigma_G} \right)_i$$

$$Q_i = \left(S_{ALT}\right)_i^m \cdot N_i$$

$$Q_{TOTAL} = \sum_{i=1}^{n} Q_i$$

$N_i$ = Number of cycle for $i^{th}$ load pair

$m$ = Paris Law exponent (for pc-PRAISE $m = 4$)

$n$ = Total number of load pair combinations

$\left(S_{ALT}\right)_i$ = Total alternating stress intensity for the $i^{th}$ load pair

$\left(S_{ALT}\right)_i = \left(\Delta\sigma_M + \Delta\sigma_G\right)_i$

$\Delta\sigma_M$ = Uniform membrane stress

$\Delta\sigma_G$ = Linear and non-linear gradient stress

Table 7.6 illustrates an application of the above equations to charging line calculations of Section 5 of this report. These calculations included a total of 18 load pairs. The total range of alternating stresses (membrane plus gradient contribution) for each of the 18 load pairs are listed in the second column of Table 7.6. The fraction of the alternating stress that comes from a membrane stress component was subject to uncertainty. For this example, a 138-MPa (20-ksi) cyclic membrane stress range ($\Delta\sigma_M$) for all load pairs was assumed. Columns of the table list the membrane-to-gradient stress ratios for each of the transients (values ranging from 0.081 to 0.492) along with values of the weighting factors. The weighted average value of the membrane-to-gradient stress ratio (as shown in the lower left-hand corner of the table) was calculated to be 0.261.

### 7.5.3 Postulated Flaw Model

In accordance with L-3210 of Appendix L, and for reasons previously stated, the initial postulated flaw depth was obtained from the allowable inservice examination surface flaw depth specified in the acceptance standards (Table IWB-3514-2). Accordingly, the initial postulated flaw depth for a flaw depth for this example is 1.37 mm (0.054 in.) (12.2% of the wall thickness).

The initial equivalent single crack aspect ratio 20.5 was obtained by linear interpolation of the results in Figure 7.4 for a wall thickness of 11.1 mm (0.438 in.) and a cyclic membrane-to-gradient stress ratio of 0.261.

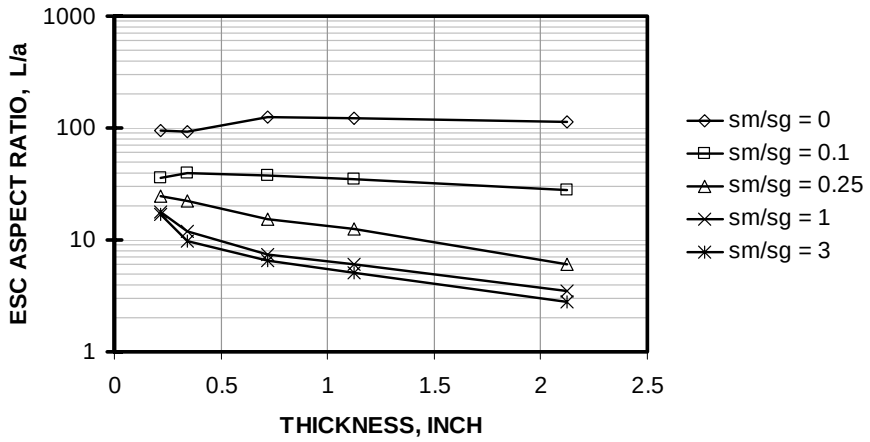


**Figure 7.4 Appendix L Equivalent Single Crack Aspect Ratio as a Function of Wall Thickness and Cyclic Stress Ratio for Austenitic Stainless Steel**

### 7.5.4 Reference Flaw End-of-Evaluation Period Flaw Depth and Operating Period

Fatigue crack growth calculations for the postulated reference flaw were performed and the increment flaw crack was plotted as a function of operating time in Figure 7.5. In this analysis, it was assumed that the occurrence of the transient cycles and alternating stresses in Table 7.6 was distributed uniformly over the 40 year design life of the component. Local crack tip stress intensities and corresponding incremental crack growth were calculated for both the depth and the length directions.

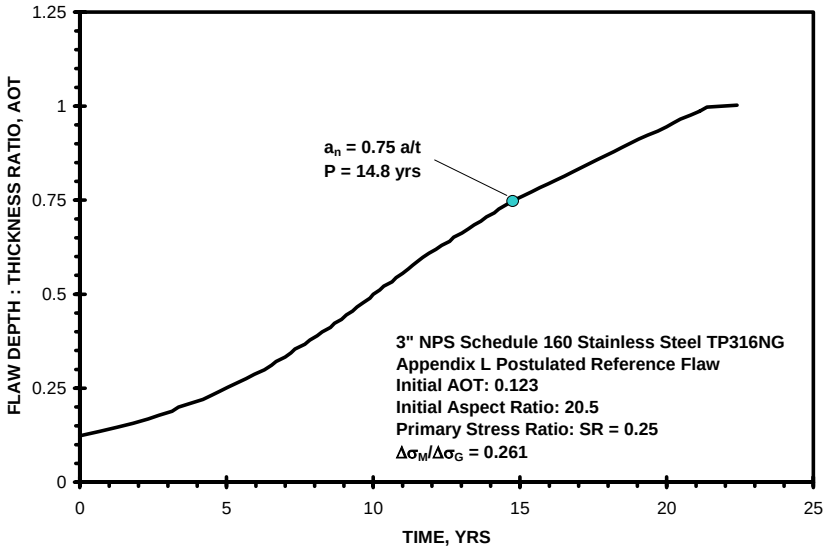


**Figure 7.5 Fatigue Crack Growth Analysis Results for 76.2 mm (3-in.) Schedule 160 Austenitic Stainless Steel NUREG/CR-6260 New Vintage Westinghouse Charging Nozzle**

The results of the fatigue crack growth calculations, along with the procedures in C-3300 of Appendix C and the allowable (critical) flaw depths specified in Table IWB-3641-1, were used to determine the Appendix L reference flaw end-of-evaluation flaw depth. A graphical representation of this analysis is shown in Figure 7.6.

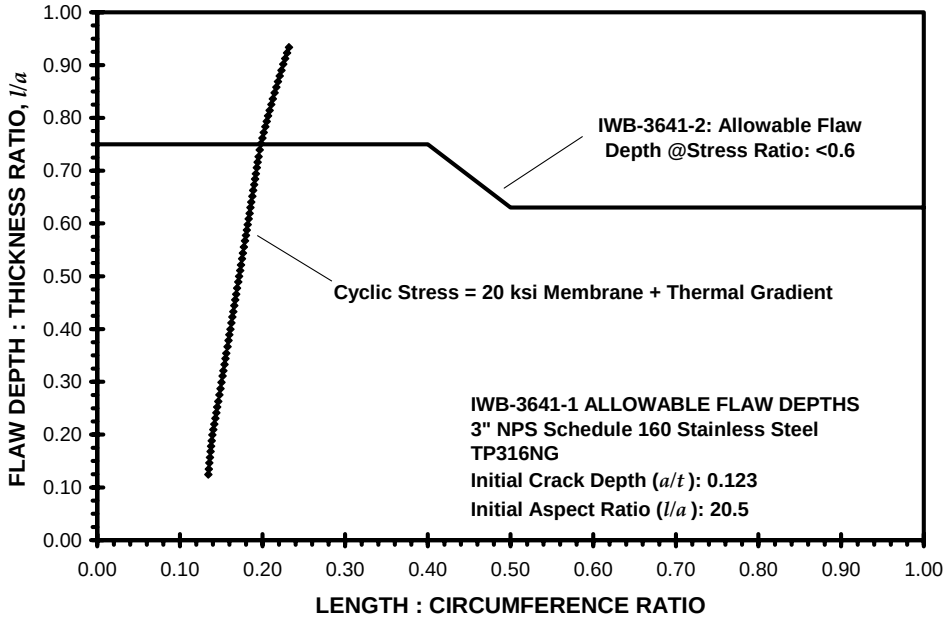


**Figure 7.6 Appendix L End-of-Evaluation Allowable Flaw Depth Analysis for 76.2 mm (3-in.) Schedule 160 Austenitic Stainless Steel NUREG/CR-6260 New Vintage Westinghouse Charging Nozzle**

In Table IWB-3641-1 ASME Code Section XI, the allowable flaw depth is specified relative to nominal wall thickness (i.e., a/t) and is a function of the final flaw length-to-circumference ratio and the applied primary stress ratio,

$$SR = \left(P_m + P_b\right) / S_m$$

where $P_m$ and $P_b$ are the applied membrane stresses at the postulated reference flaw location.

In this example, negligible primary bending stress is assumed. Therefore, the applied primary stress ratio is

$$SR = \frac{P_m}{S_m} = \frac{1}{4}\frac{p \cdot D_o}{t \cdot S_m} = \frac{1}{4} \times \frac{2.25 \times 3.5}{0.438 \times 18}$$

$$SR = 0.25$$

where $p$ = operating pressure = 15.5 MPa (2.250 ksi)
$D_o$ = outside nominal diameter = 89 mm (3.5 in.)
$t$ = nominal wall thickness = 11.1 mm (0.438 in.)
$S_m$ = ASME Section III Code Allowable Stress Intensity = 125 MPa (18.1 ksi)

From Figure 7.6, when the applied primary stress ratio is less than 0.6, the reference flaw maximum allowable end-of-evaluation flaw depth $a_n = 0.75$.

The operating period P is defined in Appendix L as the time required for the postulated reference flaw to grow to an end-of-evaluation flaw depth $a_f$ that is equal to the maximum allowable flaw depth, $a_n$. From Figure 7.5, P = 14.8 years.

## 7.6 Concluding Remarks

A methodology has been developed to address the affects of the initiation and linking of multiple fatigue cracks on component fatigue life. Applications of this methodology provide a technical basis for recommended changes to Appendix L. Tables 7.4 and 7.5 give recommended values for aspect ratios for postulated equivalent single cracks that conservatively account for the efforts of the initiation and linking of multiple cracks. Although the resulting calculations to be performed with Appendix L do not explicitly address multiple cracking, the enhanced aspect ratios of the postulated cracks ensure conservative calculations for fatigue crack growth and for required inspection intervals. For loadings that produce mainly membrane-type stresses, the original 6:1 aspect ratio of Appendix L was shown to be an appropriate assumption. However, for loadings giving high through-wall thermal gradient stresses, the 6:1 aspect ratio was shown to be non-conservative. For such loadings, Table 7.4 and 7.5 recommend aspect ratios much greater than 6:1.

# 8 Conclusions

Experience suggests that, when service-induced fatigue problems in operating plants are caused from thermal stratification or hot/cold water mixing conditions, large nonlinear gradient stress profiles tend to grow cracks in the length direction because the highest cyclic stresses occur at the surface. This causes surface cracks to initiate and coalesce and grow as effectively larger defects. Consequently, the use of a 6:1 aspect ratio single crack specified in Appendix L would not adequately model crack growth for all operating conditions.

The PDI program has generated a large amount of data that can be used to quantify NDE performance relative to combinations of controlling performance variables. The inspection teams taking the PDI demonstration test used common testing procedures/inspection protocols and inspection-equivalent equipment, and this added confidence to the statistical calculations. However, when used to develop POD models, limitations stem from the fact that both Appendix VIII and the PDI implementation program were designed as a qualification screening process in which minimum threshold acceptance criteria are applied to NDE inspector test results and were not designed to specifically determine/measure POD. The more significant of these limitations include the following:

- The treatment of far-side access in stainless steel specimens may not represent all conditions expected to occur in the field. Because of the difficulties associated with inspecting stainless steel welds when inspection access is limited to the far side, each PDI test specimen was screened to ensure that the far-side flaw was detectable using the best available technology. Therefore, the performance results represent a best effort and are applicable to cases where only far-side flaws in stainless steel welds can be detected. Additional research will need to be completed to relate these conditional results to POD expectations in the field.

- The flaws selected for Appendix VIII performance demonstration tend to be planar and do not include flaws with depths below 10% through-wall thickness (i.e., below the flaw acceptance criteria in ASME Section XI Table IWB-3410-1). Consequently, assumptions will need to be made regarding the shape of the POD curves below 10% through wall thickness.

- The performance results that were based on observations in only the PASS qualification category (i.e., observations in which the inspector passed the Appendix VIII requirements) are optimistically high because, in many cases, these same inspectors also contributed to the failed observation counts. The inspector's performance is expected to degrade between re-qualification periods because most examinations in the field are performed on good materials that rarely have recordable defects.

- There exists a wide range of field conditions, many of which are not directly represented in the PDI test specimen sets and test conditions.

- The inspector acts alone during the performance testing rather than as part of a team in the field, where he would receive additional input when characterizing and sizing defects.

The results reported in Section 4 support the following conclusions:

- Excellent NDE performance for fatigue cracks can be expected for ferritic materials. Very little difference was observed between the POD curves for all the ferritic cases considered in this study.

- Very good performance can be expected also for circumferential cracks in stainless steel when the crack is located on the same side of the weld in which the NDE examination is made. For these conditions, POD depended primarily on component thickness. In all these cases, inspector qualification had a small effect on the resulting POD curves.

- A POD curve with an asymptotic upper limit at large flaw sizes appears to be justified. Therefore, the data will be very useful in helping to improve existing asymptotic factors currently assumed in pc-PRAISE and other probabilistic fracture mechanics software.

- Because the PDI data are limited to flaw sizes greater than 5% through-wall depth, future analyses will need to consider false call probabilities to better define the shape of the POD curves at very small flaw sizes.

The results reported in Section 4 show that for all ferritic material components and for wrought stainless steel components with configurations that allow inspection from the same side of the weld of the postulated defect, the ability to detect fatigue cracks (TWC depths of 10%–25%) is much better than the flaw detection models previously relied upon in probabilistic fracture mechanics codes such as pc-PRAISE. Because smaller defects can be detected and repaired earlier in plant life, significant improvements (factor of 10 or greater) in component reliabilities come from the performance of periodic inspections as indicated by the probabilistic fracture mechanics results of Figure 5.21.

Because very good NDE performance can be expected at flaw depths consistent with allowable flaw depths specified in ASME Section XI Tables IWB-3514-1 and 3514-2, the hypothetical flaw depths currently specified in ASME Section XI Appendix L can be reduced to the depths specified in these tables.

The resulting crack growth analyses documented in Section 6 showed that the nature of crack growth is strongly dependent on the aspect ratio of the initial surface crack and on the relative magnitude of cyclic membrane stresses and cyclic gradient stresses (i.e., linear and/or nonlinear). As expected, under thermal transient conditions typically associated with fatigue failures observed in the field, the high-cycle loadings attributed to thermal striping, turbulence penetration, and thermal mixing can lead to mainly surface cracking at shallow flaw depths. Recommendations for the aspect ratios of postulated flaws have been developed in terms of equivalent single cracks as given by Tables 7.4 and 7.5.

The nature of the thermal fatigue mechanisms, associated with failures observed in the field, causes several small fatigue cracks to initiate, coalesce, and then grow like an equivalent long single crack. The results reported in Section 7 showed that an equivalent single crack model can be used in fatigue damage tolerance calculations that can adequately account for the effects of multiple crack initiation and growth. Aspect ratios for equivalent single cracks are specified in Tables 7.4 and 7.5.

# 9 References


64 FR 51370-51400. September 22, 1999. U.S. Nuclear Regulatory Commission, "Industry Code and Standards; Amended Requirements."

ASME. 2004a. ASME Boiler and Pressure Vessel Code, *Rules for Inservice Inspection of Nuclear Power Plant Components, Section XI*. American Society of Mechanical Engineers, New York.

ASME. 2004b. ASME Boiler and Pressure Vessel Code, An International Code, *Rules for Construction of Nuclear Facility Components, Section III, Division 1 – Subsection NB, Class 1 Components*, 2004 Edition, American Society of Mechanical Engineers, New York.

Barson J and S Rolfe. 1987. "Fracture and Fatigue Control in Structures." In *Applications of Fracture Mechanics*, 2nd ed. Prentice-Hall, Englewood Cliffs, New Jersey.

Chopra OK. 2002a. *Mechanism of Fatigue Crack Initiation in Austenitic Stainless Steel in LWR Environments.* NUREG/CR-6787, U.S. Nuclear Regulatory Commission, Washington, D.C. Available at http://www.nrc.gov/reading-rm/doc-collections/nuregs/contract/cr6787/cr6787.pdf (March 2007)

Chopra OK. 2002b. "Mechanism of Fatigue Crack Initiation in Austenitic Stainless Steel in LWR Environments," *Pressure Vessel and Piping Codes and Standards*, PVP-Vol. 439, R.D Rana, ed., American Society of Mechanical Engineers, New York. pp. 133–142.

Chopra OK and WJ Shack. 2001. *Environmental Effects on Fatigue Crack Initiation in Piping and Pressure Vessel Steels*. NUREG/CR-6717, U.S. Nuclear Regulatory Commission, Washington, D.C.

Deardorff AF, DA Harris, and D Dedhia. 2002. *Materials Reliability Program: Re-Evaluation of Results in NUREG/CR-6674 for Carbon and Low-Alloy Steel Components (MRP-74)*. Electric Power Research Institute, Palo Alto, California.

EPRI. 1986. *Evaluation of Flaws in Austenitic Stainless Steel Piping*. EPRI-NP-4690-SR, Electric Power Research Institute, Palo Alto, California.

EPRI. 1995. *Operating Nuclear Power Plant Fatigue Assessments*. EPRI-TR-104691, Electric Power Research Institute, Palo Alto, California.

EPRI. 2002. Materials Reliability Program: Re-Evaluation of Results in NUREG/CR-6674 for Carbon and Low Steel Components (MRP-74). EPRI-TR 1003667, Electric Power Research Institute, Palo Alto, California.

Gavenda DJ, PR Luebbers, and OK Chopra. 1997. "Crack Initiation and Crack Growth Behavior of Carbon and Low-Alloy Steels." In *Fatigue and Fracture 1*, Vol. 350, S Rahman, KK Yoon, S Bhandari, R Warke, and JM Bloom (eds.), pp. 243-255. American Society of Mechanical Engineers, New York.

Gosselin SR. 1995. "ASME Section XI Philosophy Related to Operating Nuclear Power Plant Fatigue Damage Protection." In *International Pressure Vessel Piping Codes and Standards: Volume 2 - Current Perspectives ASME 1995*, PVP Volume 313-2, pp. 171-175. American Society of Mechanical Engineers, New York.

Gosselin SR, AF Deardorff, and DW Peltola. 1994. "Fatigue Assessments in Operating Nuclear Power Plants." In *Changing Priorities of Codes and Standards*. PVP-Vol. 286, pp. 3-8. American Society of Mechanical Engineers, New York.

Gosselin SR, PG Heasler, FA Simonen, SR Doctor, and FL Becker. 2002. "NDE Performance (POD) Curves for Fatigue Cracks in Piping Based on Industry Performance Demonstration Data," in *Proceedings of 10th International Conference on Nuclear Engineering (ICONE 10)*, April 14-18, 2002. American Society of Mechanical Engineers, New York. pp. 1-11.

Gosselin SR, FA Simonen, PG Heasler, FL Becker, SR Doctor, and RG Carter. 2005. "Performance demonstration based probability of detection curves for fatigue cracks in piping." PVP-2005-71027, in *2005 ASME Pressure Vessels and Piping Conference (PVP 2005)—Technologies for Safe and Efficient Energy Conversion*. American Society of Mechanical Engineers, New York. pp. 1-12.

Gosselin SR, FA Simonen, PG Heasler, AF Deardorff and FL. Becker. 2002. *Materials Reliability Program: Recommended Improvements to ASME Section XI Appendix L*. EPRI-TR 1002814, Electric Power Research Institute, Palo Alto, California.

Harris DO and DD Dedhia. 1992. Theoretical and User's Manual for pc-PRAISE, A Probabilistic Fracture Mechanics Computer Code for Piping Reliability Analysis. NUREG/CR-5864, U.S. Nuclear Regulatory Commission, Washington, D.C.

Harris DO, EY Lim, and DD Dedhia. 1981. Probability of Pipe Fracture in the Primary Coolant Loop of a PWR Plant Volume 5: Probabilistic Fracture Mechanics Analysis. NUREG/CR-2189, Vol. 5, U.S. Nuclear Regulatory Commission, Washington, D.C. Publication information available at http://www.osti.gov/energycitations/product.biblio.jsp?osti_id=5341468

Hazelton W. 1986. Technical Report on Material Selection and Processing Guidelines for BWR Coolant Pressure Boundary Piping. NUREG-0313, Rev. 2, U.S. Nuclear Regulatory Commission, Washington, D.C.

Iida K, E Friedman, and V Zilberstein. 2000. "Technical Basis for Flaw Shape Change Formulations Proposed for Appendix A to Section XI," PVP-Vol. 407, Pressure Vessel and Piping Codes and Standards. American Society of Mechanical Engineers, New York.

Keisler J, OK Chopra, and WJ Shack. 1995. *Fatigue Strain-Life Behavior of Carbon and Low-Alloy Steels, Austenitic Steels, and Alloy 600 in LWR Environments*. NUREG/CR-6335, U.S. Nuclear Regulatory Commission, Washington, D.C.

Khaleel MA, OJV Chapman, DO Harris, and FA Simonen. 1999. "Flaw Size Distribution and Flaw Existence Frequencies in Nuclear Piping." In *Probabilistic and Environmental Aspects of Fracture and Fatigue*, ASME PVP-Vol. 386, pp. 127-144. American Society of Mechanical Engineers, New York.

Khaleel MA, FA Simonen, HK Phan, DO Harris, and D Dedhia. 2000. *Fatigue Analysis of Components for 60-Year Plant Life*. NUREG/CR-6674, PNNL-13227, prepared by Pacific Northwest National Laboratory for the U.S. Nuclear Regulatory Commission, Washington, D.C.

PWR Pipe Cracking Study Group. 1990. *Investigation and Evaluation of Cracking Incidents in Piping in Pressurized Water Reactors*. NUREG-0691, U.S. Nuclear Regulatory Commission, Washington, D.C.

Scott P and T Thorpe. 1981. *Prediction of Semi-Elliptic Crack Shape Development During Fatigue Crack Growth*. AERE-R10104. United Kingdom Atomic Energy Authority, United Kingdom.

Simonen FA and SR Gosselin. 2001. "The Impact of ASME Section XI Appendix L Inspections on Piping Reliability," *Pressure Vessel and Piping Codes and Standards*, PVP-Vol. 419, pp. 83-106. American Society of Mechanical Engineers, New York.

Spanner JC, SR Doctor, TT Taylor, and J Muscara. 1990. *Qualification Process for Ultrasonic Testing in Nuclear Inservice Inspection Applications*. NUREG/CR-4882, PNL-6179, prepared by Pacific Northwest National Laboratory for the U.S. Nuclear Regulatory Commission, Washington, D.C.

USNRC. 1980. *BWR Feedwater Nozzle and Control Rode Drive Return Line Nozzle Cracking*. NUREG-0619, U.S. Nuclear Regulatory Commission, Washington, D.C.

Ware AG, DK Morton, and ME Nitzel. 1995. *Application of NUREG/CR-5999 Interim Fatigue Curves to Selected Nuclear Power Plant Components*. NUREG/CR-6260, U.S. Nuclear Regulatory Commission, Washington, D.C.

Wire GL and YY Li. 1996. "Initiation of Environmentally-Assisted Cracking in Low Alloy Steels," *Fatigue and Fracture - Volume 1*, PVP-Vol. 323, pp. 269-289, American Society of Mechanical Engineers, New York.

Wirsching PH. 1995. "Probabilistic Fatigue Analysis." In *Probabilistic Structural Mechanics Handbook*, C Sundararajan (ed.), Chapter 7, pp. 146-165. Chapman & Hall, New York.

# Appendix

# Nondestructive Evaluation Probability of Detection Curves for Fatigue Cracks in Nuclear Piping

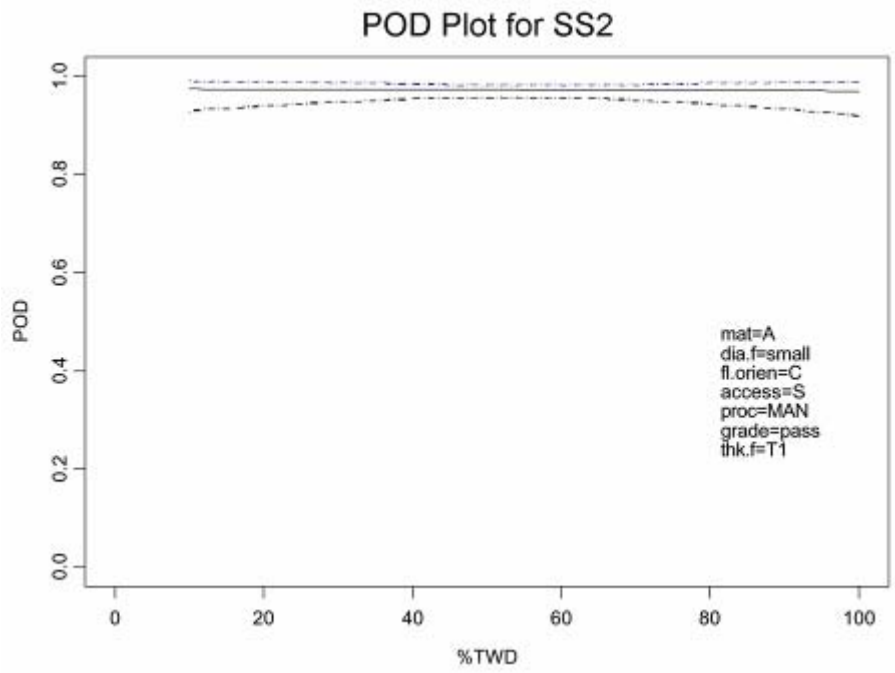
POD Plot for SS2
POD
%TWD
0.0
0.2
0.4
0.6
0.8
1.0
0
20
40
60
80
100
mat=A
dia.f=small
fl.orien=C
access=S
proc=MAN
grade=pass
thk.f=T1

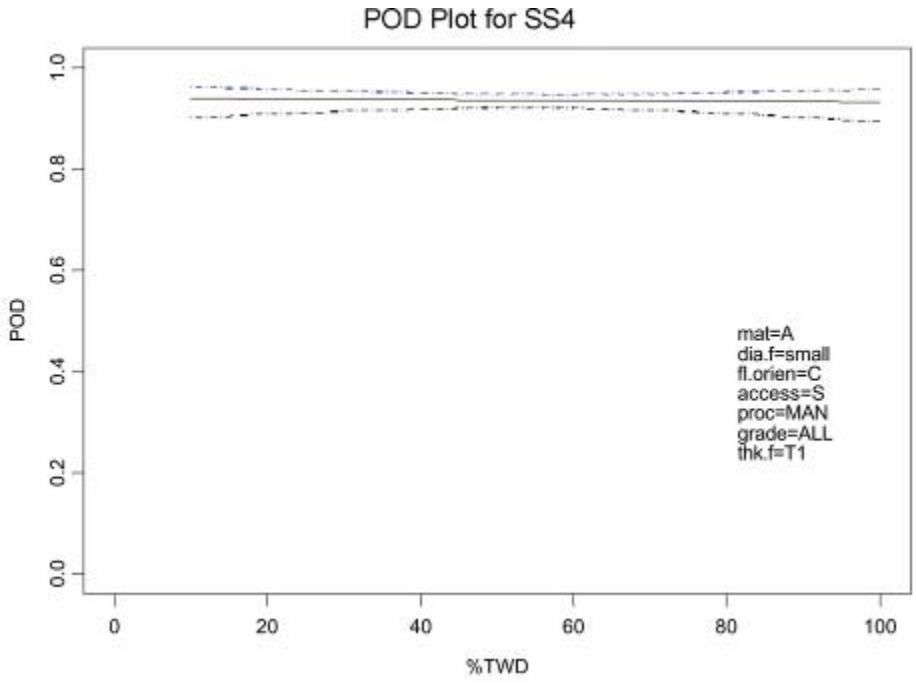
POD Plot for SS4
POD
%TWD
0.0
0.2
0.4
0.6
0.8
1.0
0
20
40
60
80
100
mat=A
dia.f=small
fl.orien=C
access=S
proc=MAN
grade=ALL
thk.f=T1

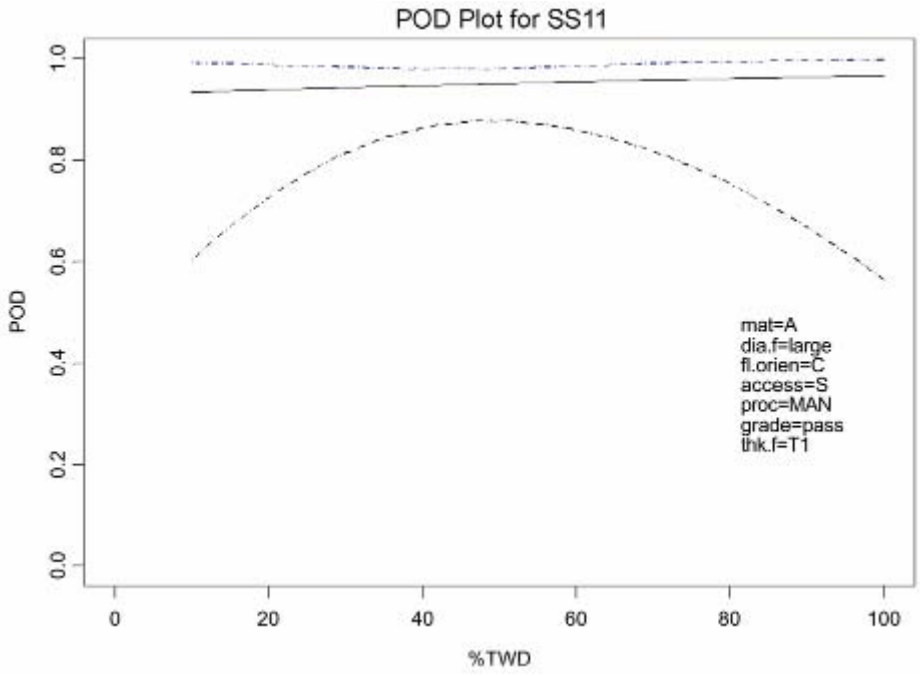
POD Plot for SS11
POD
%TWD
0.0
0.2
0.4
0.6
0.8
1.0
0
20
40
60
80
100
mat=A
dia.f=large
fl.orien=C
access=S
proc=MAN
grade=pass
thk.f=T1

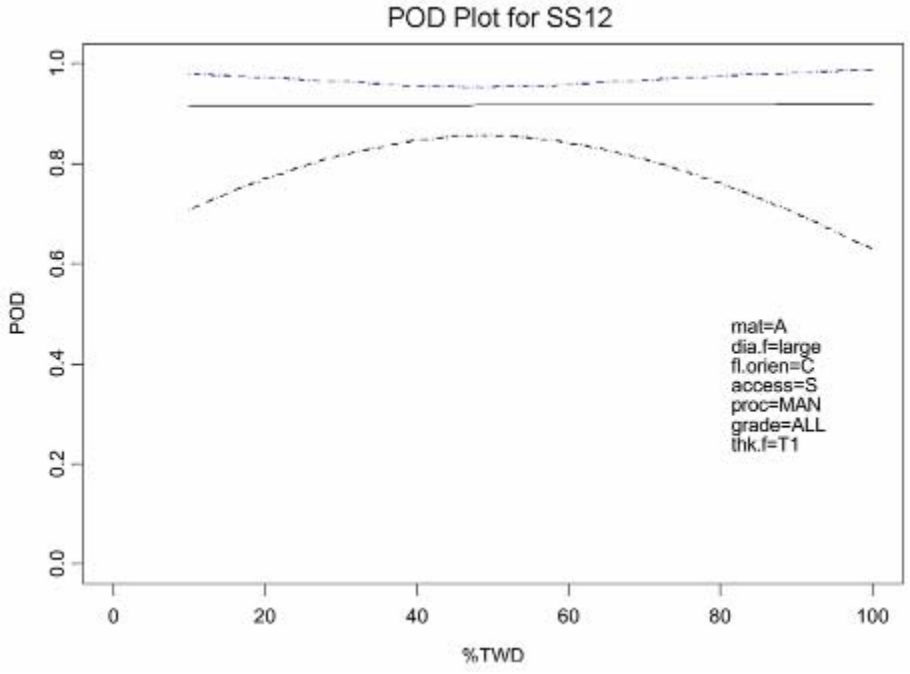
POD Plot for SS12
POD
%TWD
0.0
0.2
0.4
0.6
0.8
1.0
0
20
40
60
80
100
mat=A
dia.f=large
fl.orien=C
access=S
proc=MAN
grade=ALL
thk.f=T1

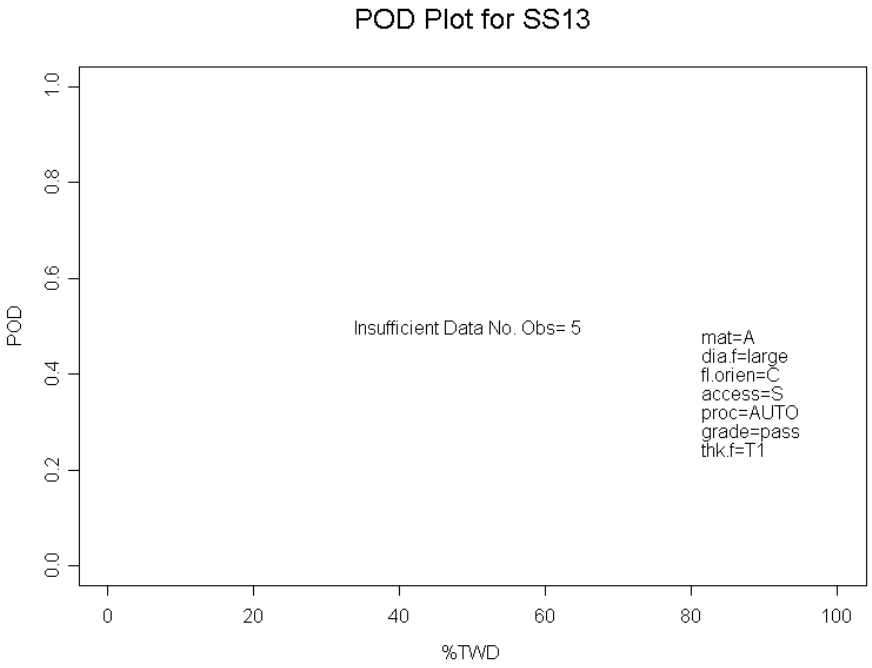
POD Plot for SS13
POD
%TWD
Insufficient Data No. Obs= 5
mat=A
dia.f=large
fl.orien=C
access=S
proc=AUTO
grade=pass
thk.f=T1

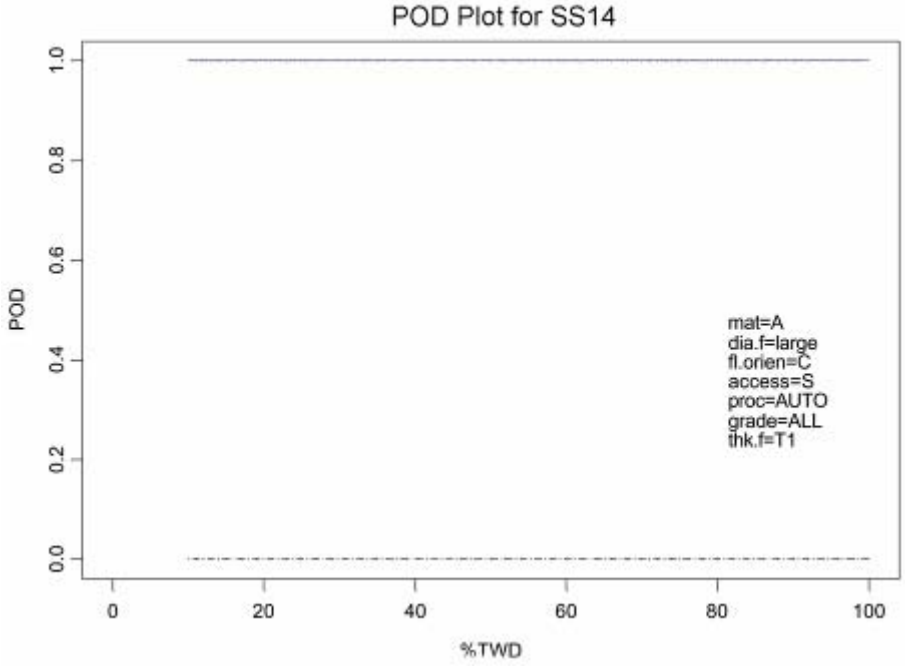
POD Plot for SS14
POD
%TWD
mat=A
dia.f=large
fl.orien=C
access=S
proc=AUTO
grade=ALL
thk.f=T1

POD Plot for SS19

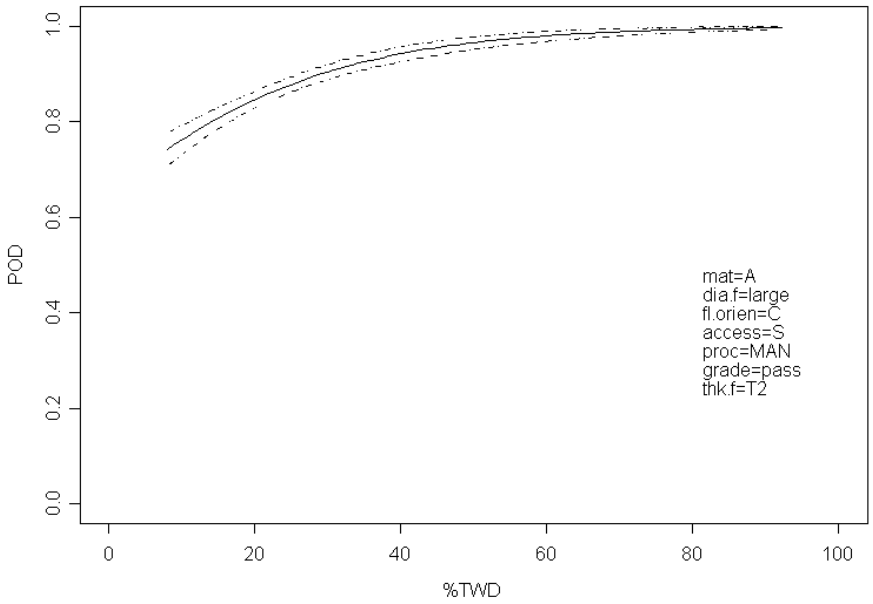


POD Plot for SS20

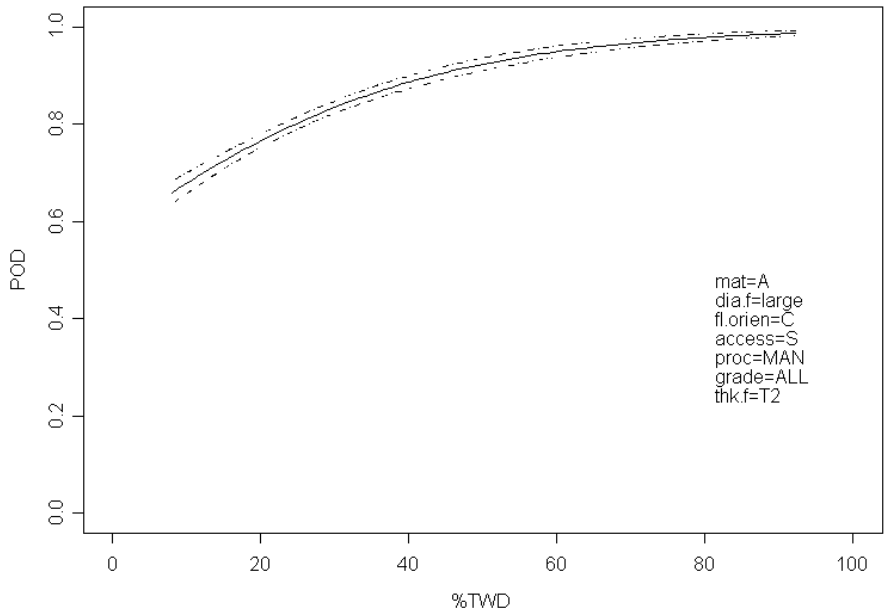

POD Plot for SS21

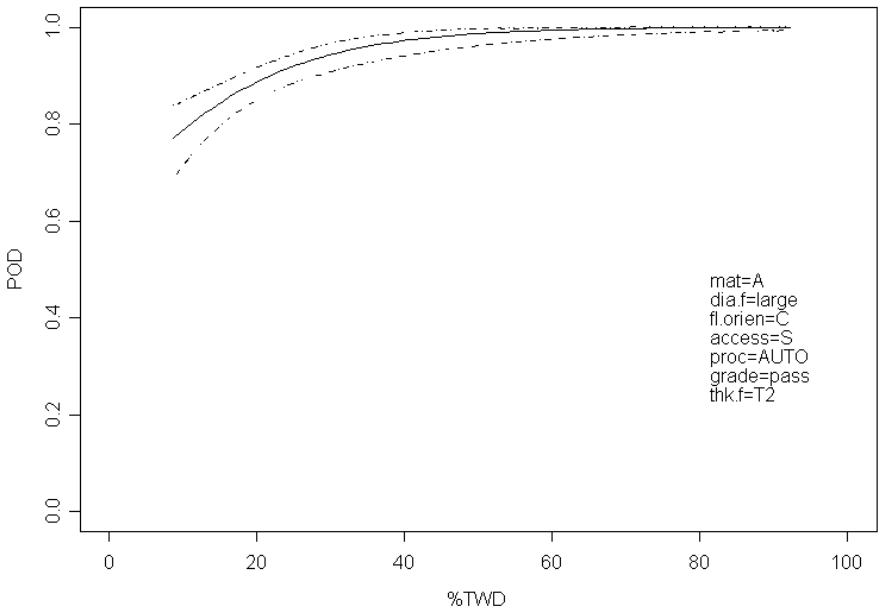


POD Plot for SS22

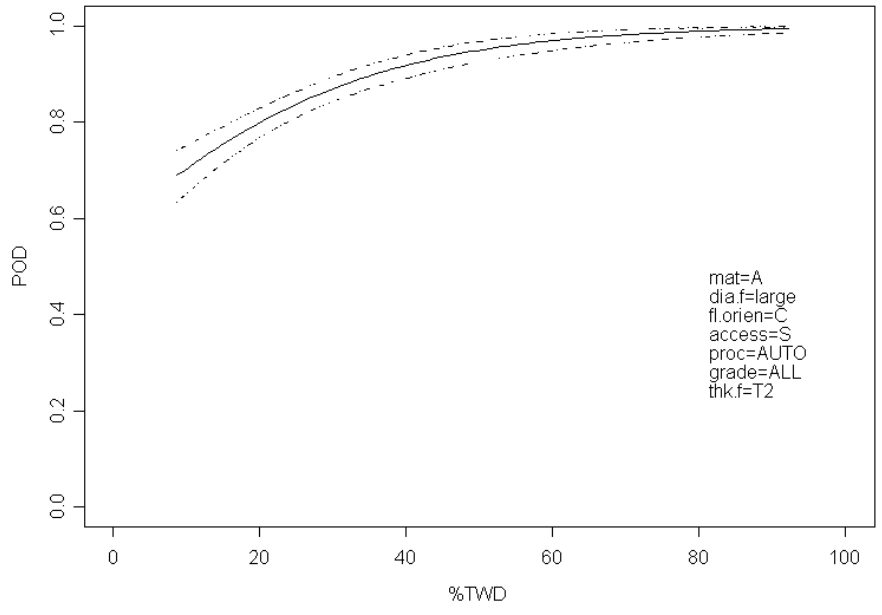

POD Plot for SS27

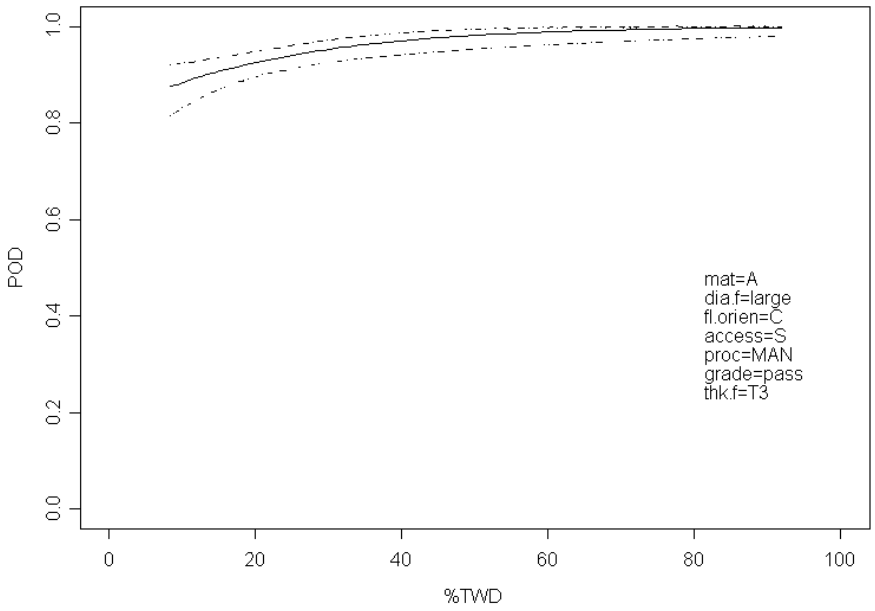


POD Plot for SS28

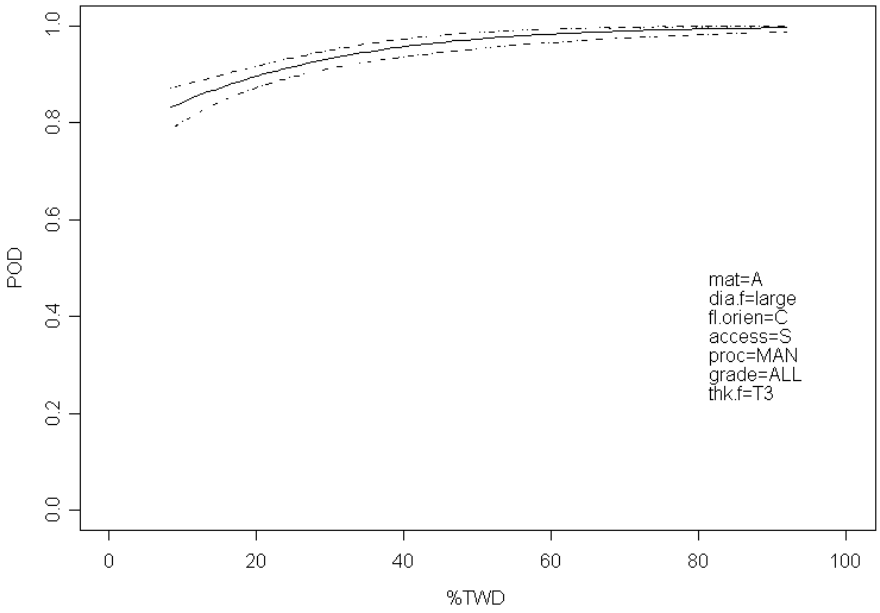

POD Plot for SS29

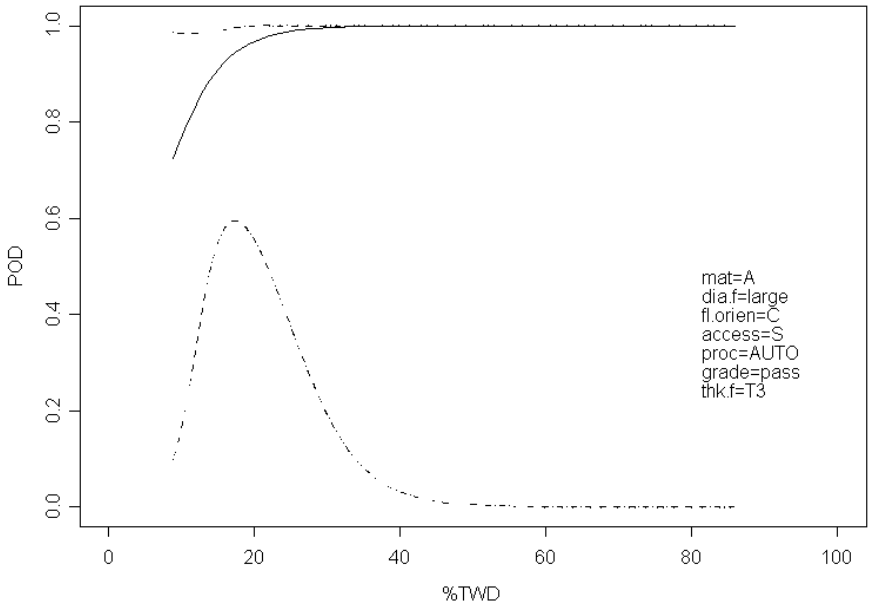


POD Plot for SS30

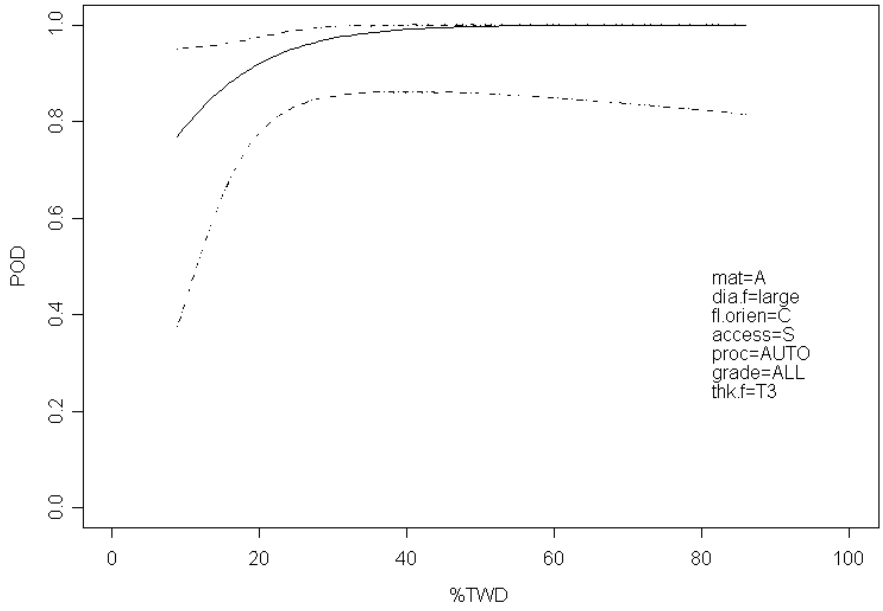

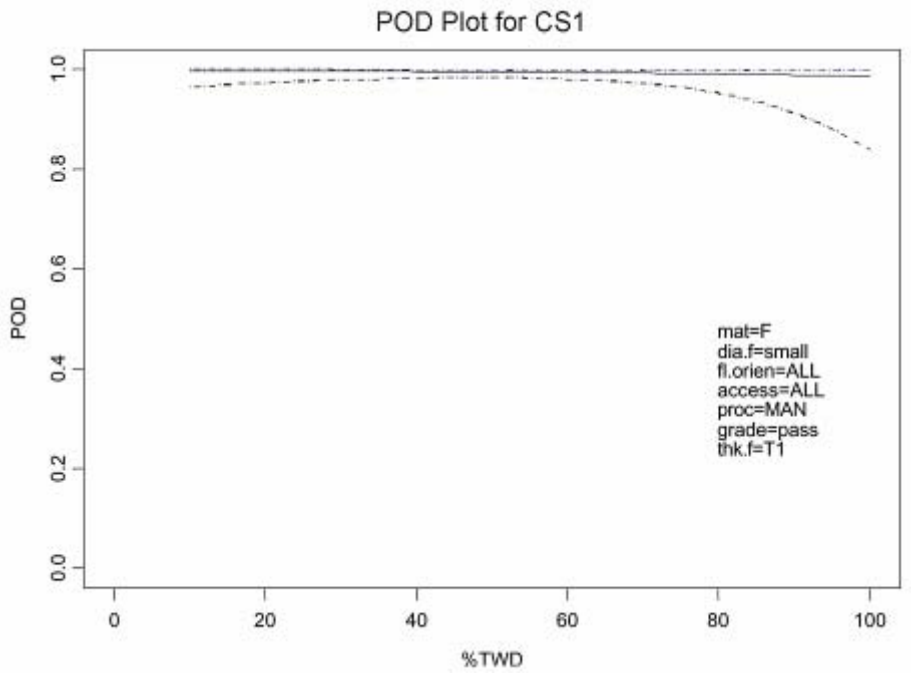
POD Plot for CS1
POD
%TWD
mat=F
dia.f=small
fl.orien=ALL
access=ALL
proc=MAN
grade=pass
thk.f=T1

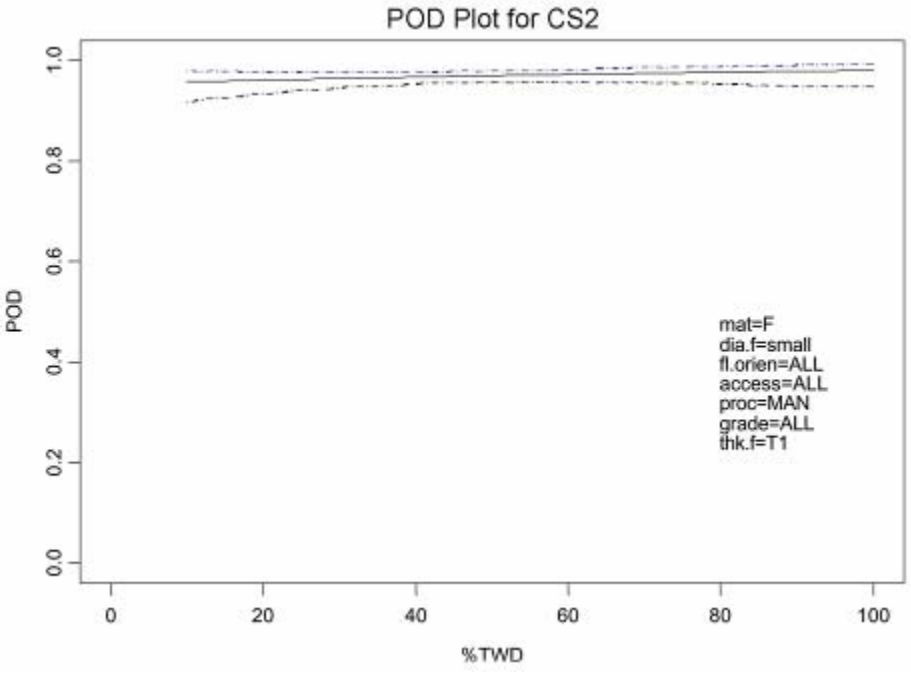
POD Plot for CS2
POD
%TWD
mat=F
dia.f=small
fl.orien=ALL
access=ALL
proc=MAN
grade=ALL
thk.f=T1

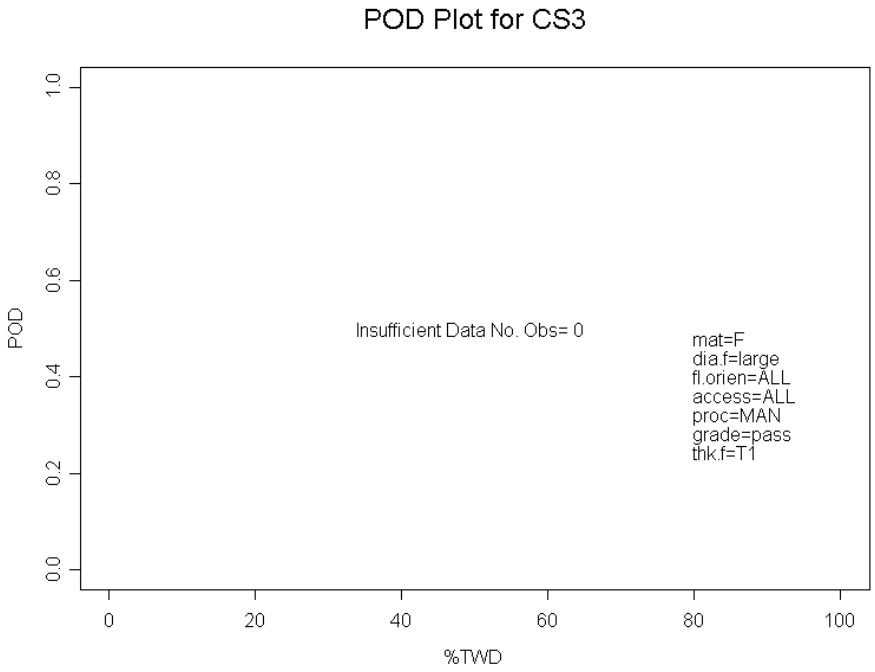
POD Plot for CS3
POD
%TWD
Insufficient Data No. Obs= 0
mat=F
dia.f=large
fl.orien=ALL
access=ALL
proc=MAN
grade=pass
thk.f=T1

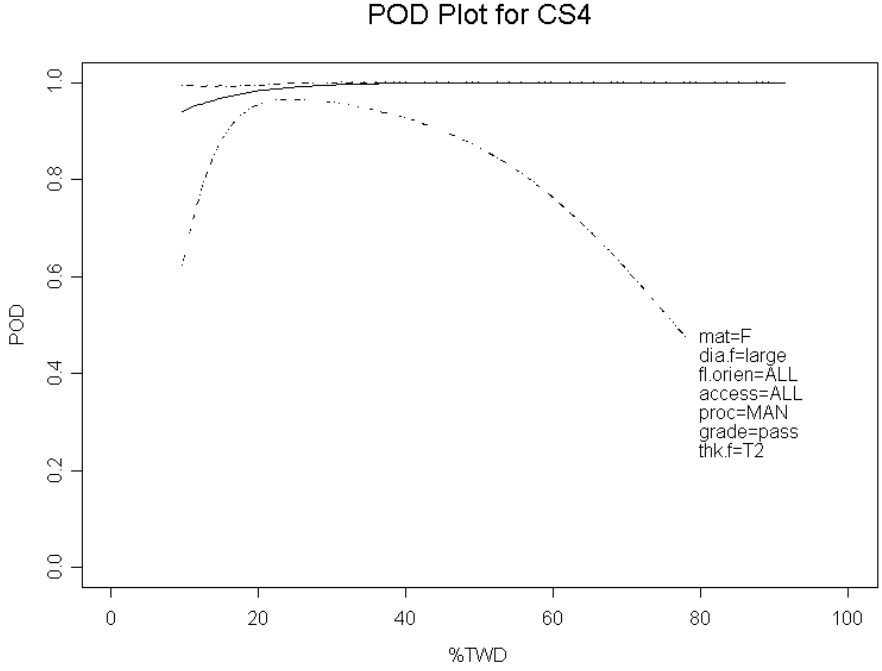
POD Plot for CS4
POD
%TWD
mat=F
dia.f=large
fl.orien=ALL
access=ALL
proc=MAN
grade=pass
thk.f=T2

POD Plot for CS5

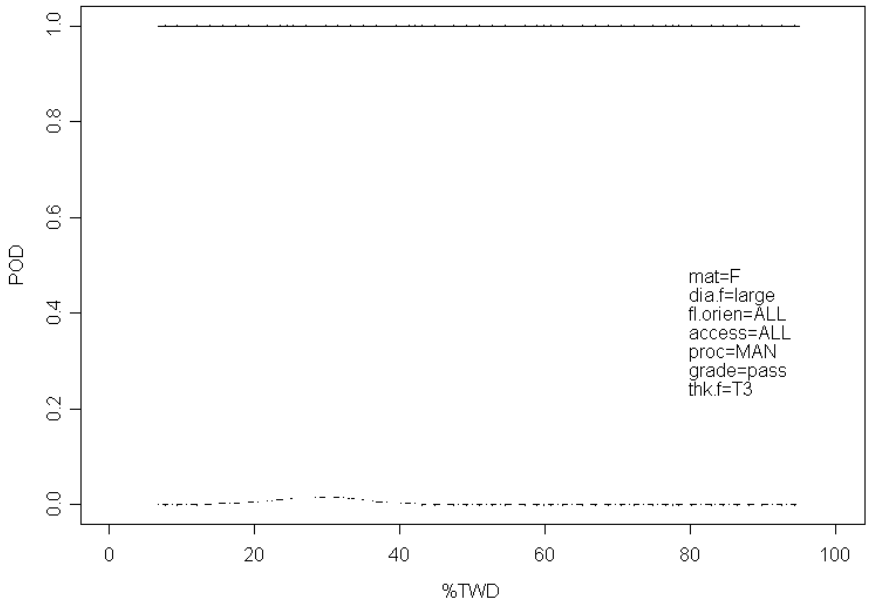


POD Plot for CS6

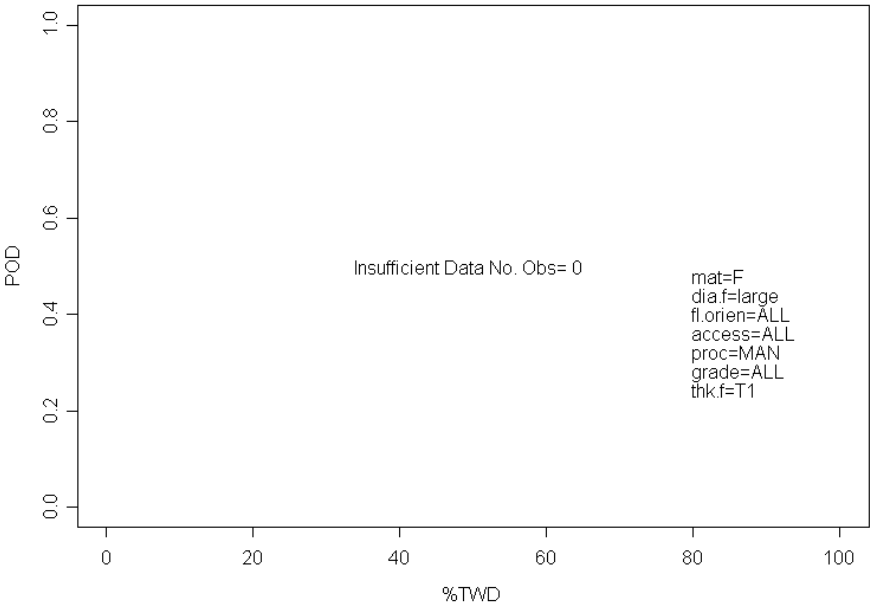

POD Plot for CS7

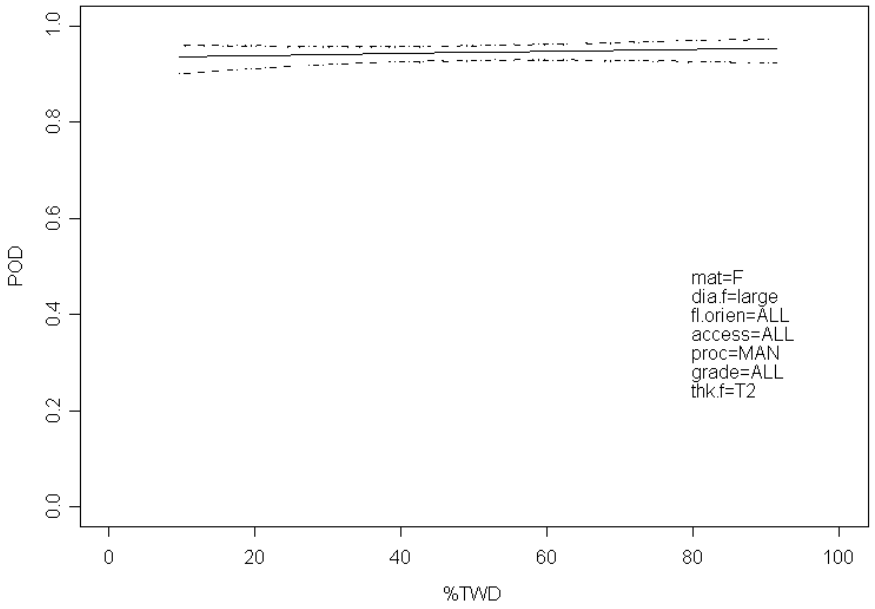


POD Plot for CS8

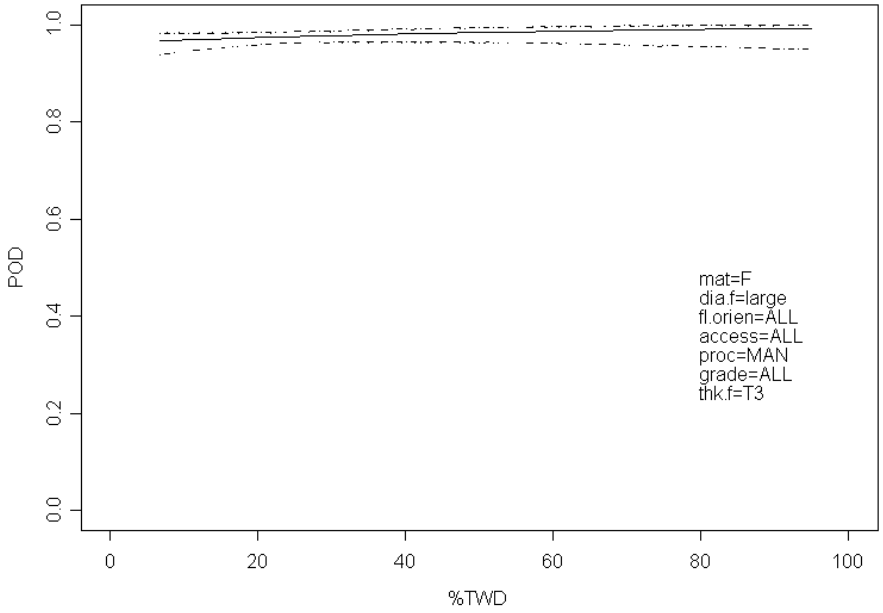

POD Plot for CS9

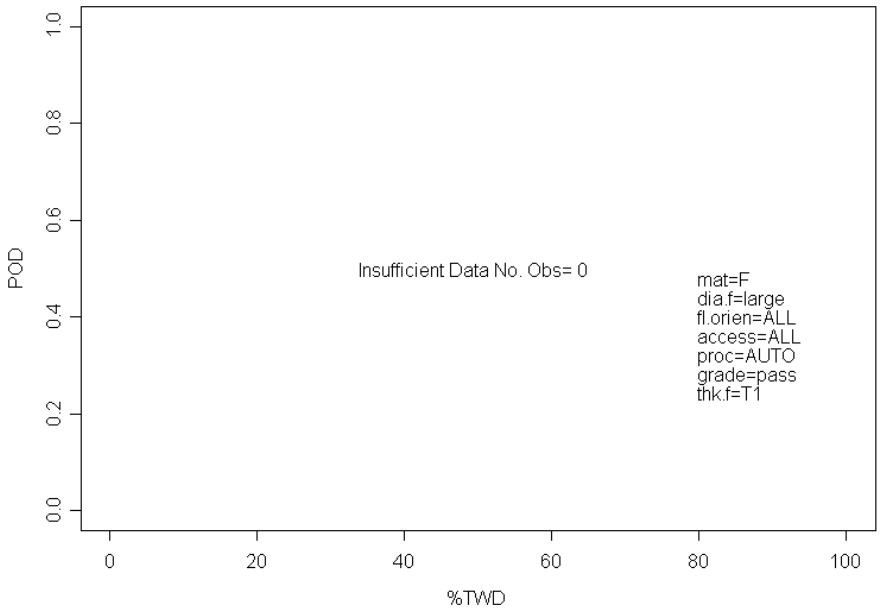


POD Plot for CS10

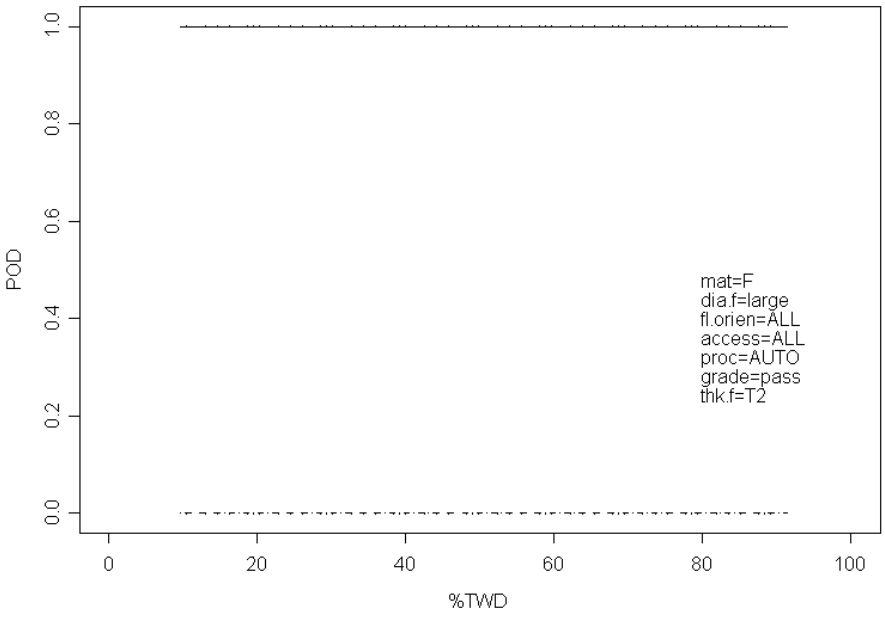

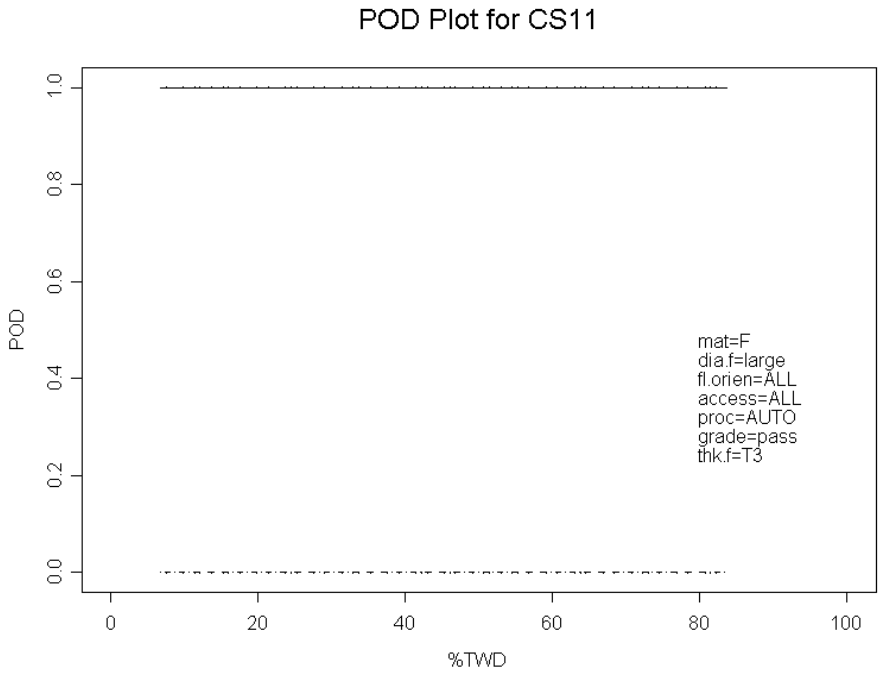
POD Plot for CS11
POD
%TWD
0.0
0.2
0.4
0.6
0.8
1.0
0
20
40
60
80
100
mat=F
dia.f=large
fl.orien=ALL
access=ALL
proc=AUTO
grade=pass
thk.f=T3

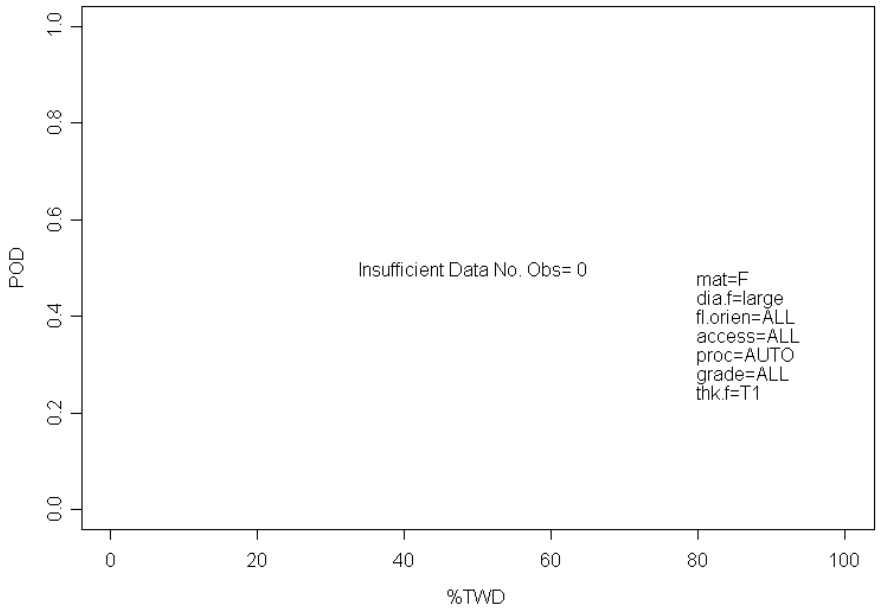
POD Plot for CS12
POD
%TWD
0.0
0.2
0.4
0.6
0.8
1.0
0
20
40
60
80
100
Insufficient Data No. Obs= 0
mat=F
dia.f=large
fl.orien=ALL
access=ALL
proc=AUTO
grade=ALL
thk.f=T1

POD Plot for CS13

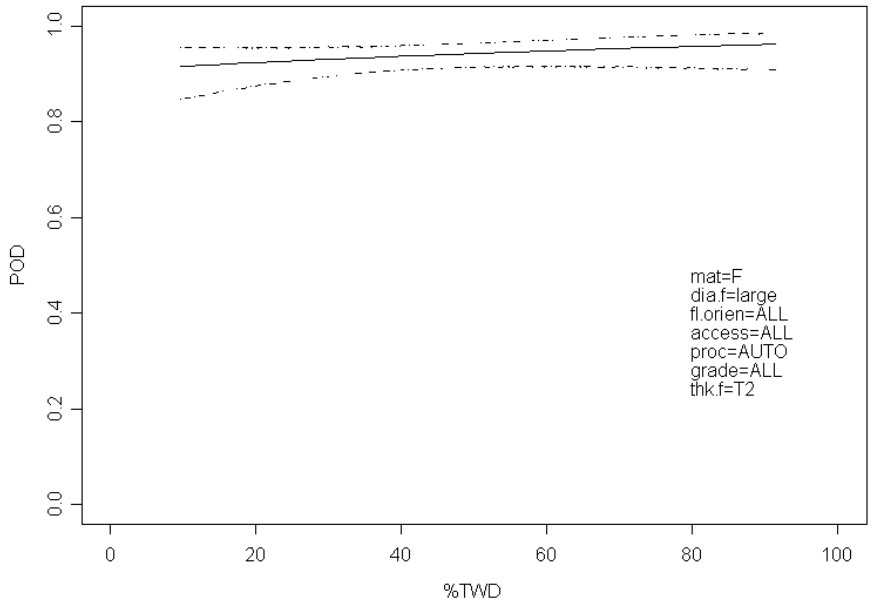


POD Plot for CS14